

**DYNAMICS OF RATE-BASED SEPARATION
METHODS FOR GRANULAR MATERIALS AND
THE SOLID-LIQUID INTERACTION**

by

Diana Marcela Lievano Ortegon

Chemical Engineer, Universidad de los Andes, 2010

Submitted to the Graduate Faculty of
the Swanson School of Engineering in partial fulfillment
of the requirements for the degree of

Doctor of Philosophy

University of Pittsburgh

2016

UNIVERSITY OF PITTSBURGH
SWANSON SCHOOL OF ENGINEERING

This dissertation was presented

by

Diana Marcela Lievano Ortegon

It was defended on

November 24, 2015

and approved by

Joseph J. McCarthy, PhD, Professor, Department of Chemical and Petroleum Engineering

Sachin Valenkar, PhD, Professor, Department of Chemical and Petroleum Engineering

Robert Enick, PhD, Professor, Department of Chemical and Petroleum Engineering

Luis Vallejo, PhD, Professor, Department of Civil and Environmental Engineering

Dissertation Director: Joseph J. McCarthy, PhD, Professor, Department of Chemical and
Petroleum Engineering

DYNAMICS OF RATE-BASED SEPARATION METHODS FOR GRANULAR MATERIALS AND THE SOLID-LIQUID INTERACTION

Diana Marcela Lievano Ortegon, PhD

University of Pittsburgh, 2016

Processing of granular materials is a costly endeavor that spans across a variety of industries ranging from pharmaceutical, food, and cosmetics to construction and metal extraction. Devices commonly used in granular processing however, lack a fundamental understanding of granular behavior - implementing outdated technologies based on heuristics. Separation units for dry mixture, in particular, are highly energy intensive and environmentally unfriendly. For wet or damp mixtures, less is understood about the liquid-solid particle interactions that govern mixture behavior, which has limited development of advanced separation units for wet mixtures in industry.

The work presented here implements discrete element method (DEM) simulations along with experimental work to present two energy-efficient (green), granular separation unit prototypes, designed to rationally exploit the properties of particulate materials that naturally result in segregation. This work also describes an analytical method that yielded a deeper and novel characterization of solid-liquid interactions among two- or three-particles simultaneously. Taken together, the work presented in this dissertation seeks to advance the current state of knowledge of solid-solid and solid-liquid interactions, and has furthered the development of rationale separation systems with applications in industry.

Herein, segregation of granular mixtures with two newly developed systems was successfully demonstrated. Each prototype potentiates the effects of physical differences among particles to achieve separation via a kinetic differential, known as rate-based separation. In the first case, a passive separation system analogous to sieving was developed to success-

fully induce segregation among size-disperse granular mixtures, without being encumbered by issues with material accumulation or fouling. In the second case, separation of density-disperse mixtures was successfully demonstrated using a fluid coated vibrating system. The unique features of these systems make each an attractive option for further development as a unit operation in manufacturing settings, particularly given the rising interest in green technology.

Further study of the rupture forces of complex liquid bridges is presented to advance the understanding of liquid-solid interactions in particle processing. Using a custom-built micromechanical force microscope, the rupture force of bridges conjoining two or three particles were analytically measured. Direct characterization of three-particle interactions in the funicular regime is a novel achievement. Results indicate that the maximum force and rupture distance are the effect of surface characteristics, straining mechanism and effective liquid volume. These insights may encourage new solutions to achieve wet mixture separation.

This work utilizes powerful computational simulations and experimental methods to reveal novel insights of granular behavior, which drive innovation of new, rational separation devices that are attractive to industry applications.

Keywords: granular flow, rate-based separation, mixing, discrete element method, particle dynamics, capillarity, viscosity, lubrication, cohesion, pendular saturation, funicular saturation, liquid bridge rupture.

TABLE OF CONTENTS

1.0 MOTIVATION AND SIGNIFICANCE	1
2.0 BACKGROUND THEORY	5
2.1 Particle Dynamics	7
2.1.1 Contact mechanics	7
2.1.2 The Coefficient of restitution	10
2.2 Vibration driven segregation	11
2.3 Fluids and cohesive forces - Elastohydrodynamic lubrication	13
2.3.1 Liquid Saturation regime	14
2.3.2 Viscous force	16
2.3.3 Capillary force	17
3.0 PASSIVE SEPARATION OF A BINARY MIXTURE USING A GAL- TON BOARD	20
3.1 Introduction	20
3.2 Simulation results	24
3.2.1 Single Particle studies	25
3.2.2 Multi-particle results	29
3.3 Experimental results: Separation of size disperse mixtures using a GB	36
3.4 Statistical analysis of results	40
3.5 Model	42
3.6 Summary and Outlook	46
4.0 DYNAMIC SEPARATION OF A BINARY MIXTURE USING CO- HESION: THE GRANULAR CHROMATOGRAPH	47

4.1	Introduction	47
4.2	Materials and methods	50
	4.2.1 Simulation Parameters and Boundary conditions	51
4.3	Granular Chromatograph: results and analysis	52
	4.3.1 Single particle simulation	52
	4.3.2 Multi-particle simulations	57
4.4	Summary	67
5.0	STUDY OF PENDULAR AND CAPILLARY LIQUID BRIDGES	68
5.1	Introduction	68
	5.1.1 The rupture of a pendular liquid bridge	70
	5.1.2 Viscous Forces	71
5.2	Materials & Methods	73
	5.2.1 Measurement of micromechanical forces in an axially strained liquid bridge	74
	5.2.2 Experimental methodology	76
5.3	Results and Analysis	77
	5.3.1 Liquid bridges between two particles	79
	5.3.2 Three particle system and capillary liquid bridges	81
5.4	Summary and conclusions	87
6.0	OUTLOOK AND CONCLUSIONS	88
6.1	The Galton Board	89
6.2	The Granular Chromatograph	90
6.3	Pendular and funicular liquid bridges	90
6.4	Outlook	91
	APPENDIX A. TESTING THE ROBUSTNESS OF PD CODE - COEF- FICIENT OF RESTITUTION CALCULATION	92
	APPENDIX B. PROBABILITY BASED TERMINAL VELOCITY CODE TO PREDICT SEPARATION IN A GALTON BOARD SYSTEM	95
	BIBLIOGRAPHY	98

LIST OF TABLES

3.1	PD simulations- list of different dimensions and configurations tested for the GB design	26
3.2	Primary experimental and computational parameters for validating PD simulations of the Galton Board	32
3.3	Mixture size ratios for mono-modal size distribution of three mixtures of acrylic particles tested. Particle and system properties are defined in Table 3.2	38
3.4	K-S results for the analysis of distribution variance for the small and the large particle within a bi-disperse mixture	41
3.5	K-S results for the analysis of distribution variance between experimental and simulation results for each particle size, and for each mixture tested	41
4.1	Material mechanical properties for the glass and steel spheres simulated. . . .	51
4.2	Fluid properties for water and Silicone oil at room temperature.	52
4.3	Vibrational energy parameters tested for 200cSt silicone oil single particle simulations.	53
4.4	Vibrational energy parameters tested for water single particle simulations. . . .	55
5.1	Properties for Ethylene Glycol at 20°C	73
5.2	Modified Bond number and expected rupture distance calculations for liquid volumes dispensed	79

LIST OF FIGURES

1.1 Schematic representation of the most frequently identified mechanisms of segregation for granular materials. Adapted from Figueroa [1].	3
2.1 Representation of capillary networks formed between particles in a packed bed at different moisture content levels. a) Lower saturation level - Pendular state. b) Intermediate saturation, with interstitial space between connecting particles - Funicular state. c) Full saturation - Capillary state. d) Slurry.	15
2.2 Sketch of a liquid bridge formed between two spheres. P1 and P2 are planes of symmetry.	18
3.1 Representation of the Galton Board system (left), and comparison of the expected interactions for a small and big particle (right).	21
3.2 Close-up schematic of the characterization parameter d_{eff} , as related to the spacing between pegs l_p and the particle diameter d_i	22
3.3 Exit time distribution for a single particle size as a function of peg diameter. A 4mm diameter particle is implemented for all of the simulations, and the free space between pegs l_p is held constant at 6.4mm which results in a constant value of $D_{eff} = 0.63$. Figure adapted from [2].	27
3.4 Exit time distribution for a single particle as a function of inter-peg spacing for pegs with diameter $d_{peg} = 1.0mm$ and a particle with $d_p = 4mm$. Left: $l_p = 9.4mm$. Center: $l_p = 14.6mm$. Right: $l_p = 19.8mm$. Figure adapted from [2].	28

3.5	Terminal velocity as a function of time for homogeneous mixture for 2mm and 4mm diameter particles. Particles are initially arranged into a monolayer lattice covering 10% of the surface area of the board. Figure adapted from [2].	29
3.6	Plot for the extent of separation (E_s) defined by Eq. 3.3 as a function of the surface area covered by the mixture in the GB device. An equal number of small (2mm) and big (4mm) particles was used. Figure adapted from [2].	31
3.7	Particle distribution obtained via PD simulation along the height of the collector, for three binary mixtures. Particle and system properties are defined in Table 3.1	33
3.8	Particle distribution along the different collector bins for a binary mixture of 2 and 4mm particles at different times. Top left 2s, top right 10s, bottom left 20s and bottom right 25s. The formation of pure species regions in time is evidenced. Figure adapted from [2].	35
3.9	The Galton Board experimental set-up: A device to separate particles via collisional flow. To initiate a run the stencil is removed and the particles flow as a result of gravitational forces, interacting with the pegged region and ultimately being collected at the bottom. Figure adapted from [2].	37
3.10	Particle distribution obtained experimentally along the height of the collector, for three binary mixtures	39
3.11	Particle terminal velocity distribution for mixture ratio = 0.72, extracted from experimental separation videos. Velocity is made dimensionless with the unimpeded rolling time of a sphere down an incline	43
3.12	Average terminal velocity profile for fictional particles with coefficient of restitution of 0.5, 0.7, 0.9 according to probability model compared with a PD simulation based terminal velocity. Soft material results were extracted from the single particle simulations, where a fictitious material with a low coefficient of restitution is tested.	45
4.1	Sketch of the operation of a dynamic granular chromatography column, where A is the vibrational amplitude. The distance between top and bottom wall is $2A$.	49

4.2	Terminal velocity attained by steel and glass particles as a function of Γ employing silicone oil as the fluid (below) and compared with dry conditions (above). The open symbols represent conditions where particles collided with the top wall of the system, whereas filled (black) symbols represent conditions where no interaction with the top wall was observed. The red symbols represent instantaneous velocities for conditions where a steady state velocity was not achieved. The Ξ values and their corresponding to each vibrational frequency are listed in Table 4.3. Standard deviation for all conditions that reach a terminal velocity is smaller than the data symbol size.	54
4.3	Terminal velocity attained by steel and glass particles as a function of Γ employing water as the fluid (below) and compared with dry conditions (above). Open symbols represent conditions where particles collided with the top wall. Filled symbols represent conditions where no interaction with the top wall was observed. The red symbols represent instantaneous velocities for conditions where a steady state velocity was not achieved. The Ξ values and their corresponding vibrational frequency are listed in Table 4.4. Error bars were included for those conditions where the variability was bigger than the symbol size.	56
4.4	Time evolution for the separation of 100 particles, comprised of a 50-50 number fraction of steel and glass particles employing silicone oil at Γ_{o2} . The parameters associated for vibration can be found in Table 4.3.	58
4.5	Time evolution for the displacement of 100 particles, comprised of a 50-50 number fraction of steel and glass particles in the absence of fluid at Γ_{o2}	60
4.6	Time evolution for the separation of 100 particles, comprised of a 50-50 number fraction of steel and glass particles employing water at Γ_{w2} . The parameters associated for vibration can be found in Table 4.4.	61
4.7	Time evolution for the displacement of 100 particles, comprised of a 50-50 number fraction of steel and glass particles in the absence of fluid at Γ_{w2}	62

4.8	Time evolution for the separation of 100 particles of a density disperse mixture of glass using silicone oil at condition Γ_{o2} , where $\rho_1 = 2700kg/m^3$ and $\rho_2 = 8100kg/m^3$	63
4.9	Time evolution for the displacement of 100 particle of a density disperse mixture of glass in the absence of fluid at Γ_{o2} , where $\rho_1 = 2700kg/m^3$ and $\rho_2 = 8100kg/m^3$	64
4.10	Time evolution for the displacement of 2400 particle comprised of a 50-50 number fraction of steel and glass particles employing water at Γ_{w2} . The parameters associated for vibration can be found in Table 4.4.	65
4.11	Time evolution for the separation of 2400 particles comprised of a 50-50 number fraction of steel and glass particles employing oil at Γ_{o2} . The parameters associated for vibration can be found in Table 4.3.	66
5.1	Micromechanical force microscope: Brookfield texture analyzer casing, stainless-steel retractible cantilever, optical displacement sensor.	76
5.2	Image of a pendular liquid bridge between two spheres. The top sphere is attached to the cantilever and the bottom sphere is held static. Straining of the liquid bridge is a result of the upwards movement of the top sphere at constant speed	77
5.3	Force between an acrylic sphere and glass plane forming a pendular liquid bridge measured experimentally compared with the calculated theoretical values for F_{cap}^* (Eq. 5.2), and F_{tot}^* (Eq. 5.5) as described by Pitois <i>et al.</i> The fluid used is Ethylene glycol.	78
5.4	A) Experimentally measured capillary force versus separation curves for an axially strained pendular liquid bridge formed between two identical acrylic spheres ($R = 1mm$). Three runs for each corresponding liquid volume ($V^* = 0.25$, $V^* = 0.50$) of ethylene-glycol are presented. B) Picture liquid bridge of volume $V^* = 0.25$. C) Picture liquid bridge of volume $V^* = 0.50$	80

5.5	A) Measured liquid bridge force for a single axially strained bridge in contact with three identical acrylic spheres. Three runs are plotted for each of the liquid volumes used ($V^* = 0.25$, $V^* = 1.0$). The center-to-center distance for the bottom spheres is $d^* = 2.5$. B) Picture liquid bridge $V^* = 0.25$. C) Picture liquid bridge $V^* = 1.0$	82
5.6	Comparison of the two primary draining behavior observed for a single bridge between three identical spheres. Left: Axially strained single bridge where the neck of the meniscus is located closer to the top sphere. Right: Asymmetrical draining and rupture of the meniscus.	83
5.7	A) Measured Capillary force between for two axially strained liquid bridges formed between three identical spheres. Two separate drops are initially placed on top of each of the bottom spheres. Three runs are plotted for each of the liquid volumes used ($V^* = 0.25$, $V^* = 0.50$, and $V^* = 0.75$). The center-to-center separation between the bottom particles is $d^* = 3.2$. B) Picture liquid bridge $V^* = 0.25$. C) Picture liquid bridge $V^* = 0.50$. D) Picture liquid bridge $V^* = 0.75$	84
5.8	Parallel between the combined effect of two springs in parallel and two liquid bridges held between a three particle unit. A) Shows two springs stretched normal to the surface B) Two springs stretched at an angle θ with respect to the surface.	85
5.9	A) Rupture force for a dispensed liquid volume $V^* = 2.0$ in a 2 sphere and 3 sphere setup. The three-particle configuration here corresponds to the low solid fraction with $d^* = 3.2$. Three runs are plotted for the two and three particle configuration. B) Picture of liquid bridge ($V^* = 2.0$) held between two particles. C) Picture of liquid bridge ($V^* = 2.0$) held between three particles.	86
A1	Coefficient of restitution values obtained implementing PD simulation, as a function of impact velocity. The velocity is made dimensionless with $d_{ref}/\sqrt{\frac{d_{ref}}{g}}$, where $d_{ref} = 9\text{mm}$	94

1.0 MOTIVATION AND SIGNIFICANCE

The problem of granular material processing

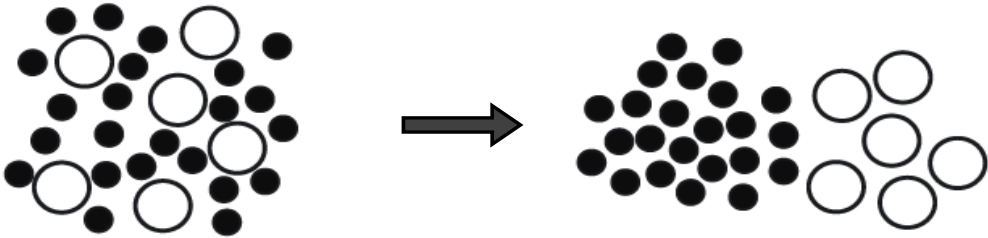
Granular materials, understood as a collection of discrete macroscopic particles, are considered among the top priority materials for human activities and endeavors. Raw solids, in granular form, are important constituents in a variety of industrial processes and geological phenomena [3]. Examples of granular matter and solid handling processes are found in the pharmaceutical, cosmetic, agricultural, food, cement, and metallurgic industries; [4] as well as in natural processes, such as avalanching, land slides and even the accumulation of particulate matter in outer space, forming celestial bodies[5].

Granular materials behave like no other known form of matter; therefore, these solid systems may be considered a unique form of matter, on their own right. At the macroscopic scale, granular materials are capable of withstanding stress without deformation like a solid, yet can be made to flow like a liquid, and can be compressed like a gas [6]. Non-cohesive interaction forces among particles are dominated by repulsive surface interactions. This phenomenon creates dissipative particle-particle interactions. Even as a solid at rest, granular materials behave differently than other forms of matter. Consider a pile of sand- if the grains of sand were poured inside a tall cylindrical container, the solid layer at the bottom would not experience a head pressure like the one displayed by fluids; this is because the pressure experienced by a single particle is not a linear function of height of the column resting above it and instead reaches a maximum value independent of the height [7]. This phenomenon is a result of particle-particle and particle-wall interactions, where the container walls bear the excess weight of the material, allowing for the pressure to reach a maximum. Poured grains, on the other hand, can sediment into regular striations without external aid. Flowing

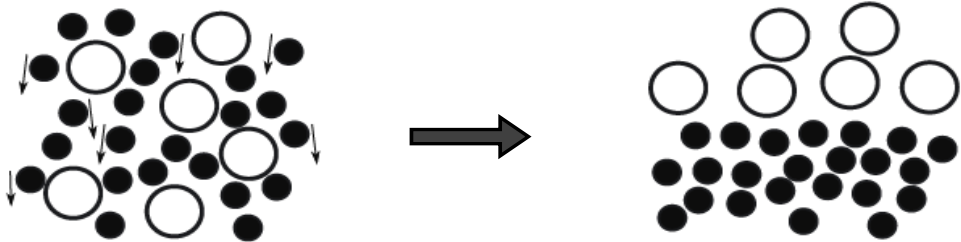
grains are commonly encountered in numerous geophysical situations and frequently induced for industrial practices; herein lies one of the most studied phenomenon in the field - the one of particle segregation [8, 9, 10, 11, 12, 13, 14, 15, 16]. Real life granular materials are comprised of a distribution of different particle sizes and shapes, which results in ubiquitous granular segregation [17]. The problem of mixing and segregation in granular materials has been at the center of granular studies for years. Segregation is an undesirable effect in many industrial processes, in which the mixing performance is typically a critical process parameter in that it may directly impact the quality of the product. One of the most prevalent events when handling granular matter is the one of particle flow. Flowing, shaken, stirred or sheared particles can reassemble, creating distinct localized patterns [18, 19, 20, 12, 21, 17]. Tumbled solids can create radial, or axial dynamic segregation patterns [22, 23, 24, 25, 26]. Undesirable effects industrially result in higher costs and highlights the importance of understanding the segregation phenomena and finding ways to control the degree of un-mixing.

Unlike fluids, granular matter is not affected by temperature as defined by thermodynamics. Thermodynamic temperature allows a fluid system to explore a phase space, which is not possible for granular materials, insensitive to the temperature parameter [7, 27]. This implies that for granular materials, each metastable configuration will last indefinitely as long as it remains unperturbed. Temperature in ordinary gases and liquids additionally provides a microscopic velocity scale for a system. For granular materials this scale is obsolete, and the velocity scale is imposed by macroscopic displacement of the bulk of material [28]. A granular temperature has been used to describe a natural frequency (i.e kinetic energy), attained under steady state, for particulate matter subject to external forces [29, 30]. In the absence of an external energy source, inelastic particles at rest have a natural equilibrium state, that corresponds to a granular temperature of absolute zero [31].

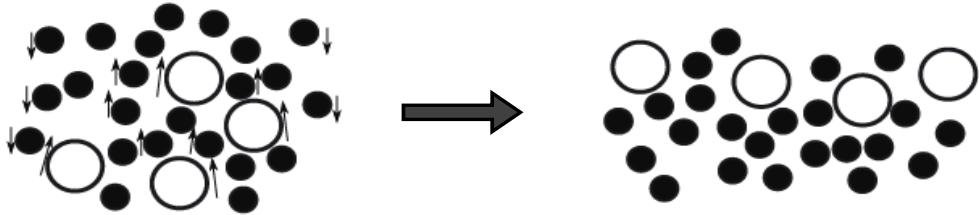
A. Trajectory segregation



B. Percolation segregation



C. Convection segregation



D. Fluidization segregation

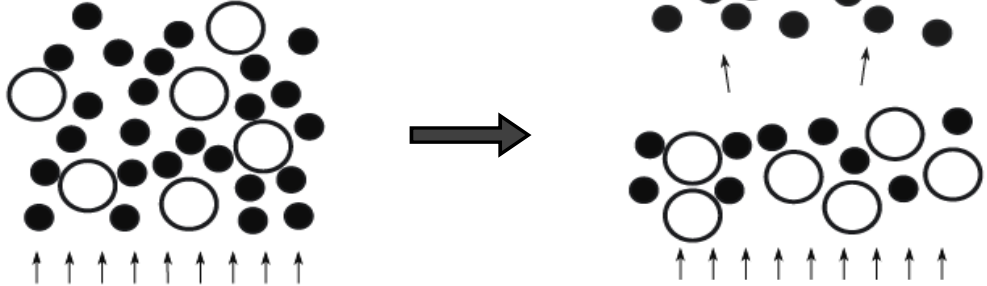


Figure 1.1: Schematic representation of the most frequently identified mechanisms of segregation for granular materials. Adapted from Figueroa [1].

The many innards of segregation have been classified according to the relative characteristics of the particles at hand; however, full quantitative descriptions for each one of these mechanisms are either not available or have not yet been formally recognized as a constitutive model [32]. Currently the mechanisms of segregation are classified as: (a) trajectory (b) percolation segregation (c) segregation convection and (d) fluidization segregation as seen in Fig.1.1. The past two decades have resulted in significant advances in understanding the subject of particulate matter, due to the substantial attention it has been given, and to the ever evolving computational tools available. However, there has been little advancement in translating the acquired theoretical knowledge to manufacturing processes. The need to develop efficient technologies to handle granular materials has become an industry in itself, and yet the methods for separation have remained virtually unmodified.

The present work is organized as follows: Chapter 2 will be dedicated to discussing the theoretical basis for the studies presented in the subsequent chapters. Chapter 3 and 4 demonstrate how, by making use of the very properties that cause particulate matter to segregate, it is possible to envision separation units that are energy efficient. Chapter 3, discusses the experimental and simulation results for a passive, dry separation method employed in size disperse mixtures. Chapter 4 on the other hand, focuses on density disperse mixtures and employs a combination of cohesive and vibrational forces to induce separation. In Chapter 5 a study on the rupture energy of funicular liquid bridges is presented in an attempt to understand the implications of bridging inside of granular arrangements when the interactions are not exclusively pairwise. Finally Chapter 6 presents conclusions and the future work proposed.

2.0 BACKGROUND THEORY

The study of granular materials has historically had a place in the field of engineering driven by the desire to understand and control particle segregation; geologists and sedimentologists followed closely [33], and in the last few decades research efforts have expanded into the field of physics [6]. As a result, instead of furnishing a unified theory for granular materials a plethora of approaches, methodologies, and models can be found. Consequently, it is possible to find as many as 13 different segregation mechanisms cited in literature [34]. In general, fundamental granular studies have focused around four primary mechanisms: percolation/sieving, fluidization, convection, and trajectory segregation. For the purpose of this work, the different mechanisms for segregation will not be individually outlined.

Granular matter is a complex system composed by a large number of discrete macroscopic particles, therefore the three-dimensional flow, mixing, and segregation of such is difficult to model; however, the assumption that the dynamic behavior is limited to a thin surface layer results in a reasonable approximation [14], providing a basis for the implementation of continuum techniques. The application of continuum methods is somewhat frequent inside the scope of granular matter in spite of presenting difficulties to capture phenomena in the mesoscopic to microscopic scale such as jamming and stress chains, frequently found in dense granular media [35]. Continuum models, analogous to theory of fluids, implement conservation equations as it is done for Newtonian fluids, while overlooking the behavior of individual particles. Such techniques obtain a solution to Navier-Stokes type, empirically derived, equations by averaging material properties over the length of the dynamic layer [36]. When applying this theory to granular materials the question of determining an appropriate time and length scale is still open to debate, and is perhaps one of the most important questions to solve in order to design efficient solid manufacture units [7]. Dense, slow flow

presents prolonged contacts with neighboring particles that hydrodynamic approaches fail to represent. In slow flow scenarios, or system comprised only of a few particles, Hertzian forces applied discretely better describe experimental observations [17]. Nonetheless, in systems where it is possible to assume that particles are evenly distributed, and possess identical physical and chemical properties with the bulk, such that they can be thought of as unit, continuum approaches can yield results in qualitative agreement with experimental data [4].

Lagrangian based models provide a different approach to simulating particle systems by employing equations of motion to determine the state of each individual particle at any given time, while employing energy dissipation equations upon interactions between a particle and its surroundings [12, 37]. These event driven models can be divided into two types: probabilistic methods, based on random number generators to determine particle movement, and deterministic based, where trajectories are calculated based on interactions and force balances [4]. One of the better known probabilistic methods is the Monte Carlo (MC) simulation method, where a random walk is generated and particle movements are accepted or rejected based on energy principle. Among its greatest advantages is that it is fast and can be implemented on particles regardless of their shape. MC simulations however, are often too idealized to reproduce real materials [36]. Several Lagrangian particle methods have been developed in the last three decades such as Molecular dynamics (MD), Brownian dynamics (BD), dissipative particle dynamics (DPD) and discrete element method (DEM) [37]. In particular the work described herein makes use of DEM simulations coupled with experimental observations in order to present novel insight into the behavior of granular materials, under free-surface gravity or vibrational driven flow in order to suggest two energy-efficient separation techniques.

2.1 PARTICLE DYNAMICS

Particle dynamics (PD), a form of DEM simulations that is capable of solving the time-dependent spatial evolution of a flowing material comprised of distinct particles, is employed throughout this work to model separation mechanisms and understand the isolated effect of specific design parameters. This simulation technique has been successfully implemented in the study of segregation patterns inside a rotating cylinder [25, 38, 23, 39] and free-surface segregation [40] to gain insight into mixing and segregation of granular materials with various of geometrical configurations and flow types [41, 42]. The results displayed good agreement with experimental observations.

The PD model makes use of a finite difference formulation of the equations of motion, that determines the individual trajectory at the particle level. This work is concerned with the so-called soft sphere model of PD simulations, where collisions are calculated on the basis of the work by Hertz and Mindlin [43]. Translational and rotational motion follow Newton's second law of motion, where a single particle can be determined employing the equations for linear and angular motion. These equations are written in terms of the mass of the particle m_p , radius of the particle R , the linear and angular velocity vectors of said particle (\vec{v}_p and $\vec{\omega}_p$), the moment of inertia I_p gravity \vec{g} , and normal and tangential forces (\vec{F}_n and \vec{F}_t). The corresponding equations are presented below:

$$m_p \frac{d\vec{v}_p}{dt} = -m_p \vec{g} + \vec{F}_n + \vec{F}_t, \quad (2.1a)$$

$$I_p \frac{d\vec{\omega}_p}{dt} = \vec{F}_t \times \vec{R}, \quad (2.1b)$$

Integrating equations 2.1a and 2.1b over a small, finite time interval results in a representation of the time-dependent trajectory evolution. When integration is applied for *every* particle in a system, the bulk behavior is described.

2.1.1 Contact mechanics

The accuracy of calculations, depends on the contact models selected. The work herein follows the theory developed by Hertz [44]. The normal component of a collision between

two particles, or between a particle and a planar surface (rigid, or elastic) is chosen according to the elastic properties of the solids. Considering pairwise interactions among particles, the normal force is described by the following equation:

$$\alpha_i = (R_i + R_j) - \delta_{ij}, \quad (2.2)$$

where α quantifies the amount of particle deformation, R_i and R_j are the undeformed radii of two particles i and j , respectively, and δ_{ij} is the distance between the two geometric centers of each particle. The first time step assumes a purely elastic normal force given by

$$F = k_n \alpha^{3/2}, \quad (2.3a)$$

$$k_n = \frac{4}{3} E^* \sqrt{R^*}, \quad (2.3b)$$

where k_n is the normal force constant, function of particle radii a and specific material properties, namely the Young's modulus (E^*) and Poisson's ratio (ν_i) [44]. E^* and R^* are given by:

$$\frac{1}{E^*} = \frac{1 - \nu_i^2}{E_i} + \frac{1 - \nu_j^2}{E_j}, \quad (2.4a)$$

$$\frac{1}{R^*} = \frac{1}{R_i} + \frac{1}{R_j}, \quad (2.4b)$$

Given a normal force that exceeds the yield force on a particle, plastic deformation occurs. This is modeled by the following linear expression:

$$F = F_y + k_y(\alpha - \alpha_y), \quad (2.5)$$

where F_y is the yield force, α_y is the deformation at evaluated at the yield force, and k_y is the plastic stiffness, defined by $k_y = F_y / \alpha_y$.

$$F_l = \kappa_1 \alpha, \quad \text{for loading,} \quad (2.6a)$$

$$F_u = \kappa_2 (\alpha - \alpha_0), \quad \text{for unloading} \quad (2.6b)$$

The energy dissipation model employed by the PD routine follows Walton & Braun [45] who indicate linear equation can be used to model the elastic resistance of a particle. The use of a stiffer spring constant for the restoration stage than for its deformation assures

that not all the energy is recovered, and the dissipative nature of particle interactions is captured. While it is computationally simple, results obtained implementing this system of equations agree favorably well with experimental observations. Equations for the loading and unloading force balance maintain the same form of Eq. (2.5) and are described by Eqs. (2.6a) and (2.6b), where κ_1 is the normal spring constant, and α_0 is the permanent plastic deformation.

The values for κ_2 and α_0 are calculated by:

$$\kappa_2 = \kappa_1 + K_s F_{max}, \quad (2.7a)$$

$$\alpha_0 = \alpha - \frac{F_{max}}{\kappa_2}, \quad (2.7b)$$

where K_s is a deformation constant and F_{max} is the maximum force attained prior to unloading. Walton & Braun derived the tangential (frictional) force, and Walton gave a complete description of the implementation of this expression [43]. For each time-step, the new tangential force acting at particle - particle contact, F_t , is given as:

$$F_t = F_{t_0} \kappa_t \Delta s, \quad (2.8)$$

where F_{t_0} is the old tangential force and $\kappa_t \Delta s$ is the incremental change in the tangential force during the present time-step due to relative particle motion; meaning, Δs is the term for spatial displacement during the present time-step. This displacement is easily calculated from the component of velocity tangent to the contact surface, v_t (i.e. $\Delta s = v_t dt$ where dt is the time-step).

The work developed by Mindlin (1949) makes a distinction between macroscopic sliding and microslip, where only a fraction of the contact surfaces are moving with respect to each other.

In order to mimic an annular region of microslip at the edge of the contact as well as limit the overall tangential force to follow Amonton’s rule of friction ($F_t \leq \mu_f F_n$ where μ_f is the coefficient of sliding friction), the frictional stiffness, κ_t , is given by the nonlinear expressions:

$$\kappa_t = \kappa_{t_0} \left(1 - \frac{F_t - F_t^*}{\mu_f F_n - F_t^*} \right)^n \quad , \quad \text{for increasing } F_t, \quad (2.9a)$$

$$\kappa_t = \kappa_{t_0} \left(1 - \frac{F_t - F_t^*}{\mu_f F_n + F_t^*} \right)^n \quad , \quad \text{for increasing } F_t, \quad (2.9b)$$

where F_t refers to F_t at the point where the direction of tangential slip changes, κ_{t_0} is equivalent to κ_t in Equation 2.8, and n is an exponent that can take values equal or greater than 1.

2.1.2 The Coefficient of restitution

The coefficient restitution (ε), defined as the ratio of the particle velocity instantaneously after collision (v_f) to the velocity an instant prior to impact (v_0), quantifies the kinetic energy that is dissipated during a single collision [46]. This parameter, first introduced by Newton, plays a key role in understanding the dynamic behavior of granular materials. The coefficient of restitution (COR) can take values in the range $[0, 1]$, depending on the particle velocity prior to impact. For low impact velocities, the value approximates unity, and decreases as impact velocity increases; however, an exact dependance on velocity is unknown [47].

$$\varepsilon = v_f/v_0 \quad (2.10)$$

Approximations for ε , using constants based experimental results, are commonly found in literature, and implemented in computational simulations in order to spare some computational resources [48]. This work rather than introducing a fixed value for the ε particle-particle interactions and particle-wall interactions are allowed to behave according to material properties and dissipate some energy following the mechanism illustrated above. These interactions and energy dissipation mechanisms will dictate the amount of energy remaining after the collision; hence determining the instant velocity at unloading. Doing this allows for

implementing PD code directly for wet cases, given appropriate cohesive interaction equations are included, whereas a constant value for the ε would have to be corrected, empirically, to account for cohesive interactions. Figure A1 displays the calculated coefficient of restitution calculated by forcing the impact of a single particle against a flat plane at different velocities. The observed trends are as expected, with a tendency to a minimum value for high impact velocities.

2.2 VIBRATION DRIVEN SEGREGATION

Vibration has long been identified as one of the most common driving forces of granular separation. Qualitative studies on the effects of vibration on particle beds have been carried out since the 1960s [49]. Theoretical and experimental studies alike have focused on the effect of size, density, shape, and surface interactions in the segregation behavior only to reveal a rich variety of underlying phenomena including heaping, convection, fluidization, arching and the formation of surface waves [50, 51]. The fundamental understanding is that the unique nature of inter-particle interactions, which varies from one particle-type to the next, results in each type having a different final kinetic state, prompting segregation [5, 52, 53, 21, 54]. Consider for instance, a mixture containing two different particle sizes - when a vibrational force is introduced the larger particles tend to rise to the top of the mixture, whereas the smaller particles sink to the bottom of the container. This effect, commonly known as the *Brazil Nut Problem*, has been addressed in numerous studies and the observed phenomena have become benchmark for vibration-driven granular segregation [55, 56, 57].

Vibration is often implemented industrially in granular drying, mixing and purification processes highlighting the importance of having a thorough understanding of vibrational effects on granular materials in order to accurately design processing units [58].

A dimensionless acceleration parameter (Γ) has been accepted to characterize a vibrated granular system and is defined by the equation:

$$\Gamma = \frac{a}{g}, \quad (2.11)$$

where a denotes acceleration - a function of vibrational parameters frequency (f) and amplitude (A) by $a = A\omega^2$. The vibrational frequency, with units radians per second (rps), is expressed as $\omega = 2\pi f$. When Γ is greater than one the free surface of the granular bed becomes fluidized yielding the complex phenomena associated with segregation. The time spent by a particle, or group of particles, not in contact with the driving force surface is called *flight time*.

The moving patterns observed for solids in a vibrated bed relate closely to the oscillatory behavior of the vibrating wall. Bizon *et al.* [47] performed event-driven simulations, as well as experiments, and reported having identified three different pattern formations (stripes, hexagons, and squares) at two different flight times, namely $f/2$ and $f/4$.

Segregation in a vertically vibrated bed has been studied by numerous groups under varying conditions; while a fundamental phenomenological understanding remains elusive, two models have more frequently been suggested to describe particle trajectories when vibration is induced [18, 19, 59, 20, 60, 61, 62]. The *percolation* model describes the movement of an intruder particle as it rises to the top of a vibrated bed. The intruder in this case is particle with a radius larger than the rest of the bed, its movement is possible due to the expansion of the bed with the vibration. The latter implies that percolation reorganization will disappear for low vibrational frequencies (f) because of the limited bed expansion, where the resulting small gaps restrict displacement possibilities for the intruder particle. A second mechanism, *convection*, on the other hand, supposes that the entire bed moves in vertical circuits and particles that are too large to embed within the continuous flow of small particles will rise to the top of the bed. Convection segregation has been found to produce different patterns depending on system geometry (wall-effects) and f , the frequency [20, 21]. Figure 1.1 (b) and (c) are represent the above described mechanisms.

2.3 FLUIDS AND COHESIVE FORCES - ELASTOHYDRODYNAMIC LUBRICATION

Most studies of particle collisions have focused on dry interactions, nonetheless, the area of *elastohydrodynamic lubrication* was developed in response to the need for more comprehensive models describing particle interactions under wet conditions. Davis, Serayssol & Hinch introduced the term; their work numerically solved coupled lubrication theory equations- accounting for viscous interactions due to fluid pressure- and contact mechanics equations to account for dissipation due to deformation [46]. Elastohydrodynamic collisions are governed by two dimensionless parameters: (i) the Stokes (St) number described by Eq. 2.12, which characterizes the bead inertia relative to viscous forces, and (ii) an a dimensionless elasticity parameter (ϵ), which is exclusive dependent on material properties (Eq. 2.13).

$$St = \frac{mv_0}{6\pi\mu a^2} \quad (2.12)$$

$$\epsilon = \frac{4\beta\mu v_0 a^{3/2}}{x_0^{5/2}} \quad (2.13)$$

where $m = 4\pi a^3 \rho_s / 3$ is the mass of the particle, of radius a and density ρ_s , μ is the fluid viscosity, and v_0 is the particle impact velocity when starting at separation x_0 from the colliding surface. The value of β relates to the Poisson's ratio ν_i and Young's modulus E_i by the equation:

$$\beta = \frac{1 - \nu_1^2}{\pi E_1} + \frac{(1 - \nu_2^2)}{\pi E_2} \quad (2.14)$$

where the subindexes $i = 1, 2$ can represent either two-particle or particle-wall interactions.

A critical Stokes number (St_c) exists for all systems; which sets the physical boundary (velocity or height) above which separation will occur [63]. The St_c value was found to be in the range of 1-10, depending on the elasticity parameters for both the sphere's material and the impact surface material. Davis *et al.* additionally reported, via experimental studies for submerged collisions and was later backed by Bair & Kotte, that as the viscosity of the liquid increases the value of St_c decreases [64].

Later work by Barnocky & Davis, introduced a pressure-dependent viscosity term, initially suggested by Chu and Cameron (1962). Nevertheless, Barnocky and Davis concluded that while this term lowers the value St_c , it only weakly affects the outcome of the collision. Adhesive electrostatic forces need not be considered given the size beads implemented in the work herein are 2mm in diameter or larger. Understanding how to characterize the nature of a collision from experimental observations is only a first step towards completing a model capable of reproducing the phenomenon of cohesive particle interactions.

2.3.1 Liquid Saturation regime

Wet granular materials have, for the most part, been studied at the lowest fluid saturation level, known the pendular regime. This regime only allows for the formation of discrete liquid bridges between two solid contact points.

For regimes containing a greater volume of fluid, available literature on the formation and rupture of liquid bridges is scarce and entirely theoretical [65, 66]. In general, the body of work has been focussed to the study liquid bridging, where capillary forces are predominant, for thinly coated surfaces, and has been centered around two-body collisions. A limited number of studies, such as by Donahue *et al.*, have considered three-body collisions between spheres, while still focusing on two particle interactions [67].

The behavior of wet solid particles is influenced by the ratio of liquid to solid volume fraction. Four saturation regimes have been identified based on the type of bridges formed during solid-liquid interactions. Each regime has a particular effect when incorporated into a solid material, from low moisture to complete liquid saturation. The four different saturation levels depicted in figure 2.1 are defined as: [68]

- Pendular state: Singular liquid bridges are formed between particles at finite contact points. Systems containing [0 -13]% by volume of moisture are classified as being in this regime.
- Funicular state: For porous material, pores start getting fully saturated with liquid while others remain filled with air. More complex networks appear as bridges coalesce. Defined for systems having above 13% and up to 25% moisture per volume.

- Capillary state: All void spaces in porous materials are fully saturated by liquid but the pores form a concave meniscus due to capillary action.
- Slurry state: Particles are fully immersed in liquid and the surface of liquid is convex, indicating that there is no capillary action.

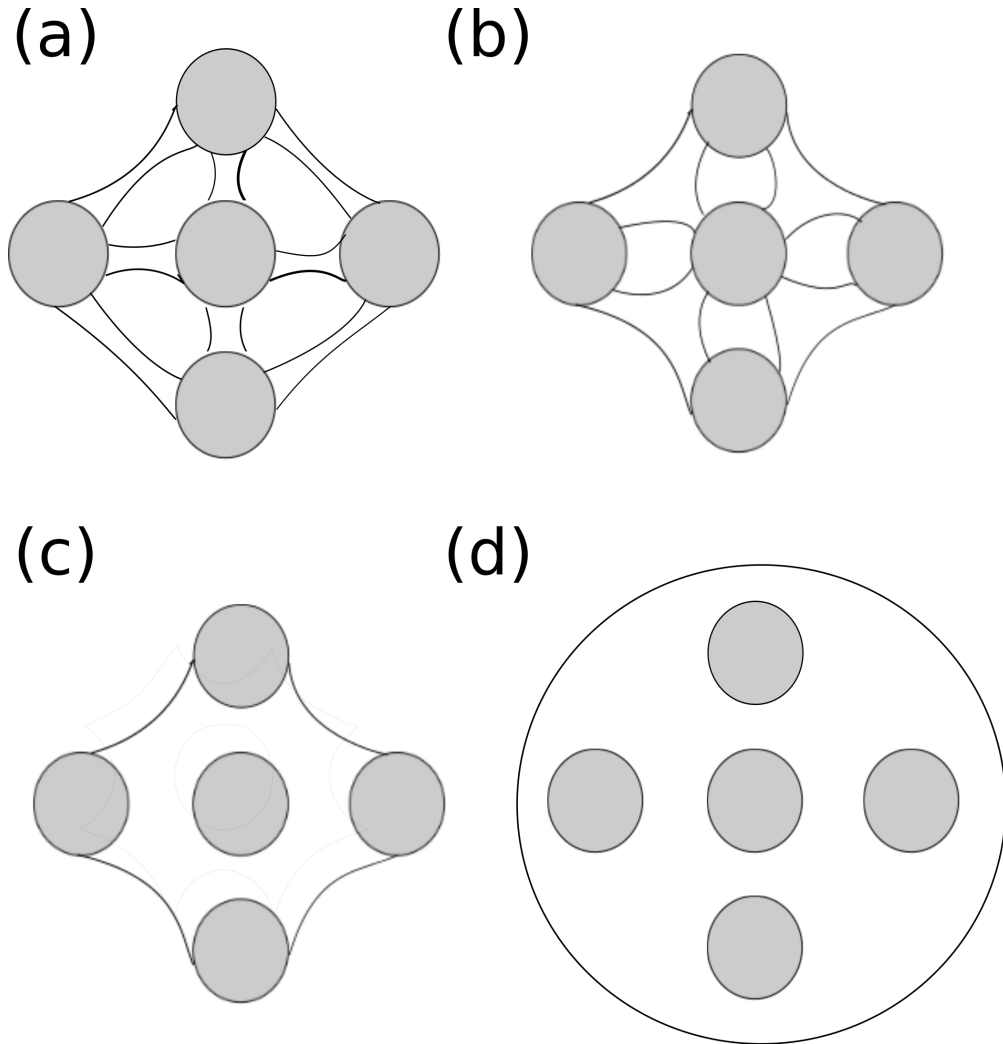


Figure 2.1: Representation of capillary networks formed between particles in a packed bed at different moisture content levels. a) Lower saturation level - Pendular state. b) Intermediate saturation, with interstitial space between connecting particles - Funicular state. c) Full saturation - Capillary state. d) Slurry.

A significant number of studies looked into the rupture forces of liquid-solid bridges, however the solutions to the rupture energy of a liquid bridge were limited to a single, stable meniscus. When moisture exceeds 13% by volume in the funicular regime, bridges start to coalesce making the *number* of bridges, and most importantly the total *volume* of liquid in the meniscus, unknown. Further increasing the liquid content causes a full saturation of the system [69, 70].

Even in cases with a low solid volume fraction, or low liquid concentration, the interactions brought on by the presence of liquid dramatically increases the computation demand of the model. Wet granular collision-laden flows have interactions (instantaneous interactions, or enduring contacts) that can diverge in duration, in up to two orders of magnitude, from identical interactions in a non-cohesive system.

Fluid properties (i.e. density, viscosity and surface energy) are introduced in the PD code to satisfy all capillary and lubrication equations. The total cohesive force calculated is the sum of a capillary component, a viscous component and a dynamic component.

2.3.2 Viscous force

The viscous dissipation components are derived from lubrication theory. A normal component F_{vn} derived by Adams & Perchard [71] is adapted, alongside the tangential contribution F_{vt} proposed by Goldman *et al.* [72].

$$F_{vn} = -6.0\pi R^* \mu v_n \frac{R^*}{D}, \quad (2.15a)$$

$$F_{vt} = -6.0\pi R^* \mu v_t \left(0.5333 \ln \frac{R^*}{D} + 0.9588 \right), \quad (2.15b)$$

where μ is the fluid viscosity, v_n is the relative normal velocity, and v_t is the relative tangential velocity between solids. In order to avoid arbitrarily large values for the viscous force, at small separation distances, a minimum separation is defined by surface asperities, which for this work is a constant value of $D_{min} = 10^{-6}$ m. The total cohesive force is then provided by $F_{tot} = F_{vn} + F_{vt} + F_{cap}$.

2.3.3 Capillary force

For low liquid volumes, where the system is characterized as being in the pendular regime, wet adhesion between two solids has a primordial component result of the action of capillarity. The presence of a liquid meniscus and the phenomenon of liquid bridging govern the adhesive properties of a solid surface, as well as the mechanical properties of contacts between solids [73]. Lian *et al.* [74] defined the capillary action in the absence of gravitational effects or buoyancy as the sum of two components. First, the axial contribution of the surface tension, acting on the three-phase contact line F_s , and second, the hydrostatic pressure differential F_h . These are given by:

$$F_s = 2\pi R\sigma \sin^2 \phi, \quad (2.16a)$$

$$F_h = \pi R^2 \Delta P \sin^2 \phi, \quad (2.16b)$$

$$F_{cap} = F_s + F_h = 2\pi R\sigma \sin^2 \phi \left(1 + \frac{R\Delta P}{2\sigma} \right), \quad (2.16c)$$

where, σ is the surface tension of the fluid, ϕ is the liquid-solid interface contact angle, and ΔP is the pressure differential across the air-liquid interface.

The pressure differential across the liquid-gas interface, defined by the mean curvature (H) of the meniscus, is obtained by solving the Young-Laplace (YL) equation for capillary forces in the presence of a curved liquid-vapor interface.

$$\Delta P = 2\sigma H \quad (2.17)$$

It is commonplace to assume the shape of the meniscus is described by a solid of revolution [75]. While numerical solutions for the YL equation for a wide variety of revolution surfaces are known, more often than not the equation for a toroid is favored [74, 69, 76]. Calculations can be further simplified by making assumptions with regards to symmetry. Understanding that the force should be equivalent on all symmetrical portions of the meniscus, the total force can be calculated as the sum of all portions.

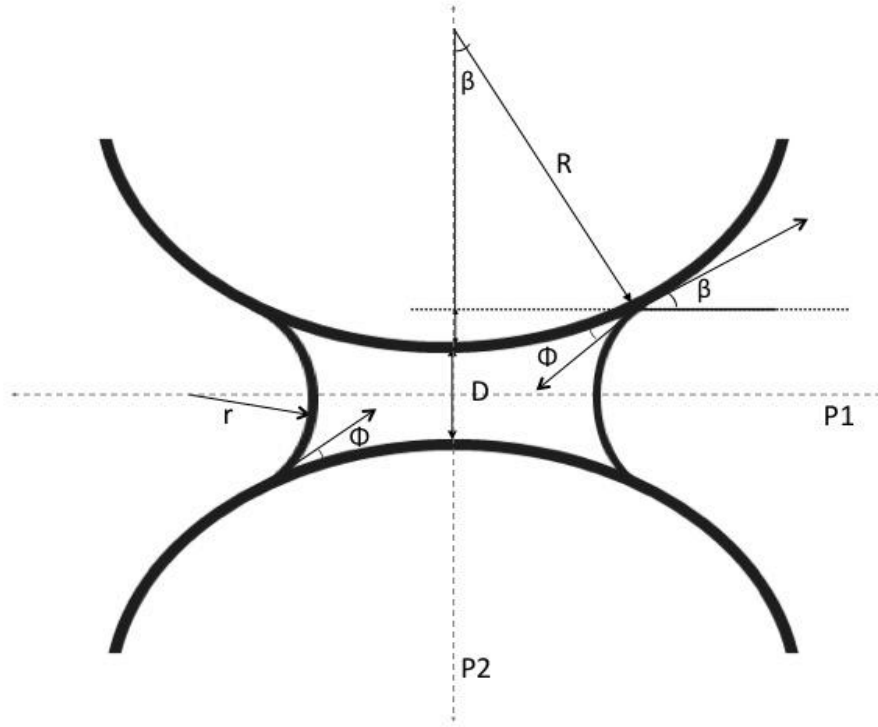


Figure 2.2: Sketch of a liquid bridge formed between two spheres. P1 and P2 are planes of symmetry.

Mikami et. al [77] developed an expression for the total capillary force F_{cap} in terms of three parameters (A, B and C) by correlating experimental data with the analytical solution to the YL equation, as described above.

$$F_{cap} = \pi R^* \sigma \exp(AD + B) + C, \quad (2.18a)$$

$$A = 1.9V^{-0.51}, \quad (2.18b)$$

$$B = (-0.016 \ln V - 0.76)\phi^2 - 0.12 \ln V + 1.2, \quad (2.18c)$$

$$C = 0.013 \ln V + 0.18 \quad (2.18d)$$

Mikami's parameters are a function of the liquid bridge volume V and the separation between solids D , exclusively. This is advantageous in that both of these values can be experimentally measured and are correlated.

The critical separation (D_{rup}) is the maximum distance a liquid bridge can be stretched before it collapses. Lian *et al.* found that for a liquid bridge between two spheres, this separation is related to the liquid bridge volume and the liquid-solid contact angle by:

$$D_{rupt}^* \simeq \left(1 + \frac{\phi}{2}\right) V^{*1/3}. \quad (2.19)$$

The critical separation is used as the liquid bridge rupture criteria in the PD routine where a cohesive contact lasts until the separation between the particles exceeds D_{rup} .

3.0 PASSIVE SEPARATION OF A BINARY MIXTURE USING A GALTON BOARD

3.1 INTRODUCTION

The Galton Board (GB) has been studied extensively in the fields of physics and engineering, as it is one of the simplest examples of a mechanical randomizer, and has served as a model for deterministic diffusion. This system is comprised of a flat surface covered by evenly spaced, interleaved cylindrical obstacles, hence it has also been studied in an analogy to filtration in fibrous or porous media [78]. H.A. Lorentz introduced the 2D Lorentz gas in 1905, to model the thermal and electrical conductivity of metals. The random motion of a single moving electron, where interactions between electrons are neglected and ions are considered to be fixed particles, is physically identical to that of a single particle traversing a GB [79]. Analytical approaches to solving include using theory from chaotic scattering, and theory of billiards [80, 81].

Studies on granular mixing, using a GB, have employed Fickian diffusion-based or stochastic models in representing flow evolution patterns [82, 80, 81, 83, 84], and have described the dynamics as diffusive mixing [85]. A solid mixture is released at the top of the board, with particles rolling down due to gravitational action alone. Lue *et al.* performs experimental studies where bins are placed along the bottom of the system to collect the outflow of the Galton Board.

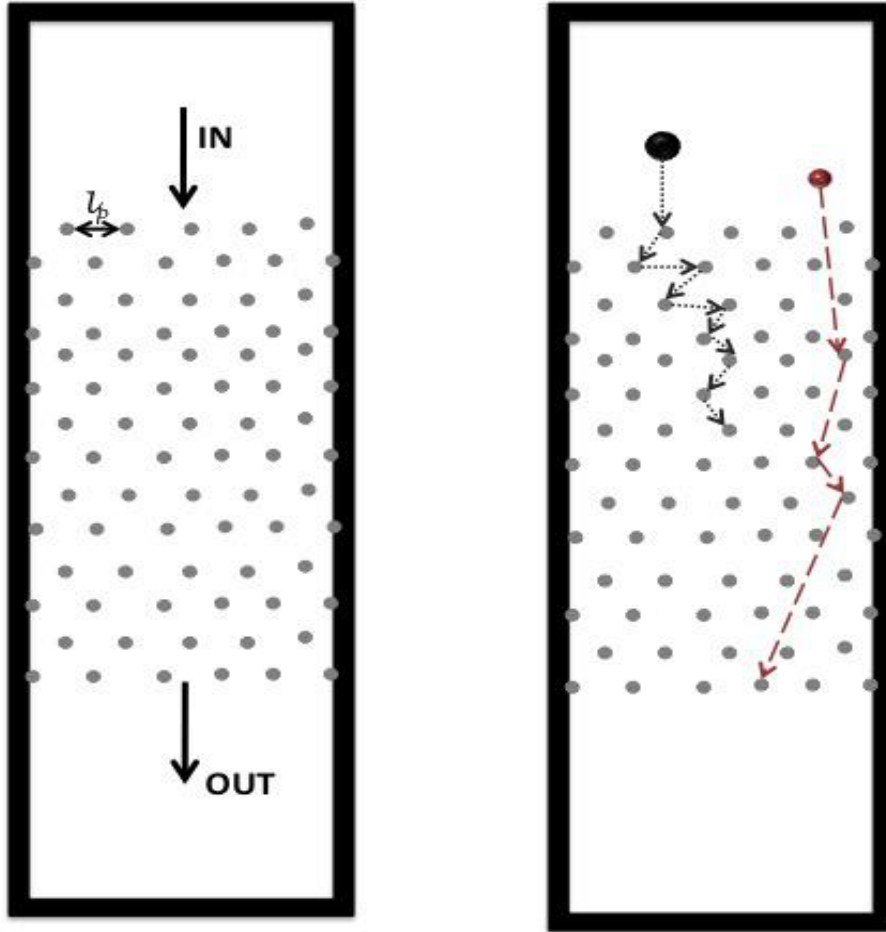


Figure 3.1: Representation of the Galton Board system (left), and comparison of the expected interactions for a small and big particle (right).

The spread of particles in the bins presents a Gaussian distribution in the direction perpendicular to flow [86]. The interactions between particles and the system (e.g. obstacles and boundaries) results in a series of collisions, bounces and free flights for all particles. Most of the analysis for the trajectory distribution of a mixture of grains traversing a GB, has focused on a lateral trajectory diffusion, resulting in a lateral separation for axially flowing material [84, 80].

Periodic lattice type systems, similar to the GB, have been employed in the past to study fluids transport and diffusion. A system described as a geometric ratchet has been employed to induce the lateral separation of the macromolecular constituents of biological

fluids (i.e. DNA or other charged biomolecules), by allowing interactions with scatterers along the system [87, 88, 89]. A geometric ratchet does not require additional vibrational forces, but consists instead of a 2D periodic array of asymmetrical obstacles. This asymmetry generates interactions with the molecules, such that their velocity vector acquires a component perpendicular to the direction of the external force field (i.e. gravity), which constitutes the ratchet effect. Further, the dynamics of the system have applications in a number of microfluidic unit operations[78].

Bruno *et al.* [84] implements a GB to study the lateral dispersion of styrene disks, and characterizes the system in terms of two independent parameters: (1) the coefficient of restitution (ε) and (2) an effective diameter (d_{eff} , refer to Fig. 3.2) given by

$$d_{eff} = \frac{d_i}{l_p}, \quad (3.1)$$

where d_i is the diameter of particle i , and l_p is the inter-peg spacing. This problem has been addressed for a variety of initial conditions, force fields and scatterer geometries [90, 91, 78].

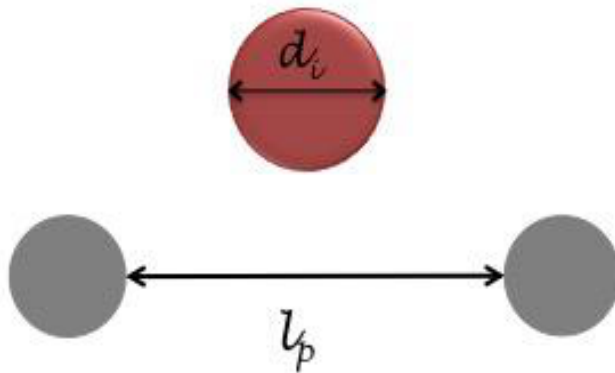


Figure 3.2: Close-up schematic of the characterization parameter d_{eff} , as related to the spacing between pegs l_p and the particle diameter d_i .

It has been shown that the mean free path of a certain particle depends on the solid fraction of the system and/or particle size, such that as solid fraction or particle size are increased the mean free path reduces [92, 91]. In addition to this, due to the dissipative nature of inter-particle collisions, the reflected velocity (v_f) after a collision, relates to the impact velocity (v_i) by

$$v_f = \varepsilon v_i, \quad (3.2)$$

where ε is the coefficient of restitution. This parameter can take any value between 0 and 1.0 depending on the elasticity of the collisions which, in turn, are dependent on the particles' material properties [48]. Scott and Bridgewater [93] studied spontaneous percolation inside a uniform bed as a function of the coefficient of restitution, in addition to proving the friction coefficient has a negligible influence in the process.

It is widely accepted that primary mechanism for size segregation in a shallow avalanche, where the smaller particles advance relatively unimpeded is analogous to inter-particle percolation, or kinetic sieving [33]. Separation of a granular materials via Galton board however, presents a number of advantages when compared to sieving. First, the completely passive operation of the GB makes the operation highly energetically efficient when compared to sieve separation which requires constant energy input to maintain particle flow. Second, screen clogging and eventual fouling are an inherent outcome of the sieving process, which results in additional time and energy spent towards screen recovery [94]. The GB on the other hand, would only present clogging when particle diameter is such that bridge formation plausibly obstructs the free space between consecutive pegs, this critical particle size to opening diameter ratio was reported by Roussel *et al.* as being approximately 0.3 for densely packed mixtures. Finally, a particular GB (i.e. defined board length and peg spacing) is capable of separating a variety of particle ratios (with varied rate of separation) while a particular sieve screen (with fixed mesh opening size) can only separate a material into particles larger, and smaller than the mesh size.

Inspired by this principle a device is conceived, where macromolecules flow down an inclined chute, and by action of collision with obstacles yields separation. For the purposes of particle separation, as examined here, it follows that optimal set-up will result in particle-types having significantly different terminal velocities and hence yield a good de-

gree of separation. This work makes use of Particle Dynamics (PD) simulations, using the discrete element method (DEM)[95], to look at single particle and multi-particle behavior, and experimental studies to understand and characterize the time-space trajectory of the components of a binary mixture of spherical particles. We demonstrate the possibility of achieving separation, by size or coefficient of restitution, in the direction of the flow as a result of collision driven flow. Furthermore, a probabilistic model is presented capable of predicting the expected separation for a given mixture.

3.2 SIMULATION RESULTS

Two types of computational experiments are done, (i) single particle simulations provide an insight into particle behavior inside a GB system by testing the isolated effect of different design parameters, and (ii) multi-particle simulations will provide a basis for direct comparison with experimental results, and aide the development of a probabilistic model. Multi-particle simulation experiments implement a binary mixture, with equal numbers of small and large particles; three different particle size ratios, presented in Table 3.3 are used. Pegs are modeled as static towers that are two spherical particles high, each particle having a diameter of 3.42 mm (in order to match experiments, see below). The collection bin has a depth dependent on the diameter of the large particle such that the motion of the particles is strictly limited to 2D displacement, and no overlapping is generated. The device has an inclination angle of 15 degrees with the horizontal for a typical PD simulation setup. The center-to-center distance implemented between pegs is 10.4mm.

Simulations presented in this work assume a perfectly flat non-cohesive surface for the Galton Board, as well as perfectly spherical acrylic (unless noted otherwise) beads as mixture material, in order to limit the interactions to collisions and ignore any adhesive secondary forces.

3.2.1 Single Particle studies

PD simulations are performed to obtain probability distributions of exit times of a single particle. A finite chute length of 208mm, is used in some of the simulations to reduce computational demand where it is deemed a longer length chute provides no additional information. Periodic boundaries are used in the transverse direction with a typical simulation box width of 52mm (1 : 4 aspect ratio).

For single particle simulations the moving sphere is released from a random position along the board entrance. The effect of peg diameter and spacing between pegs are analyzed by tracking the particle’s residence time distribution for 100 trials. The results are made dimensionless with the theoretical time it takes for a sphere to roll down an incline, given by $t = \sqrt{\frac{2L}{a}}$, where L is the length of the board and a is the acceleration. Results are presented in Figures 3.3 and 3.4.

The results presented in Fig. 3.3 indicate that an eight-fold increase in peg diameter (from 1mm to 8mm) results in a mere 20% shift in the residence time distribution plot. This indicates that increasing the peg size relative to the particle size has little influence on the time it takes the particle to travel the length of the chute, given that all other parameters are maintained constant.

In contrast, increasing the inter-peg gap – from the established default value of 10.4mm – has a significantly larger effect on the particle residence time. Figure 3.4 indicates how a two-fold increase (to 20.8mm) in peg spacing reduced the average residence time by half. In addition to this, the residence time distribution changed from a normal distribution to a J-shaped distribution indicating the vast majority of the particles exit in the first few seconds, having had close to no interactions with the obstacles. These results are in agreement with results presented in Bruno [84], where the relation between the peg gap and particle diameter plays a determinant role in the terminal velocity and trajectory of the particles.

Table 3.1: PD simulations- list of different dimensions and configurations tested for the GB design

Parameter	Simulation
L (pegged length)	208 mm, 679 mm, 6.79 m
W (pegged width)	varies, 52 mm typical
l_p	varies, 9.4 mm typical, same as column and row spacing
$2R_{peg}$	varies, 1.0 mm typical
$2R_p$	2 mm, 4 mm
θ	15 degrees
Initial Condition (multi-particle)	equal number fraction. lattice

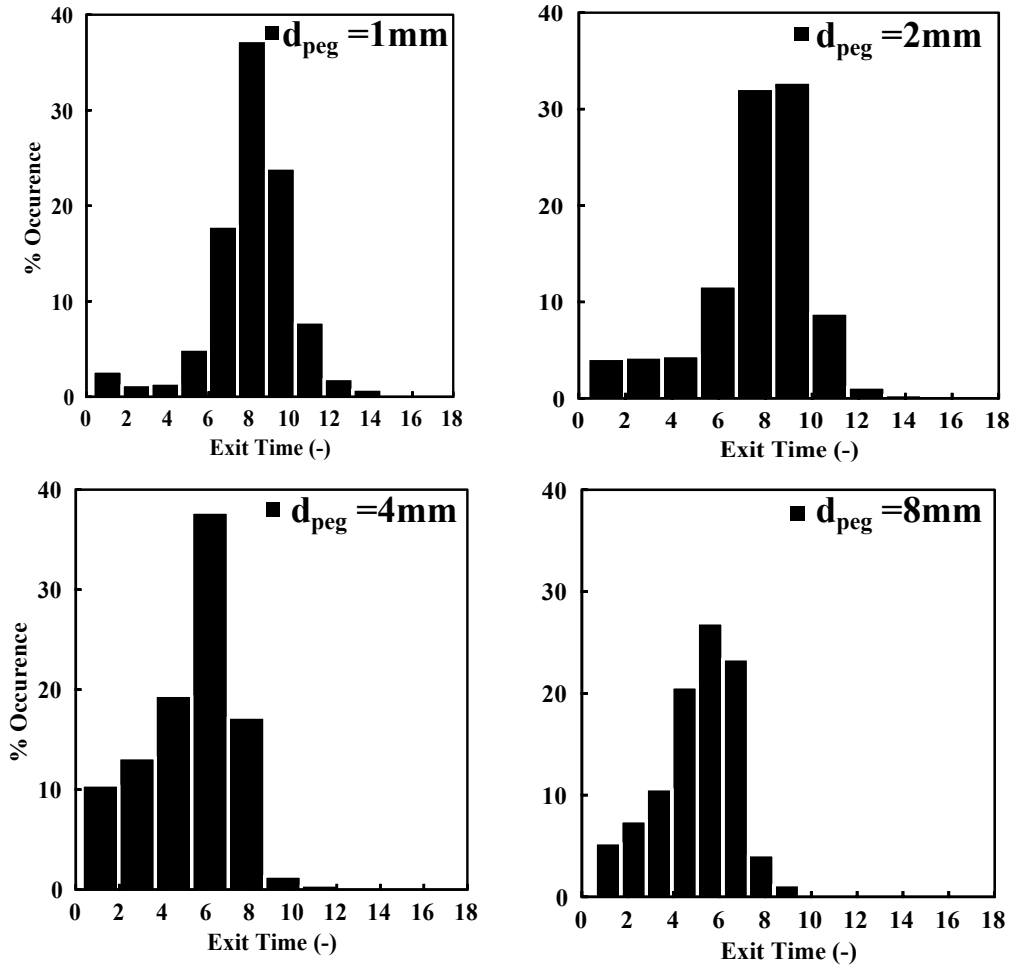


Figure 3.3: Exit time distribution for a single particle size as a function of peg diameter. A 4mm diameter particle is implemented for all of the simulations, and the free space between pegs l_p is held constant at 6.4mm which results in a constant value of $D_{eff} = 0.63$. Figure adapted from [2].

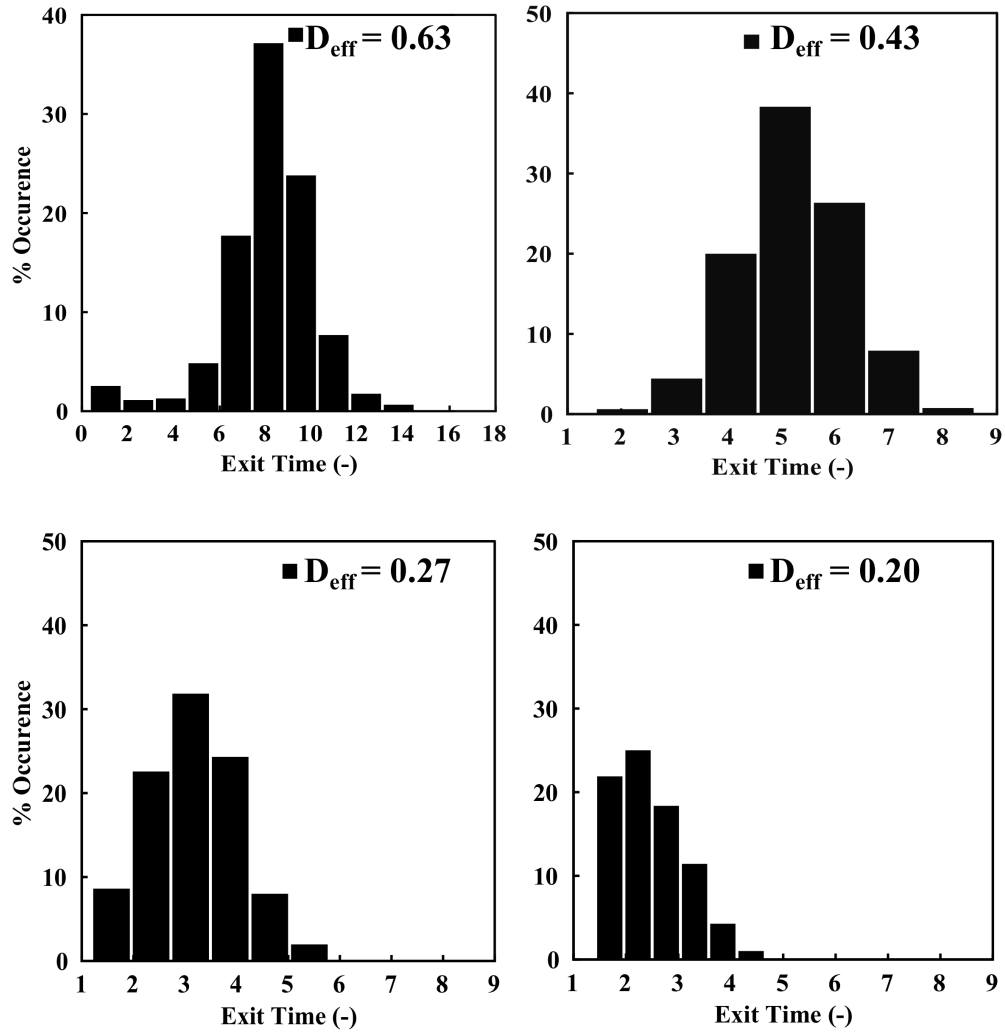


Figure 3.4: Exit time distribution for a single particle as a function of inter-peg spacing for pegs with diameter $d_{\text{peg}} = 1.0\text{mm}$ and a particle with $d_p = 4\text{mm}$. Left: $l_p = 9.4\text{mm}$. Center: $l_p = 14.6\text{mm}$. Right: $l_p = 19.8\text{mm}$. Figure adapted from [2].

3.2.2 Multi-particle results

A mono-disperse granular material comprised of either 2 and 4mm diameter particles is tested to determine the effect of multiple particles insider the system, while observing the difference in the terminal velocity attained. Particles are initially placed in a uniformly mixed monolayer lattice which covers approximately 10% of the length of the board. In the current case, a 679 mm long and 52 mm wide device is considered with 10.4 mm peg center-to-center spacing. Pegs are made from 1 mm particles.

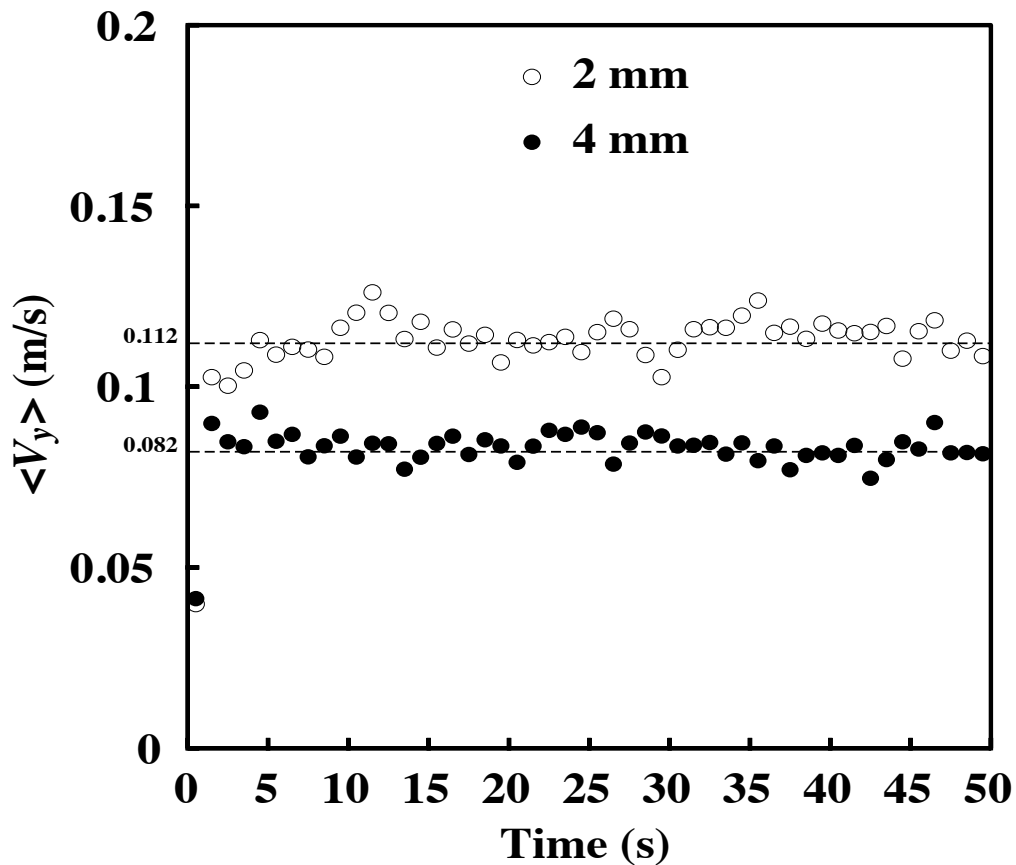


Figure 3.5: Terminal velocity as a function of time for homogeneous mixture for 2mm and 4mm diameter particles. Particles are initially arranged into a monolayer lattice covering 10% of the surface area of the board. Figure adapted from [2].

Our first multi-particles tests involve periodic chutes operated at constant particle number density. Fig 3.5 evidences the importance of the loading solid fraction; by increasing the solid fraction and releasing multiple particles at once the terminal velocity is reduced overall, given the increased number of particle-particle interactions. When analyzing single particle results we concluded that doubling the peg distance would almost double the average terminal velocity. This is equivalent to saying a granular mixture with a 2:1 ratio should display a small particle as having a terminal velocity that doubles the velocity of the larger particle. However Fig 3.5 indicates that – for the loading level used in this simulation – the result of multiple particle interactions is that the small particle travels only 20% faster than the larger one. Despite this reduction in separation efficiency, however, in general differently sized particles have a different probability of experiencing a particle-peg collision, thus resulting in a different displacement rate for each type.

To underscore this conclusion, numerical investigations are performed to examine the effect of particle loading on the extent of separation (E_s) of a mixture. The extent of separation E_s is defined in Eq. 3.3, as a function of the terminal velocities for both particle sizes.

$$E_s = \frac{(\langle V_{small} \rangle - \langle V_{big} \rangle)t}{L} \quad (3.3)$$

where $\langle V_{small} \rangle$, $\langle V_{big} \rangle$ are the average longitudinal (x) velocities of small and big (2 and 4mm diameter) particles respectively, t is the time allowed for migration, and L is the length of the device.

The extent of separation is plotted as a function of the percentage (%) of area coverage of particles (for an equal number of small and large particles) in Figure 3.6. The surface area covered by the particles is indicative of the degree of the loading of the device, and is calculated as the ratio of the cross-sectional area of all flowing particles to the non-pegged surface area of the device.

Despite the fact the extent of separation decreases dramatically as the loading (area coverage) increases, there still exists a small, but finite difference in terminal velocity even at over 30% coverage. This is explained by the augmented number of collisions a particle experiences with increased solid fraction, these results are in accordance with those reported as the collective effect by Bruno *et al.* [96, 84]. The increase in the number of released

particle creates a “short term” effect where the number of collisions in the first few instances of a run are multiplied as a direct result of the particle number density; however, as particles traverse the board they disperse and the collective effect becomes reduced.

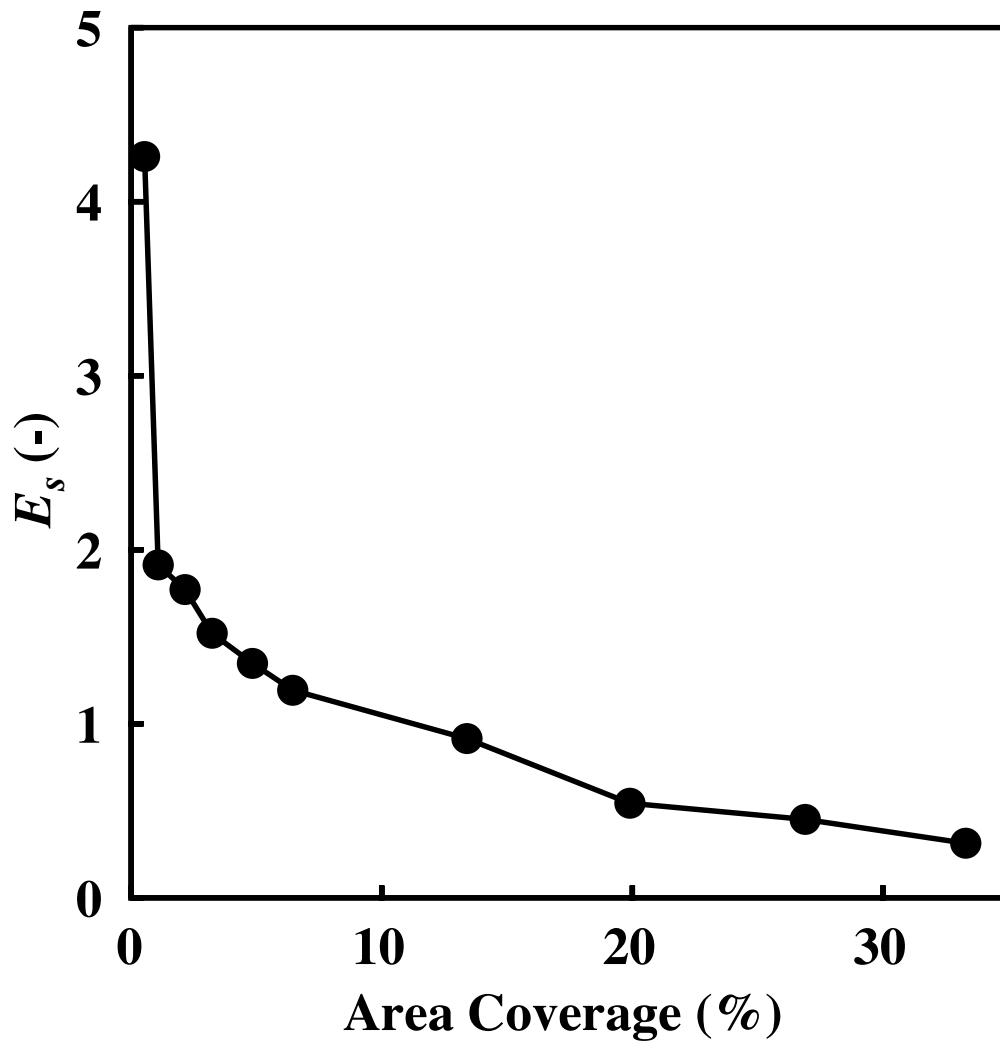


Figure 3.6: Plot for the extent of separation (E_s) defined by Eq. 3.3 as a function of the surface area covered by the mixture in the GB device. An equal number of small (2mm) and big (4mm) particles was used. Figure adapted from [2].

Table 3.2: Primary experimental and computational parameters for validating PD simulations of the Galton Board

Parameter	Experiment
L (pegged length)	757. mm
W (pegged width)	152 mm
l_p	19.0 mm, same as column and row spacing
$2R_{peg}$	3.18 mm
$2R_p$	4.65 mm, 6.9 mm, 7.8 mm
θ	25 degrees
Initial Condition (multi-particle)	equal number fraction. Semi-random(stencil)/Random lattice

Simulation particle distribution

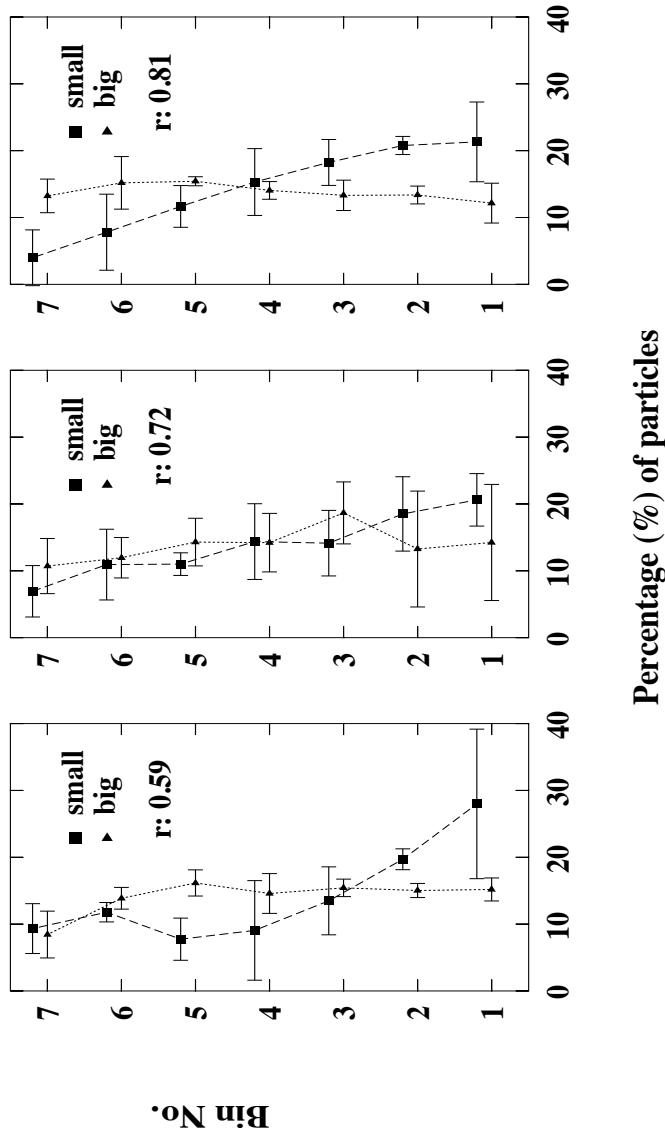


Figure 3.7: Particle distribution obtained via PD simulation along the height of the collector, for three binary mixtures. Particle and system properties are defined in Table 3.1

In accordance with this observation, as a second multi-particle test, we examine finite chute lengths whereby the number density along the board will vary as separation is achieved. As seen in Figure 3.7 the particle with the smallest diameter exits the system faster on average, and is found at the bottom of the collection bin with more frequency, whereas the “big” particle tends to be located inside the top portion of the bin for all mixture ratios. Longer simulations are run in order to determine the relation between degree of separation, for a binary mixture, as a function of particle residence time inside Galton board.

Another method of studying multi-particle flow is to examine periodic chutes that are sufficiently long that particle number density still varies. As opposed to previous, results which present the distribution along bin height for the output mixture, these present the particle spatial distribution along the length of the board at different times. For longer times, particles achieve a better degree of separation (primarily because the local number density decreases leading to higher values of the extent of separation).

From Figure 3.8 we conclude that the longer a mixture interacts with the pegs, the more likely complete segregation is possible as particles spread out further apart along the length board. For a simulation lasting only 25 seconds we observe three clearly defined regions, a region containing only a pure small beads (towards the bottom of the board, after 2.5m), a region where we can find a mixture (in the region between 2-2.5m) and a region of pure big beads (along the first 2m of the boards length). This indicates that the separation can be achieved for any two particle sizes given a sufficiently long board.

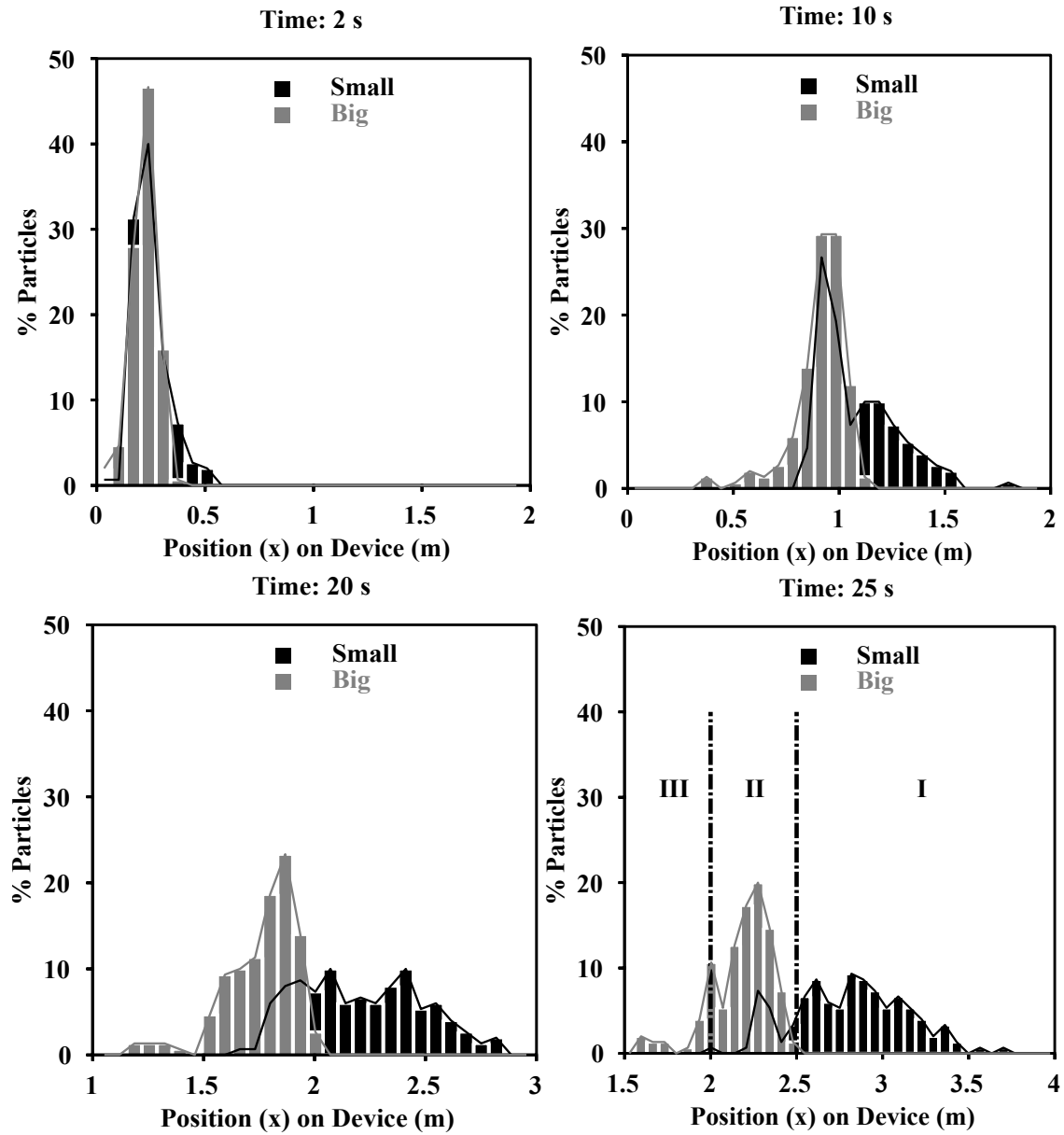


Figure 3.8: Particle distribution along the different collector bins for a binary mixture of 2 and 4mm particles at different times. Top left 2s, top right 10s, bottom left 20s and bottom right 25s. The formation of pure species regions in time is evidenced. Figure adapted from [2].

3.3 EXPERIMENTAL RESULTS: SEPARATION OF SIZE DISPERSE MIXTURES USING A GB

The Galton Board is comprised of a 1/8in thickness, perforated, polypropylene sheet (with dimensions 32in. \times 48in.), having a section covered by evenly distributed, equally spaced, identical cylindrical stainless-steel dowels of height 3/4in. The pegs are inserted into the perforation on the sheet, as per desired peg spacing. There is a total 9 columns and 45 rows of pegs, yielding a 5:1 aspect ratio for the GB. Aluminum walls enclose the system and prevent particles from bouncing outside the pegged area. The top part of the board constitutes the feeding section for the particles, and the bottom part collects the particles as they exit the system in a quasi-two dimensional bin. A mono-layer of nearly spherical particles with different material, color and size are used to observe the flow. A long rectangular plexi-glass plate placed on top of the device (supported by the side walls) acts as a cover to restrict some particles from bouncing out of the device due to collisions at higher device inclination angles.

To perform the experimental work, acrylic beads of three different diameters are selected. The beads are spherical and smooth surfaced. Table 3.3 presents the diameters (d) and effective diameters (d_{eff} ; see Eqn. 3.1) for all particles employed.

The initial condition is obtained by placing a desired number of particles in a stencil centrally-located with respect to the width of the device, as shown in Figure 3.9. The stencil is fabricated from an aluminum plate and fifteen circular holes in a 5×3 rectangular array are cut to retain the particles. To collect the flowing materials as it exits the last row of pegs, a funnel or Y shaped receptacle is placed to capture the particles as they arrive, which in turn, gives us a picture of the time dependent particle positions at exit, and hence, a measure of separation - the fastest particle (or the first to exit the device) deposits at the bottom of the collector and the slowest, or the last to arrive, deposits at the top.

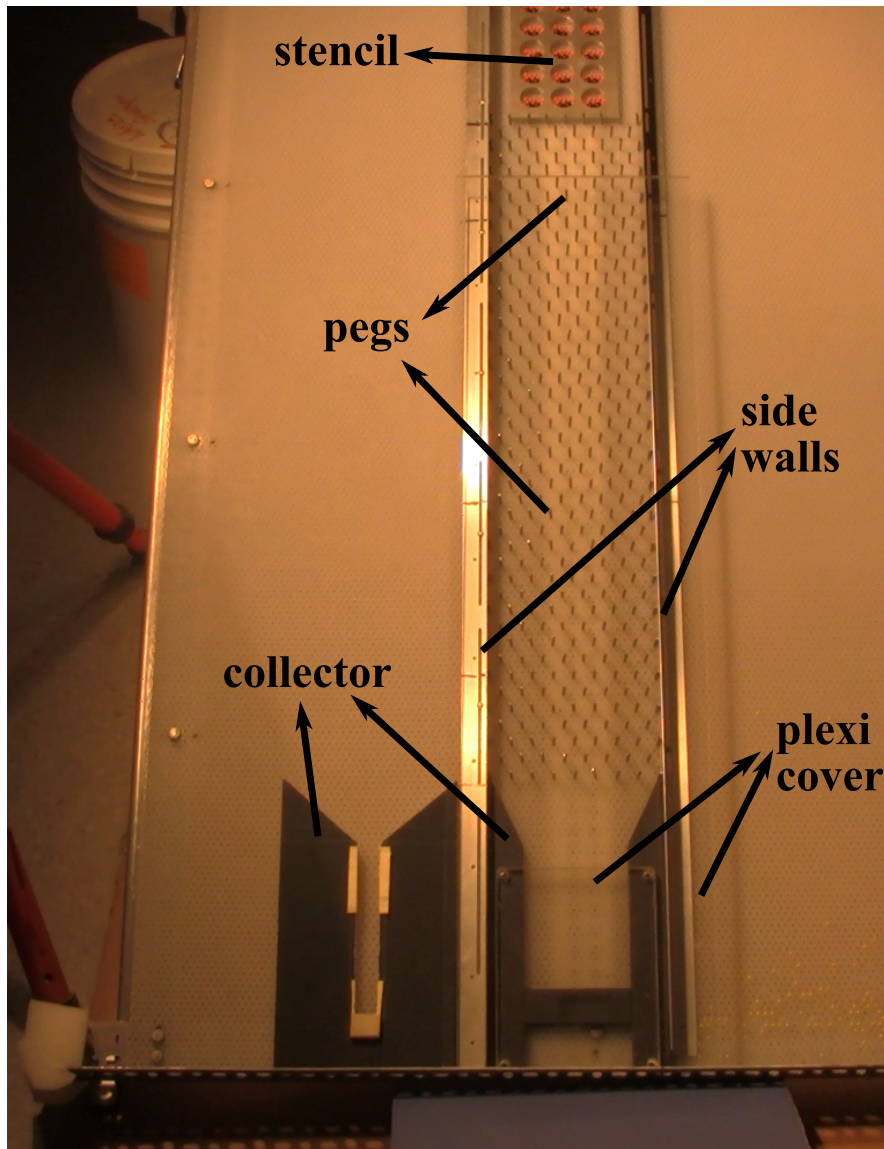


Figure 3.9: The Galton Board experimental set-up: A device to separate particles via collisional flow. To initiate a run the stencil is removed and the particles flow as a result of gravitational forces, interacting with the pegged region and ultimately being collected at the bottom. Figure adapted from [2].

A 7.8mm diameter particle is selected as the largest particle, pegs are placed along a section $L = 1\text{m}$ length, having a distance $l_p = 2.0\text{cm}$, between pegs and interleaving rows a

distance $l_p/2$. The board has an inclination of 25.0 degrees, enough to drive all the particles in a vertical flow, yet close enough to laying horizontal such that the terminal velocity of the particles is low enough that particles can be easily contained. Particles exit the pegged region by being funneled into the collector bin. The funnel walls have a 26° angle, only affecting the flow of particles close to the wall (most particles exit the galton board and roll to the bottom of the bin without interacting with the funnel walls).

Table 3.3: Mixture size ratios for mono-modal size distribution of three mixtures of acrylic particles tested. Particle and system properties are defined in Table 3.2

Diameters (mm)	d_{eff}	ratio(R_{small}/R_{big})
4.6 : 6.4	0.24 : 0.32	0.72
6.4 : 7.8	0.32 : 0.39	0.81
4.6 : 7.8	0.24 : 0.39	0.59

The depth for the outflow/collector bin is fixed just slightly greater than the maximum particle diameter (for the black spheres having a diameter of 8.6mm), forcing particles falling into the collector form a monolayer. Inside the collector particles come to a rest and are classified according to the height along the collector. The mixture contains an equal number fraction of big and small particles. Three different combinations of a mono-disperse particle mixture, having three different particle ratios- pink-black, is selected to test separation via GB. Once the enclosure stencil for the mixture is removed, the particles are free to flow down the board. A still camera (Nikon D40) is used to capture of both the initial particle arrangement in the stencil and the final arrangement in the collector. The outflow bin image is analyzed in order to quantify the correlation between distribution along the height of the bin, and particle radii with the use of images processing tools.

The distribution of particles along the length of the monolayer is a function of the particle residence time; hence, the end position of a particle along the height H of the product container is a function of the velocity at which said particles travel. In Figure 3.10 the distribution of particles inside the collector is presented for the three different mixtures.

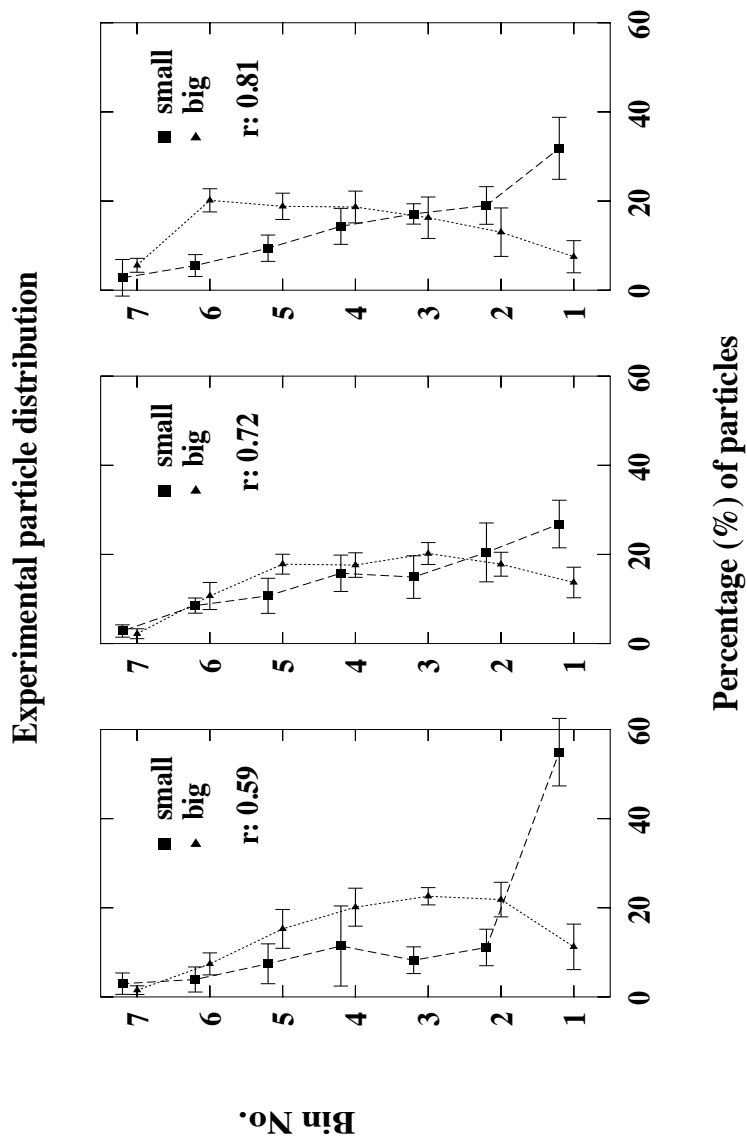


Figure 3.10: Particle distribution obtained experimentally along the height of the collector, for three binary mixtures

For the distribution analysis, the image is divided into seven horizontal bins of height $H/7.0$. The number of bins (7), was selected based on the observation that – for the particle combinations examined – the total height of the particle bed inside collector bin is roughly 7 times the diameter of the small particle, for all mixtures. The number of granules of each color is counted within each bin, then the total is divided by the total number of beads to obtain a percentage of each species per bin. Results are presented in Figures 3.10 and 3.7.

Figure 3.10 shows the distribution for each particle type in each one of the different mixtures. For all the mixtures tested, the the same pattern is observed in the collector. The smaller of the two species displays a clear tendency to exit the GB ahead of the other. These results suggest that the mixture with the greatest radii difference separate more thoroughly. We compared experimental results with simulation results for identical mixtures and operational conditions, where the separation is better as the mixture ratio increases (see Table 3.2). In addition to this it is worth noting that not only is the smaller particle most frequently localized in the bottom bins but the distribution trends for all particle mixtures present the same shape between experimental and simulation results.

3.4 STATISTICAL ANALYSIS OF RESULTS

As a quantitative comparison a two distribution Kolmogorov-Smirnov (K-S) test is performed to determine if the outflow configuration distributions for each particle size, in each mixture is significantly different between the experimental and the simulation results. The two-sample K-S test is a non-parametric hypothesis test that evaluates the difference between two sample distributions, being sensitive to differences in the location and shape of the cumulative distribution functions of the samples in question [97, 98].

The implemented K-S test function from MATLAB returns the probability (p) of distribution 1 being indistinguishable from distribution 2 with a significance, or α value of 0.05. As the p value decreases and approaches of 0 the probability of reproducing sample distribution 1 in sample distribution 2 decreases.

Table 3.4: K-S results for the analysis of distribution variance for the small and the large particle within a bi-disperse mixture

Particle ratio	p value (sim)	p value (exp)
0.59	0.129	0.423
0.72	0.806	0.883
0.81	0.423	0.883

Table 3.4 shows the calculated p value for a K-S test to determine the difference in distribution between the small and large particle within each of the mixtures tested (including both experimental and simulated results). In this scenario we are looking for a small p values to indicate that the probability of these distributions being identical is low (or that there exists a statistically significant degree of separation between the species). It can be observed that the lowest p was obtained for the simulation of the 0.56 ratio mixture; whereas the largest p value of 0.88 was obtained for two out of the three experimental results. For all the mixtures it is true that the small to large particle distributions are more similar for the experiments than the simulations; in part, this is the result of the experimental error created by partial overlap of particles inside the collector bin.

Table 3.5: K-S results for the analysis of distribution variance between experimental and simulation results for each particle size, and for each mixture tested

Particle ratio	p value (small)	p value (large)
0.59	0.5189	0.5189
0.72	0.9290	0.5189
0.81	1.0	0.187

Table 3.5 presents the results for the comparison of the distribution of each type of particle obtained from experimental and computational runs. That is, here we compare how similar our results are for the experimental versus simulated cases (for both the small particles and the large particles). In this scenario a large p value is desired to indicate how similar the average distributions are. In general the distributions for the small particle are more likely to be identical between simulations and experiments. However the distributions for the larger particle have a 50% probability or less of being identical between simulation and experiments.

Finally, the velocity distribution for a mixture with particle diameter ratio 0.72 was calculated from experimental videos. Figure 3.11 shows the mode of the distribution is found around 0.141 for the small particle, with $d_{eff} = 0.24$, and at 0.106 for the large particle (with $d_{eff} = 0.32$). This results in a velocity that is 10% higher for the smaller particle in this case (in qualitative agreement with simulations from Figure 3.5).

3.5 MODEL

As mentioned above, we anticipate that particle separation can be induced via two mechanisms: first, by varying the probability of peg-particle collisions (by changing particle size), but also, second, by varying the *influence* of each peg-particle collision (by changing the particle properties). In order to assess this hypothesis, here we propose a time-based probability model in order to predict the terminal velocity for a species as a function of both the effective diameter as well as the coefficient of restitution (COR). In other words, the algorithm takes the particle position and calculates the terminal velocity a particle would attain by calculating the probability for this particle to collide with a peg for every row of pegs in the system.

Starting at time $t = 0$ and $V = 0$ we choose a random position for the *center of mass* of the particle (that lies somewhere along the distance between two pegs). Based on this position and the value of d_{eff} , we determine whether flow would result in a collision with a peg. If so, a *bounce time* is added to the time spent in free-fall prior to allowing this particle to pass the current row of pegs. The bounce time is assumed to be the equivalent to the time it would take the particle to bounce up and then return to the current peg location/height.

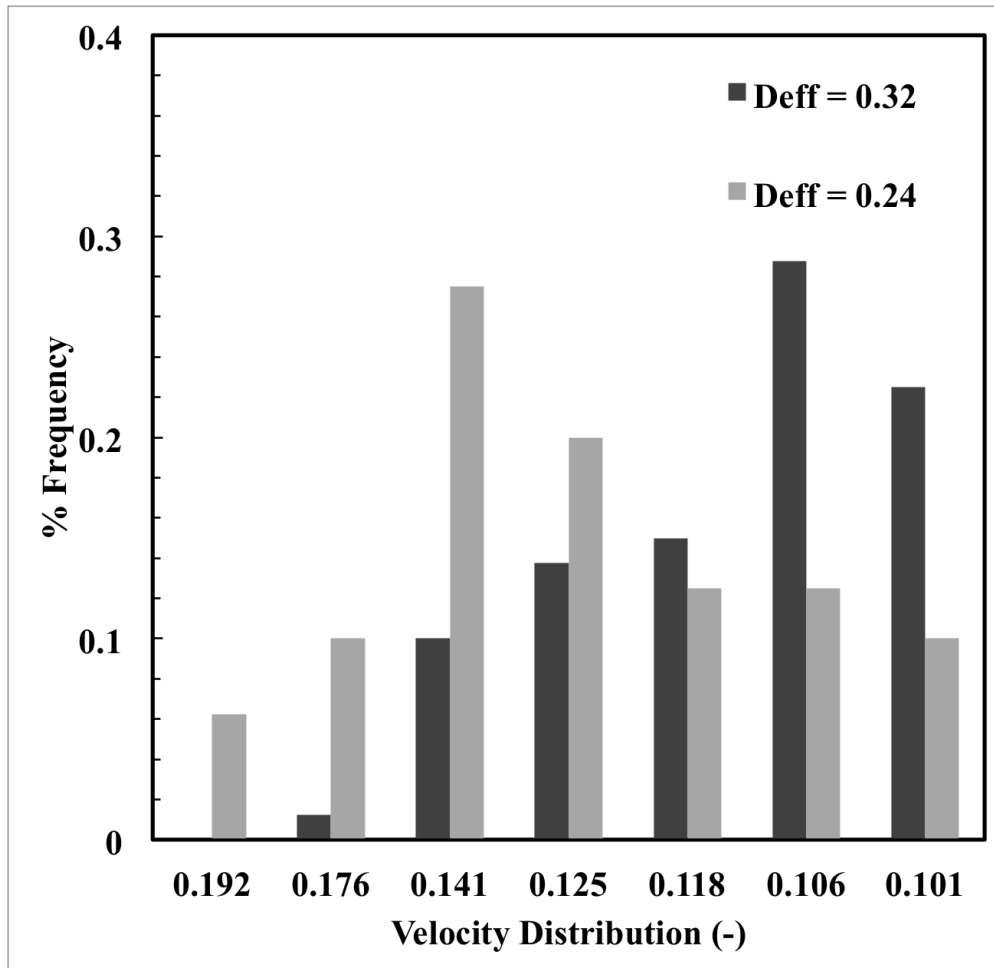


Figure 3.11: Particle terminal velocity distribution for mixture ratio = 0.72, extracted from experimental separation videos. Velocity is made dimensionless with the unimpeded rolling time of a sphere down an incline

Assuming ballistic flight following a collision, the bounce time (t_b) is calculated as $t_b = V_b/a$, where V_b is the rebound velocity, a is the particle acceleration, Δl is the distance traveled between successive collisions and $V_0 = 0.0$ for the first step and then becomes $V_0 = V_b$ for subsequent steps.

$$V_f = V_0 + at \tag{3.4a}$$

$$t = \sqrt{\frac{2\Delta l}{a}}, \tag{3.4b}$$

The distance between consecutive rows of pegs is given by $H_p = l_p \sin(\pi/3)$. The transit time is calculated from Eq. 3.4b for a sphere falling down an inclined plane of length l and angle θ with the horizontal. Here a is the acceleration of the sphere and is equal to $\vec{g} \sin \theta$. In the present work average terminal velocities are calculated using this model by testing the probability of incidence with a peg, once for each of the 100 rows. This process is repeated 50 times for each particle size, for each of the fictional materials selected, defined by a constant coefficient of restitution value. These trends are then compared with results for additional single particle simulations inside an infinitely long GB in order to assure the terminal velocity is captured.

The COR values presented were selected according to the impact velocities measured in the preceding simulations and further determination of the COR value at said impact velocities from Fig. A1. As one can see, the results of our probabilistic model are in qualitative agreement with the PD simulations both as a function of particle size and material properties.

CH.?? contains details on the PythonTM algorithm for the probability model.

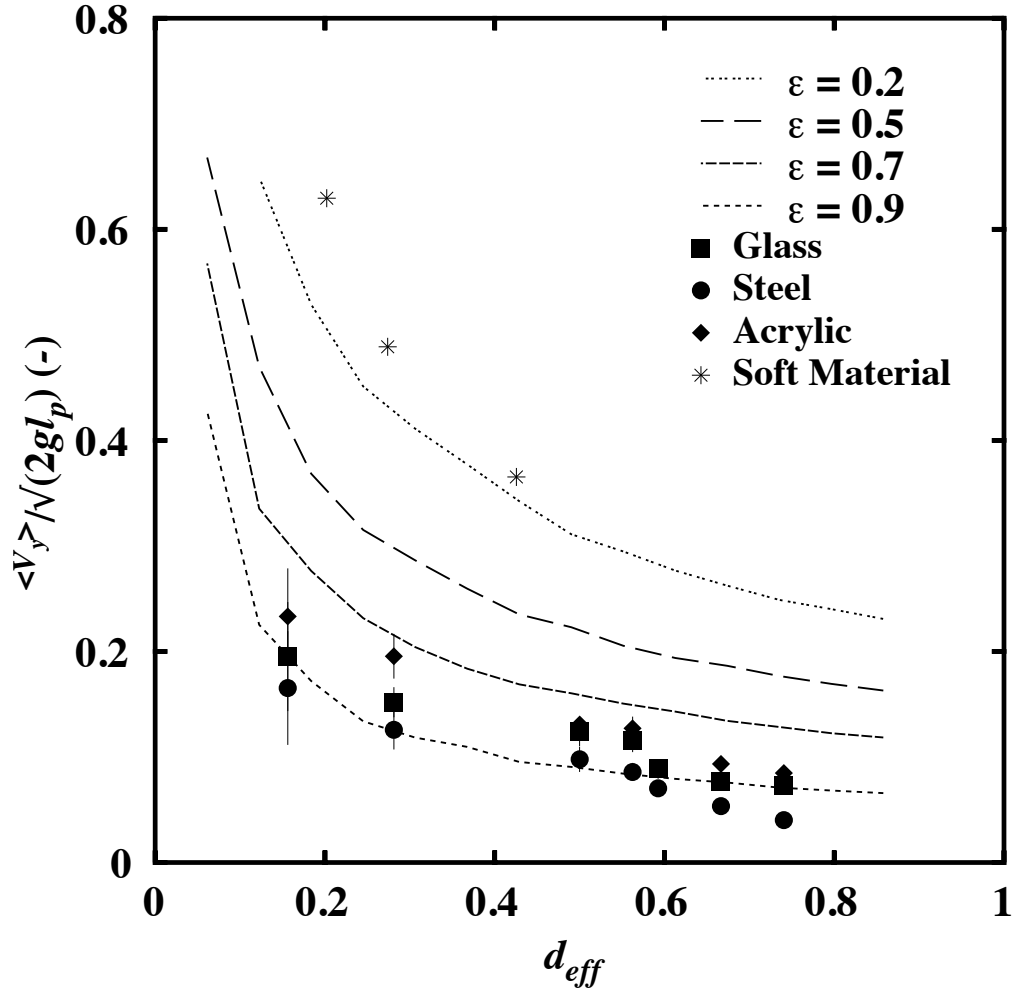


Figure 3.12: Average terminal velocity profile for fictional particles with coefficient of restitution of 0.5, 0.7, 0.9 according to probability model compared with a PD simulation based terminal velocity. Soft material results were extracted from the single particle simulations, where a fictitious material with a low coefficient of restitution is tested.

3.6 SUMMARY AND OUTLOOK

While segregation is often an undesired effect, sometimes separating the components of a particle mixture is the ultimate goal in many industrial processes. Rate-based separation processes hold promise as both green and less energy intensive, when compared to conventional particle separations technologies such as vibrating screens or froth flotation methods. In this work, it has been demonstrated for the first time, that a device inducing diffusive motion to the constituents of a mixture by way of gravity-driven collisional flow through an array of obstacles can be used to separate particles effectively, without an external energy input.

The effects of various design and operating parameters on the extent or quality of separation are investigated by means of a simple single particle model along with experiments and DEM simulations. It has been found that the ratio of the particle size to the available gap between two obstacles (called effective diameter or d_{eff}) is a key parameter controlling the separation. This parameter is also a measure of the probability of a particle colliding with a peg. Qualitative results confirm smaller particle travels length of the board faster on average. Separation is achieved for all particle mixtures, despite some mixtures having particles whose size is only 20% smaller.

Increasing the board length results in an increase in the number of particle-peg interactions and results in a better degree of separation. If a long enough board is provided any mixture can yield good separation in a GB. The model provided can help determine the necessary peg spacing and board length for any particular system. The extent of separation deteriorates as the loading fraction of the device is increased due to relatively high number of dissipative collisions for all types of particles, which effectively reduce their relative mobility (in the extreme case, jamming occurs). Realization of a complete theoretical model to predict the length (L) or time (t) required for obtaining a desired extent of separation in a particular device with a given design and operating parameter is still elusive and could be the topic of future research.

4.0 DYNAMIC SEPARATION OF A BINARY MIXTURE USING COHESION: THE GRANULAR CHROMATOGRAPH

4.1 INTRODUCTION

The process of separation/purification is a routine task across many industries (e.g. chemical, pharmaceutical, food, metallurgical), and its naturally occurring analogue- segregation, is ubiquitous to the handling of granular materials. However commonplace solid separation is to industrial processes, conventional separation units such as sieving, are often highly energy intensive, and/or environmentally unfriendly as in froth flotation [99, 100]. Vibrating screens and sieves require an energy input during separation, and de-clogging stages, as well as during the recovery of the screen at the end of each batch. Chevoir *et al.* [101] studied the geometrical properties that lead to the jamming of mixtures flowing through obstacles, and mathematically demonstrated that clogging is inevitable when the screen opening size was equal or less than three times the particle diameter of the small particle. Hence, a typical screening process is prone to clogging *by design*. Moreover, industrial vibrating screens can weigh thousands of tons when loaded with materials, therefore the continuous shaking of the screen requires high energy input.

Vibrated beds have long been studied in the context of granular materials, for vibration is one of the better known dynamic forces to induce segregation [18, 9]. Ahmad *et al.* [19] stated that even for more or less uniform particle mixtures, there exist a tendency to separate into its individual constituents once it is subjected to vibration. A variety of different experiments have been performed by different groups in order to observe segregation patterns in vertically vibrated systems, such as simple cases where a single intruder-type particle is placed inside a uniform bed of smaller particles, or more complex systems comprised of bi-disperse particle

mixtures [54]. Studies to determine the effects of vibrational forces on granular systems have made an attempt at characterizing the parameters that primarily influence the end distribution of the system [21]. Three main segregation mechanisms have been identified for vibrational systems: (i) geometrical reorganization, (ii) size percolation, and (iii) convection [61]. Shinbrot *et al.* [20] observed that convection rolls form along vibrated granular beds and explained the single intruder phenomenon, in which a more massive particle makes its way to the top of a bed of ‘smaller’ particles and remains at the top in the presence of vibrated flow, as being a result of particle inertia. Single intruder segregation has been attributed to more than one phenomenon; both percolation and convection have been identified as the operating mechanism for this type of scenario [102]. A dimensionless acceleration parameter (Γ) has been accepted to characterize a vibrated granular system and is defined by the equation (2.11).

Cohesion on the other hand, has been employed as an aide to induce a desired degree of mixing in a number of studies [11, 6, 103, 52]. Cohesion in granular materials can arise from a variety of inter-particle forces such as van der Waals, electrostatic, magnetic, and capillary – through the formation of liquid bridges [61]. This work is concerned with the latter, and when using the term cohesion henceforth it will refer to the presence of liquid-bridge induced capillary (and viscous) forces. Hsiau & Yang studied self-diffusion and mixing of particles by combining both cohesive forces and vibrational forces [104]. They implemented Discrete Element Method (DEM) simulations, with contact mechanics equations and capillary force model equations. The force exerted by the liquid bridge arising between two colliding particles was calculated using the toroid approximation to describe the geometrical shape of the meniscus, while neglecting the buoyancy and gravitational force. Johanson *et al.* [102] on the other hand, presented a quantitative analysis of particle segregation mechanisms and concluded that for a mixture of fine and coarse particles, the segregation potential is reduced for by the addition of a critical volume of a binding fluid. However, an increased degree of segregation can be observed for a minimal (0.1%) oil content, even when the percolation velocity is effectively zero. This is attributed to the formation of capillary bridges that preferentially bond fine-fine particles over fine-coarse pairs.

Yang [61] offers a model to represent the combined effect of vibrational energy and cohesive forces due to the presence of a fluid. The observations reported reveal there is an optimal fluid volume that allows for manipulation of the degree of mixing, or unmixing. This supports the finding presented by Li *et al.* [12, 105] where they introduce a phase diagram outlining regions where the presence of a fluid results in segregation being alternatively enhanced or mitigated. Strauch & Herminghaus [3] reference a dimensionless excitation value Ξ – a ratio of the vibrational energy of the system to the energy required to rupture a capillary bridge – described by the equation:

$$\Xi = \frac{mA^2\omega^2}{2W_{tot}}, \quad (4.1)$$

where m is the mass of the particle and W_{tot} can be calculated by integrating the capillary and viscous force with respect to the separation between particles (a quantity often called the “work of adhesion”). A fluidized state is necessary in order for particles to displace as a result of vibrational forces, and minimum a critical acceleration (Γ_{crit}) is necessary for this to take place. Under dry conditions Γ_{crit} has been found to be around 1.2 [5, 6], while a minimum value of 1.5 has been reported as being necessary to observe fluidization in wet systems [3].

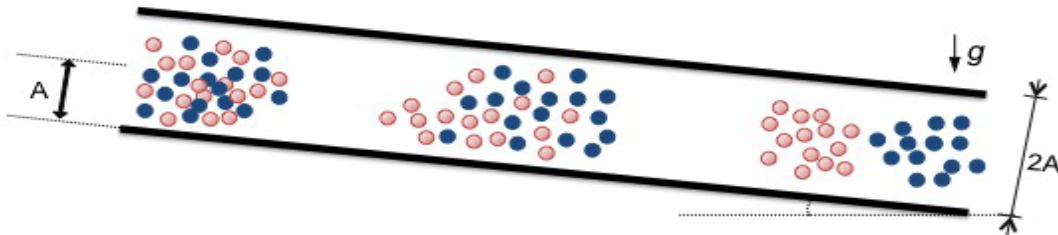


Figure 4.1: Sketch of the operation of a dynamic granular chromatography column, where A is the vibrational amplitude. The distance between top and bottom wall is $2A$.

Dynamic rate-based separation refers to the separation of particles based on their displacement rate within a system with constant energy influx. In this case, the driving force for separation will be the induced differential in kinetic energies for the particles themselves as a result of the interaction with a fluid and the vibrating surface. This work makes use of the so-called soft particle, or soft sphere model of DEM simulations. A soft particle method is commonly applied to complex systems with multi-particle collisions, significantly lengthy contact times and particle deformation.

It is the objective of this work to simulate a fluid-solid system that can be employed as a separation unit for granular mixtures by exploiting the conditions for completely inelastic collisions. By selecting a fluid and a vibrational speed, a density disperse binary mixture can separate into its components as they traverse a channel in varying amounts of time. This approach is analogous to the separation of different chemical species in a gas chromatography column, where differing adsorbent selectivity impedes the displacement of a single component of the mixture. Our system, which we call the dynamic granular chromatograph, is depicted in Fig. 4.1. To our knowledge, no reports have been published to date that implement the competition between vibration and capillary/viscous forces to successfully induce a rate differential intended to separate density disperse granular mixtures.

4.2 MATERIALS AND METHODS

The mechanical properties of the particles simulated are summarized in Table 4.1. These materials in particular were selected due to the density ratio between them, which is roughly 3:1 for glass and steel mixtures. All particles are assumed to be perfectly spherical with a radius $R = 4.5\text{mm}$.

Water and silicone oil with a viscosity of 200cSt were implemented in simulations in order to isolate the effect of liquid properties on separation, particularly viscosity and surface tension (refer to Table 4.2).

Table 4.1: Material mechanical properties for the glass and steel spheres simulated.

Material	Density (kg/m^3)	Young's Modulus (Pa)	Poisson Ratio	Yield Stress (Pa)
Glass	2700.0	68.95e9	0.33	68.95e7
Steel	7900.0	193.0e9	0.29	265.7e7

4.2.1 Simulation Parameters and Boundary conditions

The system simulated is comprised of a horizontal column, with a rectangular cross-section, that is being vertically vibrated. The length L_{col} of the column is defined in terms of a the particle radius, keeping $L_{col} \gg R$. The spheres are subjected to a collision driven flux along the length of the vibrating column. In order to vibrate the column, the boundaries are given a sinusoidal trajectory with a defined frequency (f) and amplitude (A), where the position for the top and bottom wall are given by $y = A \times (1 - \cos(f * 2\pi t/60))$. The influx of vibrational energy can be modified by defining A and/or f . From here on the amplitude term used to characterize a system will be presented in its dimensionless form A^* , where $A^* = A/R$.

Every interaction between the spheres and the walls creates a capillary bridge that is elongated as the particle bounces, following the particle's rebound trajectory. If the energy after impact is high enough to overcome the capillary and viscous forces, the bridge is ruptured and the particle continues its free-flight path. Boundaries in the direction of flow (taken here to be the 'x' direction) are defined as continuous, allowing for particles to exit the system, and be automatically re-introduced at the starting point, creating constant flow density. The other boundaries are solid, smooth surfaces. Interaction with smooth boundaries are estimated as interactions with a solid having an infinite radius $R = \infty$.

In addition to a constant energy influx, all surfaces are assumed to be homogeneously coated with a thin liquid layer. Every single collision between a particle and its surroundings, be it system walls or other particles, results in the formation of a liquid bridge. The liquid volume available for bridge formation has been defined at a constant value of $\hat{V} = 0.005$,

Table 4.2: Fluid properties for water and Silicone oil at room temperature.

Reference	Surface Tension (N/m)	Viscosity ($Pa\cdot s$)
Water	0.0728	0.001
200cSt	0.021	0.193

characterizing the system as being in the pendular saturation regime. The separation between top and bottom wall is defined as $2A^*$. The column has an inclination angle with respect to the horizontal of 5° to ensure that there is no backflow of particles, see Fig. 4.1.

4.3 GRANULAR CHROMATOGRAPH: RESULTS AND ANALYSIS

4.3.1 Single particle simulation

A series of single particle simulations are performed to observe how the expected terminal velocity for each granular species relates to Γ and Ξ . For each set of system parameters three different initial conditions are defined. In each one a random position and velocity is assigning to each particle and the resulting (typically steady) average velocity is the value reported. Continuous boundaries in the direction of flow and a total running time of 40 s ensure a small standard deviation.

Preliminary simulations indicated neither steel nor glass particles were able to become fluidized for $\Gamma \leq 1.6$ in the presence of interstitial liquid. This is in agreement with reported literature values [3]. Tables 4.3 and 4.4 list the system parameters tested for silicone oil and water, respectively.

Table 4.3: Vibrational energy parameters tested for 200cSt silicone oil single particle simulations.

Γ_i (-)	f (RPM)	A^* (-)	V_{wall} (m/s)	Ξ Steel (-)	Ξ Glass (-)
$\Gamma_{o1} = 1.6$	90	20	1.7	23.5	8.0
$\Gamma_{o2} = 2.0$	100	20	1.9	26.1	8.9
$\Gamma_{o3} = 4.0$	200	10	1.9	26.1	8.9
$\Gamma_{o4} = 5.3$	200	13	2.5	34.0	11.6
$\Gamma_{o5} = 8.1$	200	20	3.8	52.3	17.9
$\Gamma_{o6} = 9.1$	300	10	2.8	39.2	13.4
$\Gamma_{o7} = 11.8$	300	13	3.7	51.0	17.4
$\Gamma_{o8} = 18.2$	300	20	5.7	78.6	26.8

From the dimensionless excitation values calculated, it is evident that the movement of steel is expected to be minimally affected by the presence of the fluid. In Fig. 4.2 the terminal velocities v_f attained for each trial are calculated, plotted with respect to the corresponding Γ and compared to the results in the absence of fluid. As expected, the terminal velocities for the steel particles were larger than the ones for glass across the board, which is attributed to the higher coefficient of restitution for steel in the dry cases, whereas in the wet cases the particle mass and contact angle are the determinant factors.

Conditions for water simulations required small values of A^* in order to balance a Γ value greater than 1.6 while restricting Ξ to values smaller than 300, where the forces associated with the liquid binder are significant compared to the vibrational forces. This constraint on vibrational amplitude forced an adjustment in the separation between the top and bottom wall. For these simulations, the separation was defined as $2 + 2A^*$ (one particle diameter and two dimensionless amplitudes).

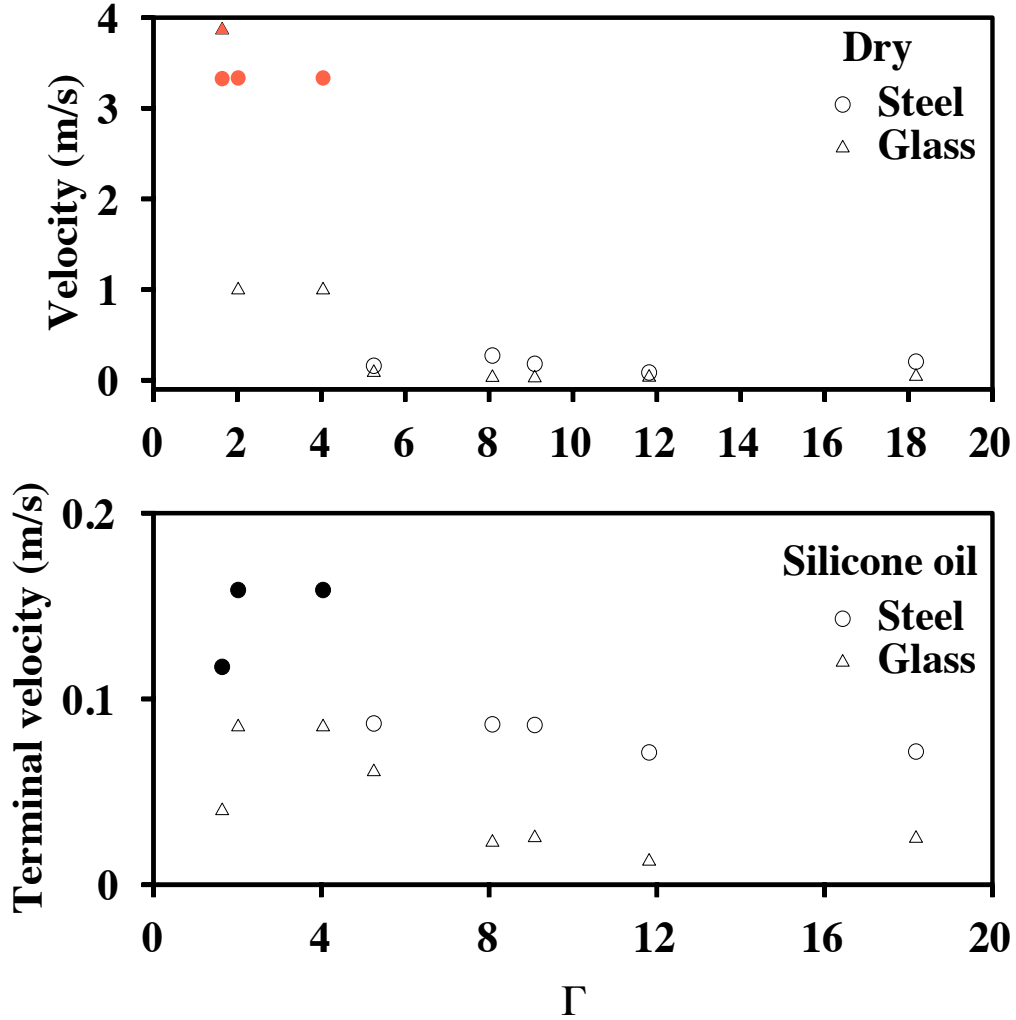


Figure 4.2: Terminal velocity attained by steel and glass particles as a function of Γ employing silicone oil as the fluid (below) and compared with dry conditions (above). The open symbols represent conditions where particles collided with the top wall of the system, whereas filled (black) symbols represent conditions where no interaction with the top wall was observed. The red symbols represent instantaneous velocities for conditions where a steady state velocity was not achieved. The Ξ values and their corresponding to each vibrational frequency are listed in Table 4.3. Standard deviation for all conditions that reach a terminal velocity is smaller than the data symbol size.

As with the oil case, Figure 4.3 depicts the (terminal) velocities obtained under varying system parameters. We should note that, for several of the trials in each figure (Fig. 4.2 and 4.3), truly terminal velocities were not achieved in some of the dry conditions due to the fact that the frictional and collisional dissipation was too small to balance the gravitational energy.

Table 4.4: Vibrational energy parameters tested for water single particle simulations.

$\Gamma_i(-)$	f (RPM)	A^* (-)	V_{wall} (m/s)	Ξ Steel (-)	Ξ Glass (-)
$\Gamma_{w1} = 2.3$	300	2.5	0.7	188.5	64.4
$\Gamma_{w2} = 2.3$	300	3.0	0.8	266.2	91.0
$\Gamma_{w3} = 2.4$	400	1.5	0.6	123.1	42.1
$\Gamma_{w4} = 1.8$	600	0.7	0.4	61.8	21.1
$\Gamma_{w5} = 3.8$	500	1.5	0.7	188.5	64.4
$\Gamma_{w6} = 4.0$	400	2.5	0.9	324.5	110.9

These particles are highlighted as the red filled symbols in the plots. The terminal velocity is the combined effect of four components: (1) The Γ value, (2) The wall energy, (3) the fluid effect, and (4) the wall separation. Dry conditions that accelerate indefinitely are typically the result of conditions where the particles do not reach the top wall.

The trends observed in the wet terminal velocity suggest there is a value of vibrational energy above which the increased number of collisions with the system walls will offset the additional energy supplied through vibration creating an asymptotic value where $v_f \rightarrow 0$ as $\Gamma \rightarrow \infty$. The differences in terminal velocity for the dry cases when compared to the wet cases highlight the impact of liquid bridge formation on displacement. The terminal velocity is an indication of the potential for separation between the two species, where the greater the difference between v_f the more rapidly and efficiently separation will occur.

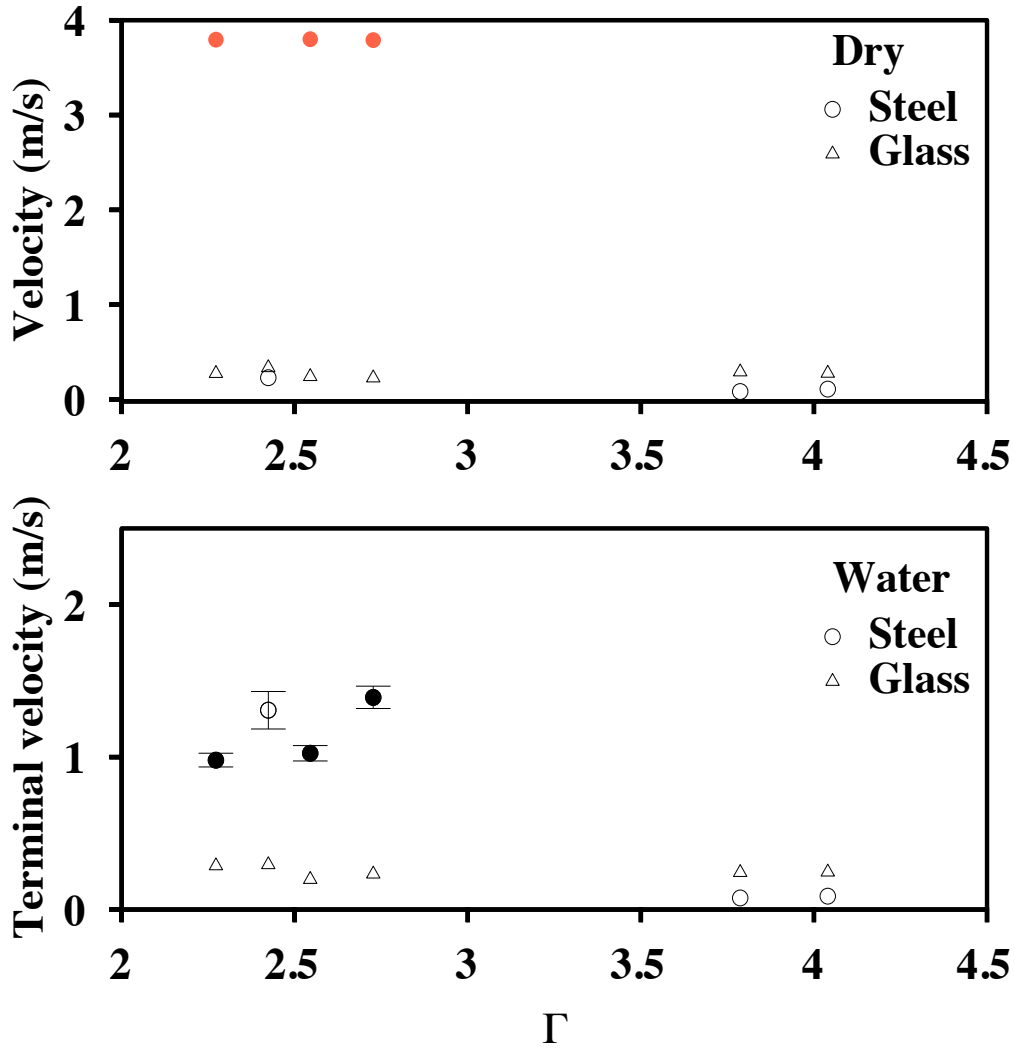


Figure 4.3: Terminal velocity attained by steel and glass particles as a function of Γ employing water as the fluid (below) and compared with dry conditions (above). Open symbols represent conditions where particles collided with the top wall. Filled symbols represent conditions where no interaction with the top wall was observed. The red symbols represent instantaneous velocities for conditions where a steady state velocity was not achieved. The Ξ values and their corresponding vibrational frequency are listed in Table 4.4. Error bars were included for those conditions where the variability was bigger than the symbol size.

From the plots of the single particle results a set of conditions for both silicone oil and water were selected for the (multi-particle) separation simulations. The criteria to select conditions expected to yield separation are: (i) the energy lost to liquid bridge rupture is significant relative to the input energy (i.e. small values of Ξ) for at least one of the species, and (ii) single-particle terminal velocities are significantly different for the species involved. The chosen separation condition defines Γ_{o2} with a ratio of $v_{f_{steel}}/v_{f_{glass}} \approx 2$ and Γ_{w2} with $v_{f_{steel}}/v_{f_{glass}} \approx 5$.

4.3.2 Multi-particle simulations

A random binary mixture comprised of equal fractions of glass and steel particles, is placed as a monolayer of particles at the entrance of the chute. Continuous boundaries in the direction of flow allow for the evaluation of separation in an effectively infinitely long unit.

Figure 4.4 shows the separation of a mixture at condition Γ_{o2} for silicone oil. It is evident that as early as 10 seconds into the simulation there are two distinct species clusters moving at different velocities. At 15s the mixture has separated into two pure species clusters. At 20s the clusters have acquired spatial separation, and any additional time inside the system will yield further spatial separation. The high viscosity of the silicone oil enables separation to take place in a short distance.

Conversely Fig. 4.5 shows the dry displacement for the same mixture and conditions. While we note that separation of the mixture can also be achieved in dry conditions, a longer chute is required in this case. We hypothesize that the separation mechanism in each of these cases is different, yet complementary. That is, in each case there is a balance between dissipation and energy input; however, in the case of the dry system the dissipation is solely due to the coefficient of restitution (COR), while in the wet systems the COR plays a significantly smaller role (but the particle mass is dominant). This hypothesis will be explored in more detail below.

Figure 4.6 shows that complete separation, using water at condition Γ_{w2} , can be attained in as little as 10s. This requires chute length of 10 m, longer than one required when using silicone oil, but shorter than the ≈ 20 m necessary to separate the dry case at Γ_{o2} . This can

be explained by the difference in Ξ for the two wet cases, where the dimensionless excitation energy value is effectively one order of magnitude smaller when using silicone oil than water. This means less energy is lost to fluid forces when using water than silicone oil, therefore displacement is faster in water for both species. This is evident when comparing the values of dimensionless excitation energy for the two cases. For the dry simulation at Γ_{w2} on the other hand, no separation was achieved (Fig. 4.7).

The terminal velocity attained for the single-particle simulations is smaller than that of

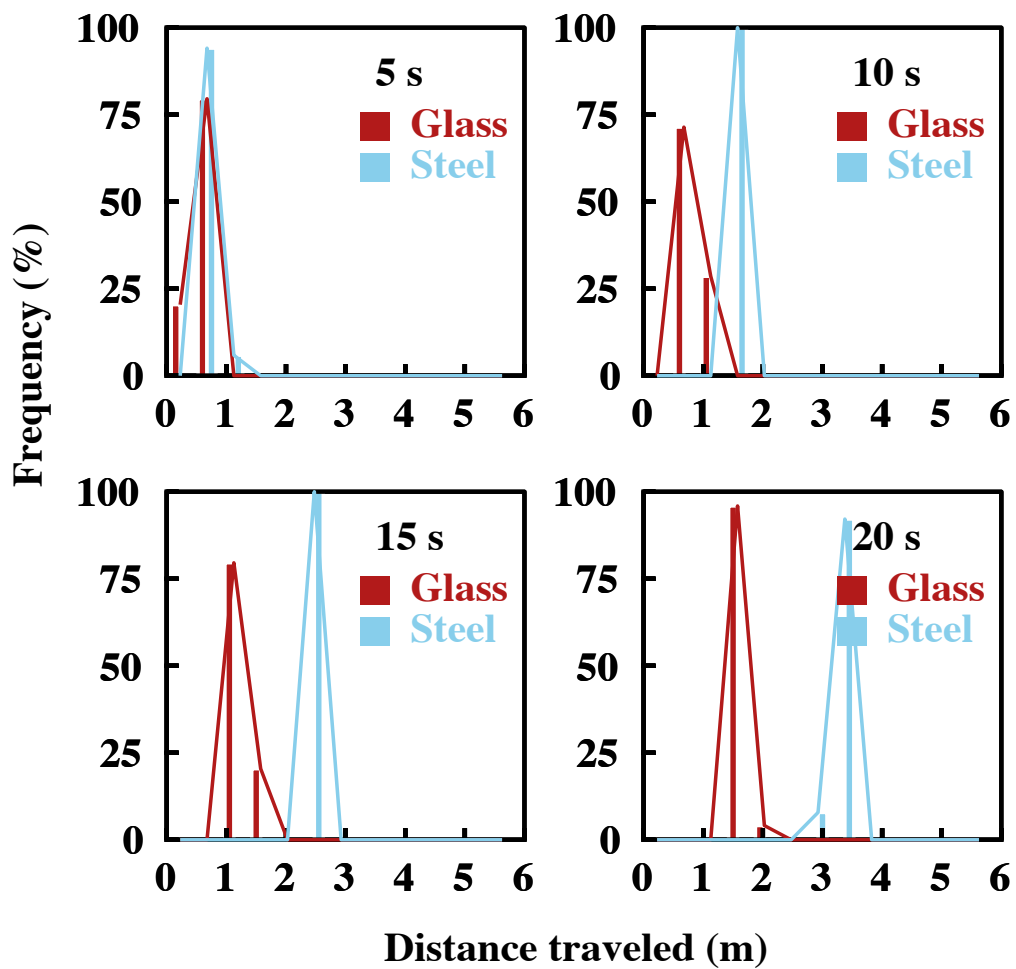


Figure 4.4: Time evolution for the separation of 100 particles, comprised of a 50-50 number fraction of steel and glass particles employing silicone oil at Γ_{o2} . The parameters associated for vibration can be found in Table 4.3.

the multi-particle simulations for all conditions and materials considered. Glass yielded a greater velocity increase than steel possibly as a result of the combined effect of (1) particle clusters formation that more easily overcome the fluid effect, and (2) an increased number of collisions with other more energetic particles. Steel, being the more massive of the two species is therefore less sensitive to the presence of the fluid and other particles, resulting in a smaller net change in velocity. Additionally, the pure clusters formed for silicone oil present a smaller spatial distribution than those formed in the water simulations.

In order to verify that the dry separation observed in Fig. 4.5 is a result of the difference in COR, additional mixture simulations were run at condition Γ_{o2} . In this circumstance, however, the mixture was comprised of two differing “species” of glass. While each species has a different density – *glass*₁ had density $\rho_1 = 2700kg/m^3$ while *glass*₂ had density $\rho_2 = 8100kg/m^3$ – all other properties were kept the same as those presented for glass in Table 4.1.

The results presented in Fig. 4.8 and 4.9 are as expected: in the presence of fluid separation between the two types of glass was achieved, whereas in the dry condition no separation is visible. This confirms the notion that for wet cases the mass of the particle is the determinant property in the terminal velocity. In contrast, for dry cases the coefficient of restitution will primarily determine the feasibility of separation.

Larger simulation comprised of 2400 particles of equal number fraction of glass and steel were studied to compare the results to those obtained in the 100 particle simulations. In these cases the initial condition is a double layer rectangular array.

Increasing the total number of particles by a factor of 20 we observe that the time it takes to achieve separation increases. This is in agreement with the observed steady state velocity analysis when comparing a single particle to the (100) multi-particle simulations. This increment is attributed to the increased number of collisions resulting from the higher particle density. However, both vibrational conditions and fluids tested still yield the expected separation.

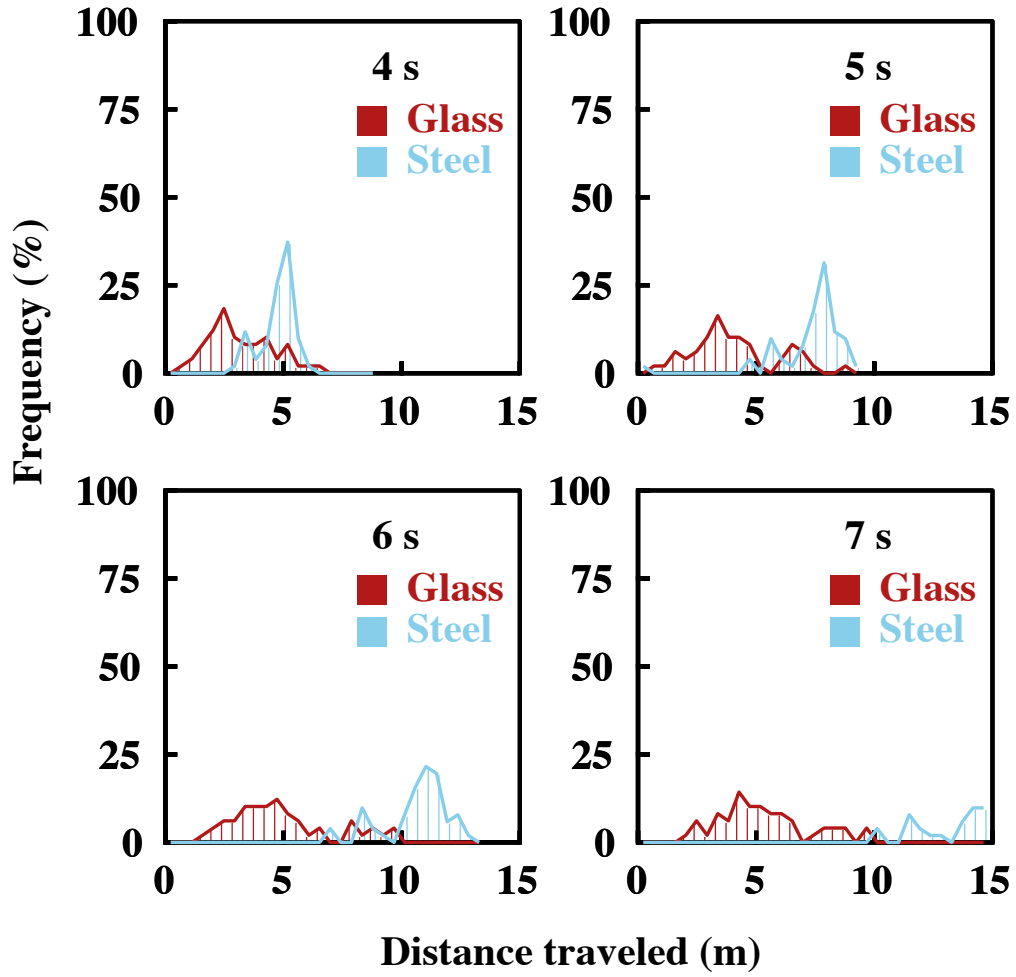


Figure 4.5: Time evolution for the displacement of 100 particles, comprised of a 50-50 number fraction of steel and glass particles in the absence of fluid at Γ_{o_2} .

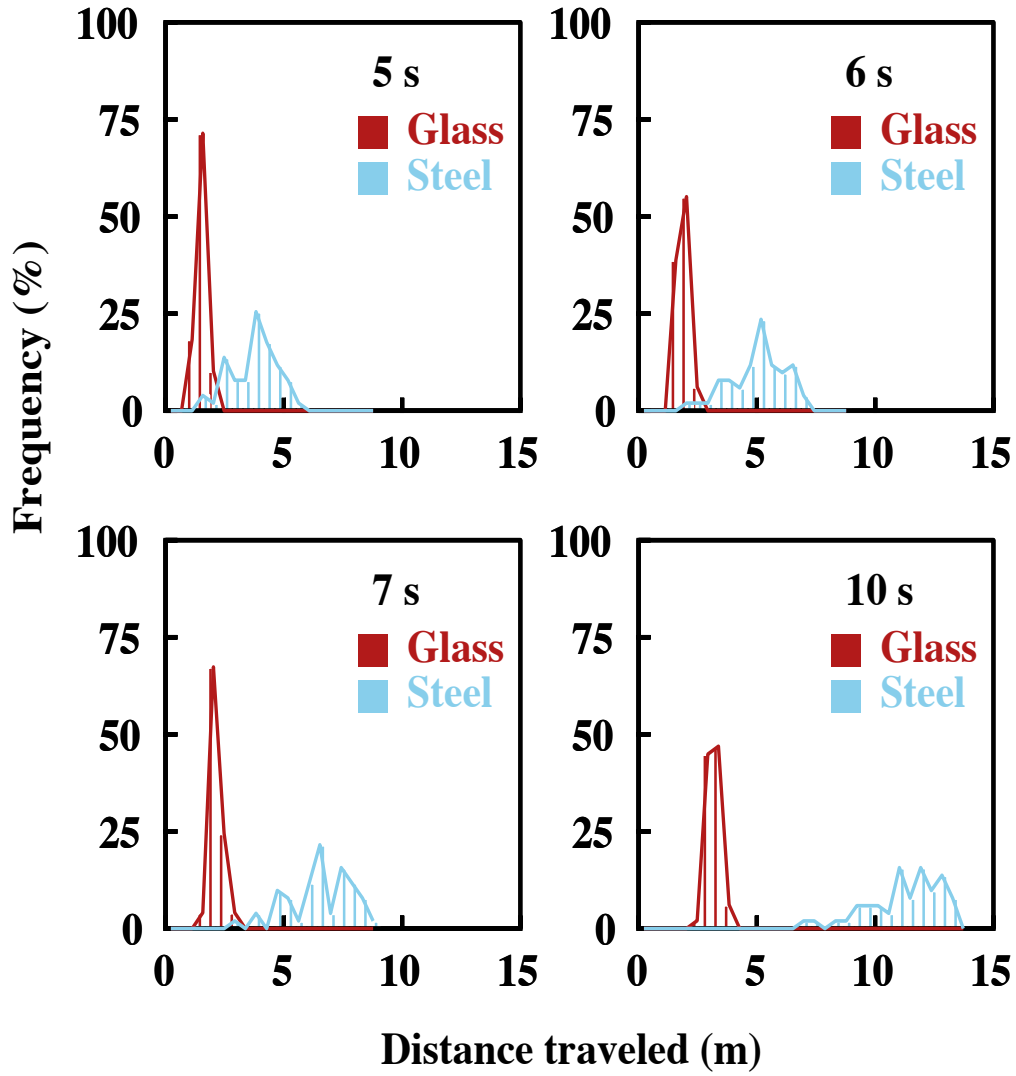


Figure 4.6: Time evolution for the separation of 100 particles, comprised of a 50-50 number fraction of steel and glass particles employing water at Γ_{w2} . The parameters associated for vibration can be found in Table 4.4.

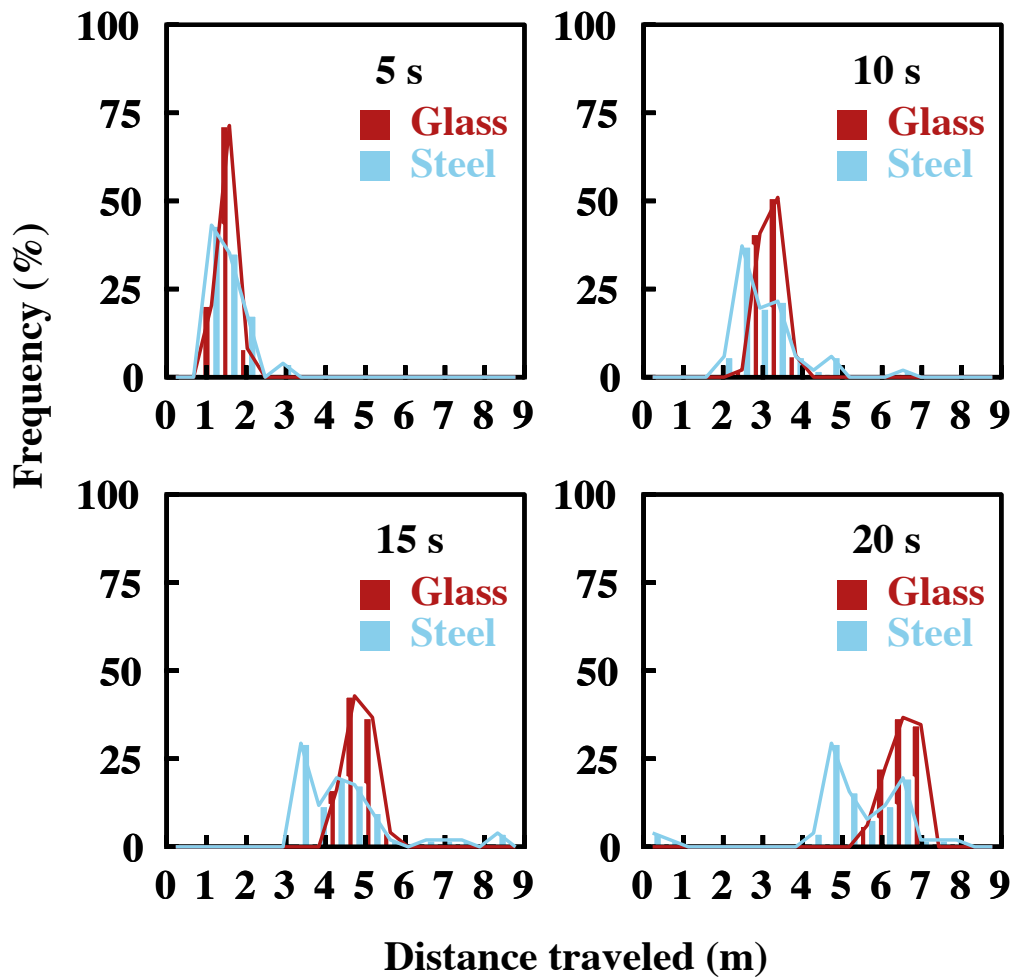


Figure 4.7: Time evolution for the displacement of 100 particles, comprised of a 50-50 number fraction of steel and glass particles in the absence of fluid at Γ_{w2} .

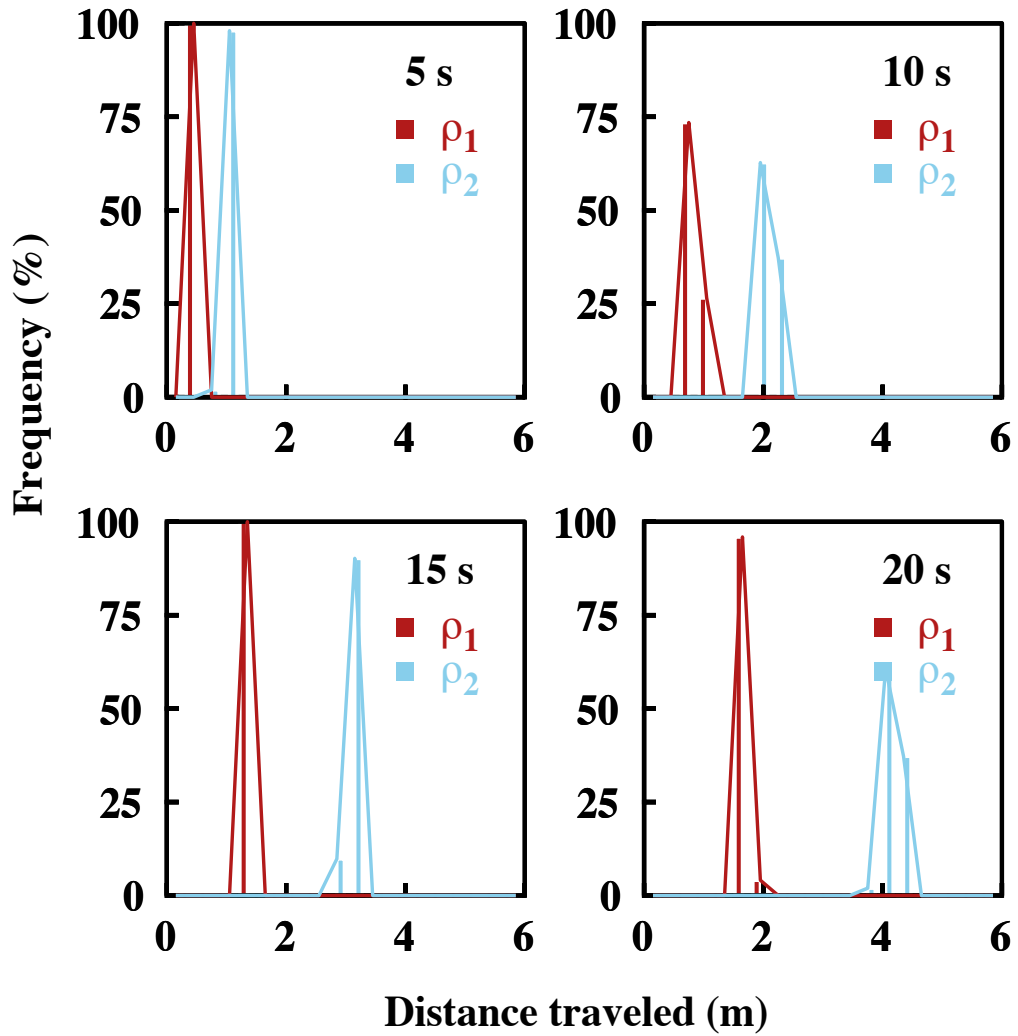


Figure 4.8: Time evolution for the separation of 100 particles of a density disperse mixture of glass using silicone oil at condition Γ_{o2} , where $\rho_1 = 2700kg/m^3$ and $\rho_2 = 8100kg/m^3$.

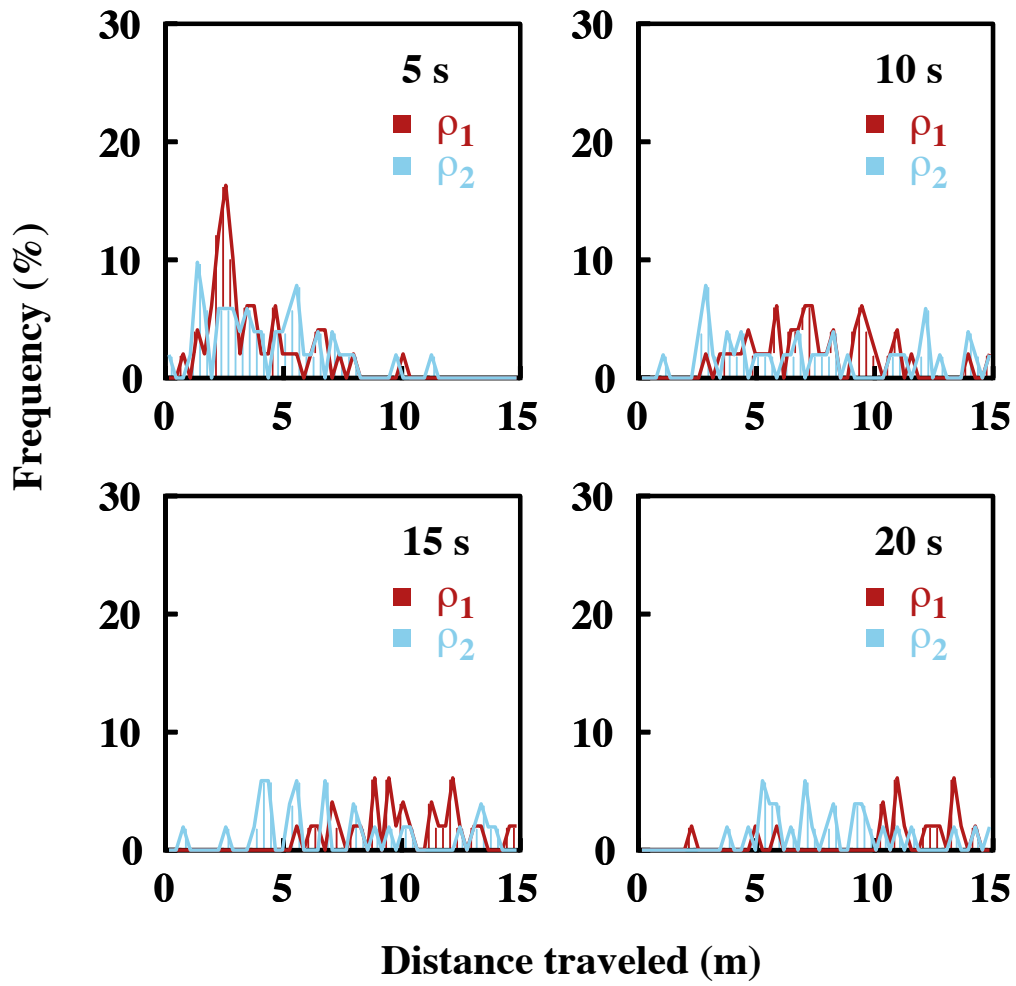


Figure 4.9: Time evolution for the displacement of 100 particle of a density disperse mixture of glass in the absence of fluid at Γ_{o2} , where $\rho_1 = 2700kg/m^3$ and $\rho_2 = 8100kg/m^3$.

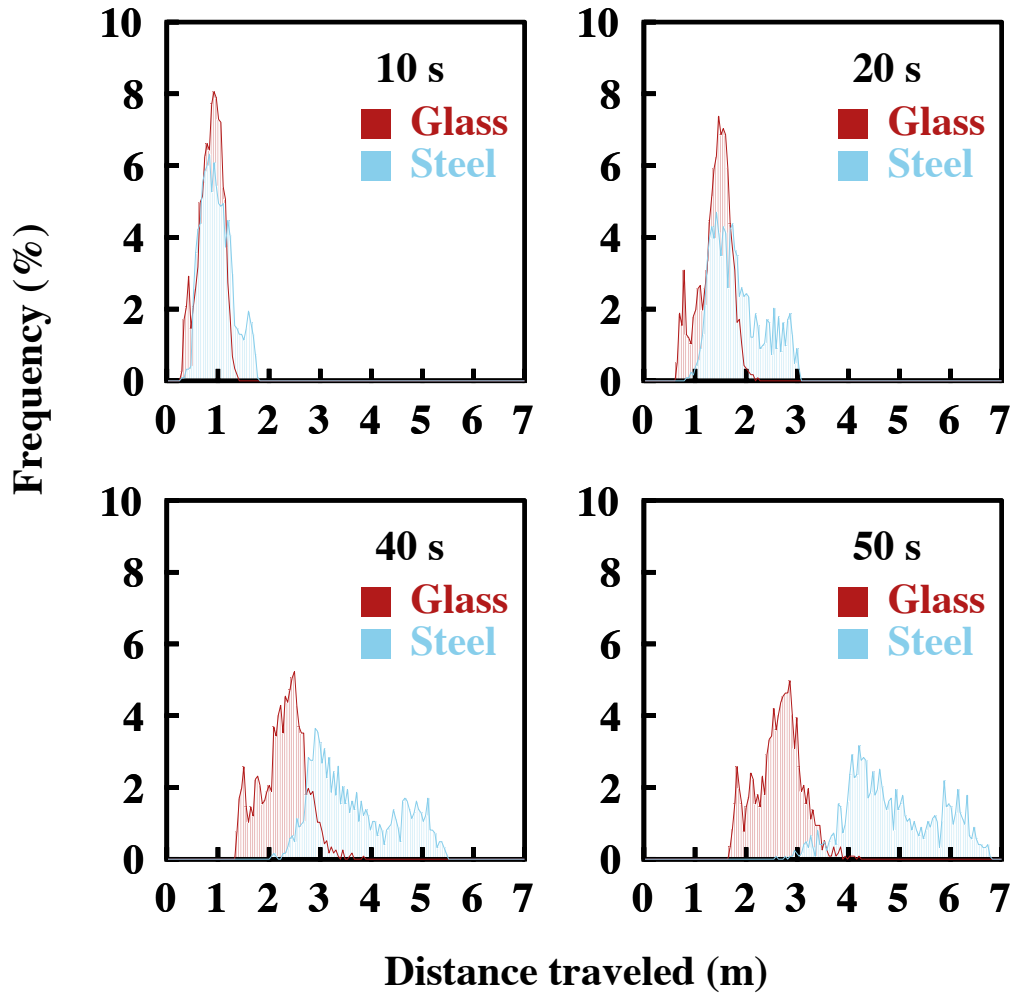


Figure 4.10: Time evolution for the displacement of 2400 particle comprised of a 50-50 number fraction of steel and glass particles employing water at Γ_{w2} . The parameters associated for vibration can be found in Table 4.4.

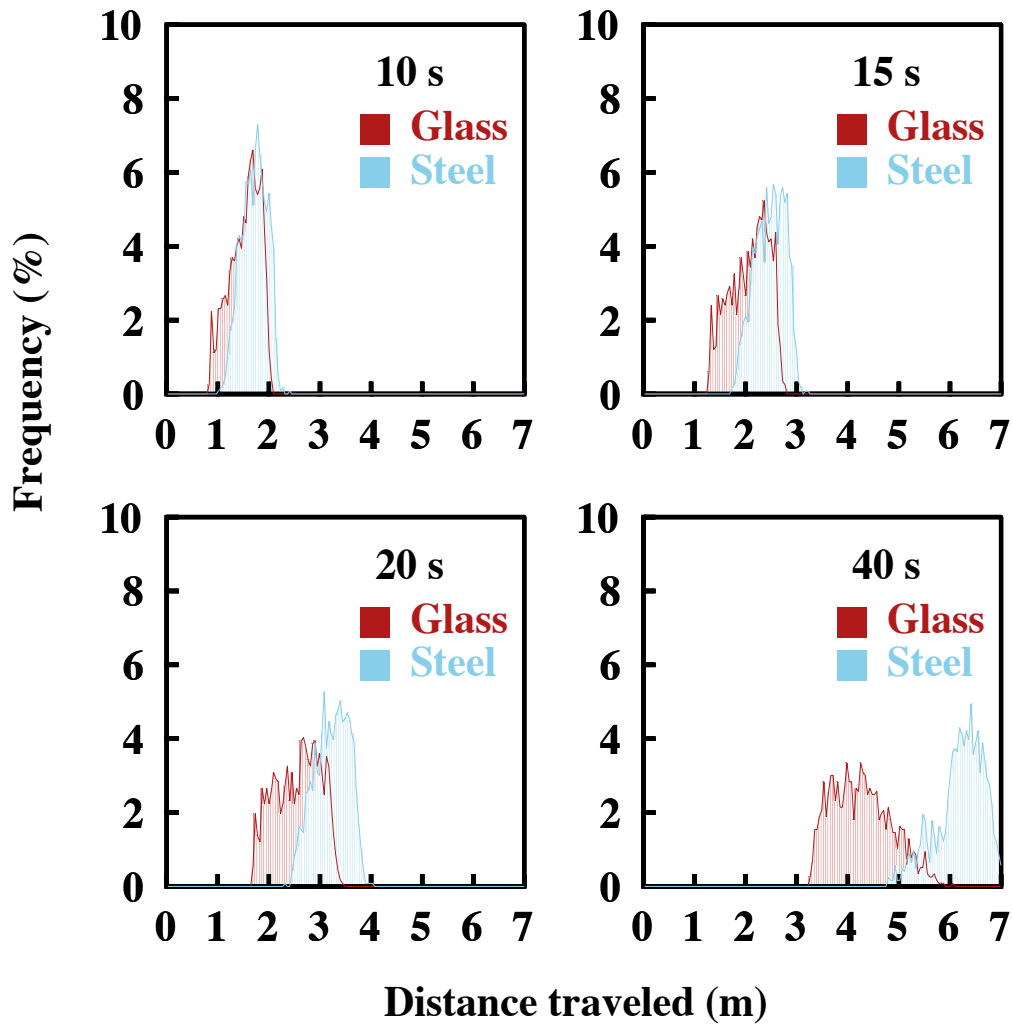


Figure 4.11: Time evolution for the separation of 2400 particles comprised of a 50-50 number fraction of steel and glass particles employing oil at Γ_{o2} . The parameters associated for vibration can be found in Table 4.3.

4.4 SUMMARY

The implementation of PD simulations has provided evidence of the possibility rate-based separation of a mixture by introducing fluid interactions to selectively impede displacement. Given that all properties of particles are known, a device can be designed that implements vibrations to provide a mixture with an energy source such that interactions with the coating fluid inside the duct result in separation.

Single particle simulations are useful to predict the candidate conditions under which separation will occur; however, at present, these trial simulations cannot be used to predict the time it will take for two species to separate. This is true primarily because the role of additional inter-particle interactions (as opposed to particle-surface interactions) changing the behavior of flow in a way that cannot be predicted from the single-particle studies.

While separation using a vibrated bed can be achieved without the need to incorporate a fluid, there are advantages in doing so. Most notably, adding an interstitial fluid causes the particle *mass differences* to become the dominant separation criterion (rather than *COR differences*, as in a dry case). Moreover, when adding a fluid the chute length required to separate a mixture is generally reduced, making it more feasible to operate a vibrated bed to separate granular materials industrially. Also, wet systems present cluster formation, which could facilitate the extraction of pure species. Finally, incorporating a small liquid volume can yield separation under conditions where dry vibration does not, as seen for condition Γ_{w2} .

Identifying different conditions to separate an otherwise identical mixture of glass and steel is indicative of the potential of the dynamic granular chromatograph system. Further studies are necessary to devise a continuous operation unit with industrial applications.

5.0 STUDY OF PENDULAR AND CAPILLARY LIQUID BRIDGES

5.1 INTRODUCTION

Investigating the phenomena involved in solid-liquid interactions is important due to the ubiquitous presence of compound solid-liquid systems among a variety of industries (i.e. pharmaceutical, chemical, cosmetic, and agricultural) and with diverse chemical and physical applications, such as agglomeration, and crystal growth. In these systems strong adhesion can be the result from the liquid meniscus that forms around the point of contact between solid surfaces [106]. This force is called the capillary force. In a two-particle system these menisci bind solid surfaces by creating a bond between two finite contact points. The phenomenon of capillary adhesion is of great importance for granular materials, and powders in the macroscale [107]. While the formation of agglomerates is commonplace in the industrial processing of solid mixtures, axial straining of a liquid bridge, in particular, can be evidenced in the granulation process.

Understanding and modeling multiphase systems is complex due to the different forces acting on the solids depending on the volume of fluid present. Depending on the liquid volume- capillary, surface, and viscous forces can appear and change the mechanical properties of the mixture, such as its tensile strength [108, 109, 110]. The increasingly intricate interactions between the solid and liquid components, as the saturation level increases, has limited most of the available experimental studies to the pendular regime, and analytical models are developed for stable pairwise, axisymmetric bridges. Furthermore, the study of the formation and rupture of binding liquid networks has the added problem of bridge stability, particularly when dealing with bridges linking spherical solids.

To forgo this problem most studies are limited to working with *small* liquid volumes (relative to particle size) such that a stable meniscus can be sustained between the solids [111, 69]. A formal definition of what we consider to be small liquid volumes will be discussed later.

The attraction or repulsion forces between solids and the interstitial liquid are a result of a pressure differential across the interface. The pressure differential can be calculated using the Young-Laplace (YL) equation, if the shape of the meniscus is known [107]. Megias-Algacil & Gauckler [112, 113] recently presented a study for the capillary forces between spheres for liquid volumes forming both concave and convex liquid bridge. The results analyze the nature of the cohesive forces, and present values for contact angle and relative liquid volume, defined as $V_{rel} = V/(\frac{4}{3}\pi R^3)$ for which a concave or convex meniscus can be expected. Urso *et al.* [65, 66] present theoretical two-dimensional studies for the rupture of liquid bridges including the transitional states between pendular and capillary saturation level. They introduce equations to calculate the area of the liquid bridge surface for different saturation states and meniscus geometries. Murase *et al.* [114] presented a first attempt at characterizing the straining phenomena for a liquid bridges of different volumes held between three spheres. They conclude that the maximum tensile force of the liquid bridge is the same for the two and three sphere system for the static rupture mechanism, but two times larger for the three-particle configuration under dynamic rupture conditions.

It is the objective of this study to perform experimental measures for the rupture force of menisci between two- and three-sphere interactions. We will follow the taxonomy described by Urso *et al.* [65, 66], where bridges between two particles are termed pendular, systems where the particle interstices are fully saturated are called capillary, and intermediate saturations where there are varying degrees of interstitial voids are considered to represent funicular saturation; however this work will only measure pendular and capillary rupture forces.

5.1.1 The rupture of a pendular liquid bridge

The rupture force for pendular liquid bridges has been studied for decades [107, 109, 110, 115, 116, 70, 117, 118]. Particle-plane and particle-particle interactions have been modeled for spherical particles and small liquid volumes. In general, the solution to the rupture energy of a liquid bridge can be found by considering it as a two-part problem. First, the stability problem and second, the net attraction/repulsion forces induced by the formation of liquid bridges [109].

When considering a packed bed, the theory for different saturation levels identifies the limit of the pendular regime at $\approx 13\%$ moisture content, while the funicular regime is identified as corresponding to a moisture content above 13% and up to 25% [68]. It is known additionally, that for small enough volumes, where the effect of gravity can be neglected, the mean curvature of the bridge surface between two spheres may be approximated as constant and the contact point is fixed [119]. The maximum volume of fluid, for which the effects of gravity can be considered negligible, is estimated using the following equation:

$$\kappa = \sqrt{\frac{\sigma}{g\rho}}, \quad (5.1)$$

where ρ_l is the density difference between the solid and the liquid phases, and κ is known as the capillary constant, or capillary length (see Figure 2.2).

In order to model such interactions it is necessary to solve the Young-Laplace (YL) equation for capillary forces in the presence of a curved liquid-vapor interface. The pressure differential across the liquid-gas interface, is defined by the shape of the meniscus. It is commonplace to assume the shape of the meniscus is described by a solid of revolution [75]. While numerical solutions for the YL equation for a wide variety of revolution surfaces are known, more often than not, an equation based on a toroidal shape is implemented [69, 74, 76]. Based on this approach, in order to perform an axially oriented force balance, first a system in equilibrium is defined (Figure 2.2). Then, making use of the surfaces of revolution to calculate the pressure differential across the liquid-gas interface according to YL, one employs the theories of capillarity and lubrication to calculate the total cohesive force [120, 121].

The work discussed herein follows the procedure described by Pitois *et al.* for the rupture energy of a pendular liquid bridge [120]. The simplified dimensionless expression derived for the capillary force contribution takes the form

$$F_{cap}^* = \frac{F_{cap}}{\sigma R} = 2\pi \cos \phi \zeta_v, \quad (5.2)$$

with,

$$\zeta_v = 1 - \left(1 + \frac{(2V^*)}{(\pi D^2)} \right)^{\frac{-1}{2}}, \quad (5.3)$$

where D is the distance between the two solid surfaces, σ is the fluid surface tension, and θ is the solid-liquid wetting angle. The star symbol (*) denotes the dimensionless form of an expression. The length scale to write dimensionless parameters is the radius of the sphere R , such that $V^* = V/R^3$, $D^* = D/R$. Similarly, we use as the force scale σR (see Eq. 5.2).

5.1.2 Viscous Forces

An expression for the viscous force contributions to granular systems was developed by Ennis *et al.* based on a derivation of the Reynolds equation to describe thin film behavior [69]. The function revealed how the contribution of lubrication forces to the total rupture force becomes increasingly important for high viscosity fluids. While the objective of the current work is focused on low viscosity fluids only, we have implemented the viscous contribution as part of the computational model for completion. The viscous contribution, in its dimensionless form, can be written as:

$$F_{visc}^* = \frac{3}{2}\pi \frac{C_a}{D^*} \zeta_v^2, \quad (5.4)$$

where, Ca is the capillary number defined as $Ca = \mu\sigma/a$, and μ is the viscosity of the fluid. It follows that the total force is the sum of the capillary and viscous terms.

A relationship between the liquid bridge volume, the liquid-solid contact angle and the quasi-static rupture distance, was presented by Lian *et al.* [74] for liquid volumes where the effect of gravity can be neglected. The rupture distance is modeled by (2.19).

The total cohesive contribution can then be expressed as the sum of the total capillary and viscous component:

$$F_{tot}^* = 2\pi \cos \phi \zeta_v + \frac{3}{2}\pi \frac{C_a}{D^*} \zeta_v^2 \quad (5.5)$$

Key contributors to viscous forces, such as wetting angles, and stability on curved surfaces have become areas of independent studies [122, 123, 124]. Results indicated that minimal shifts in the shape of the meniscus had a significant impact on the evolution and rupture of the bridge. The present work will be concerned with steady state, non-thermodynamic equilibrium, and will assume the bridge maintains a constant mean-curvature.

Adams *et al.* [125] present a study on mapping the influence of gravitational forces for the liquid binding of solid spheres. The Bond number (Bo)- defined as $Bo = \Delta\rho g d^2 / \sigma$ where d is the characteristic length - is used to quantify the gravitational distortion for a free liquid droplet. It serves as a characterization parameter when a scaling factor – which is a function of the liquid bridge volume (V) – is introduced. The modified Bond number is defined as V^*Bo and was used in Ref [125] to predict the influence of gravitational forces. In this work Adams *et al.* identified systems that have $V^*Bo < 0.01$ as being essentially gravity free, while systems in the range $0.01 < V^*Bo < 0.015$ are deemed transitional and those with $V^*Bo > 0.015$ are the considered to be gravity controlled systems (that is, they are systems in which the gravity component plays a significant role in the draining mechanism and subsequent bridge rupture).

For axisymmetric pendular rings between a sphere with radius R and a flat surface, the Bond number is expressed as $Bo = \Delta\rho g R^2 / \sigma$ where the characteristic length is the particle radius. For while for a liquid bridge between identical spheres, on the other hand, the Bond number can be expressed in terms of the liquid volume (V), as:

$$Bo = \Delta\rho g V / R\sigma. \quad (5.6)$$

When the largest dimension of a sessile drop exceeds κ the gravitational effects become significant, and the straining of a liquid bridge (between two spheres) produces a decrease in the liquid filling angle (β) of the top sphere as separation increases (see Fig. 2.2) until eventually the bridge becomes unstable.

For cases where there is an expected gravitational influence on the deformation of the liquid bridge Adams *et al.* suggests a modified rupture criterion, function of the proposed modified Bond number.

$$D_{rupt}^* \simeq (1 - 0.48V^*Bo)V^{*1/3}. \quad (5.7)$$

The experimentally measured rupture distances are used to assess the accuracy of the different rupture criterion.

5.2 MATERIALS & METHODS

Rupture tests were performed using acrylic beads of 2 mm in diameter. Ethylene-glycol (EG) was selected as the fluid to minimize evaporation at ambient conditions (refer to Table 5.1 for relevant fluid properties). Different fluid volumes were tested in order to describe the relationship between liquid volume and rupture behavior in the pendular and capillary regimes.

Table 5.1: Properties for Ethylene Glycol at 20°C

Property	Value	units
Molar mass	62.07	g/mol
Density	1.11	g/cm ³
Viscosity	0.015	Pa s
Surface Tension	0.048	N/m

5.2.1 Measurement of micromechanical forces in an axially strained liquid bridge

To measure the rupture forces of liquid binding networks, a micro-mechanical force microscope was constructed, which consists of a (Philtec) fiberoptic sensor, a stainless-steel cantilever and a moving stage. Data is collected and interpreted using two essential components: (1) a multi-purpose texture analyzer (Brookfield Engineering), and (2) a DMS optical displacement sensor. The two devices are coupled via a stainless-steel cantilever (thickness = 0.007 inches). The fiberoptic sensor can be programmed to translate the reflectivity measurement to a distance and is calibrated in-situ. The reflectivity itself is a function of the cantilever properties as well as the finished surface.

The texture analyzer (TA) holds the stage for the static bottom particle(s), as well as the retractable shaft, which is fitted with a custom stainless-steel cantilever. A retracting particle- identical to the stationary one is fixed underneath, at the distal end of the cantilever. This sphere cantilever unit is the sole mobile element in this setup, which simultaneously imparts axial strain on liquid bridges and measuring the forces acting on the system. Directly above and parallel to the cantilever is an arm which holds the optical displacement sensor. As the shaft is raised, liquid forces operating on the retracting sphere bend the cantilever from its resting position. As the distance between the cantilever and the optical sensor changes, the reflectivity of the cantilever beam is altered and this change is calibrated to yield a strain (length). Based on the measured bending modulus of the cantilever, this strain is converted to a force. The choice of cantilever thickness is determined via trial-and-error in which different thicknesses impact the accuracy of force measurement (due primarily to a changing signal-to-noise ratio). In practice, we base our selection of cantilever on a calibration of the strain to force conversion over the entire range of interest.

The optical sensor is responsible for quantifying the cantilever displacement in response to the capillary forces. The sensor emits a laser signal that reflects off of the cantilever surface, at an angle (θ_{ref}), which changes the measured reflectivity. The relationship between reflectivity (a function of θ_{ref}), and the distance between the sensor tip to the cantilever surface, is known. The style finish of this surface, the roughness and metal properties will determine the amount of light that is reflected back to the sensor. Generally the further the

optical sensor is from the cantilever surface, the more diffuse the light rays reflected will be. Therefore, the reflectivity reading decreases as the distance between sensor and cantilever increases. Initial calibration requires data from the reflectance-distance curve for the specific sensor and cantilever. Once the calibration is set, the position of the optical sensor must remain constant, for this is the point of reference.

The retraction velocity employed must ensure slow displacement of the cantilever such that the rupture is considered quasi-static. The TA device allows setting the shaft displacement at $10\mu m/s$, a velocity slow enough to capture the static rupture as indicated in Fig. 5.3. The optical sensor software keeps a real-time record of the reflectivity as well as the distance between the sensor tip and the cantilever surface. Having a set, constant shaft-speed allows for the straightforward calculation of the distance displaced in time. A qualitative analysis of the primary experimental measurements is performed in order to validate that the shaft operating velocity used in this work is slow enough to approximate quasi-static operation. The rupture of a liquid bridge under dynamic conditions is beyond the scope of the current work.

Making use of Eqs. 5.1 and 2.19, inserting the corresponding values for gravity and EG properties (i.e. density, surface tension, see Table 5.1), we calculate the rupture distance and relate it to the particle volume proposed by Lian *et al.* [74]. A gravity free liquid bridge corresponds to effective volumes where $V^{*1/3} < \kappa$, following the rationale presented in Equation 5.1 [106]. Therefore, for the particles used in this study the maximum volume allowable in order to correctly neglect gravitational forces is $\approx 0.5\mu L$. This calculated volume highlights the importance of operating with small particles. Operating with liquid volumes above $0.5\mu L$ could give rise to non-negligible gravitational forces [74].



Figure 5.1: Micromechanical force microscope: Brookfield texture analyzer casing, stainless-steel retractible cantilever, optical displacement sensor.

5.2.2 Experimental methodology

Each run is initiated in the same manner; a drop of volume V is carefully dispensed with a syringe on top of the bottom sphere(s), which remain static. The cantilever sphere is then slowly brought into contact with the liquid drop, then displacing the liquid to the surrounding until making contact with the static bead, or each of two adjacent beads when investigating three-particle interactions. The instant the top bead starts retracting by action of the shaft, the fluid will make its way into the newly available gap and produce the peak force reading in the force distance diagram. In the case of three-particle interactions, drops of EG- comprised of varying volumes- are applied to the top surfaces of each static bead, such that when the cantilever sphere is lowered, a liquid bridge conjoins all particles. As before, prior to the start of each trial, the top and bottom beads are positioned in direct contact. The data is herein presented in dimensionless terms, unless stated otherwise. Terms will be made dimensionless by using the particle radius, and surface tension of the fluid, ethylene glycol (EG).

5.3 RESULTS AND ANALYSIS

In the interest of verifying the accuracy of the measurements recorded by the micro-mechanical force microscope initial tests were aimed at validating the experimental methodology. Accordingly, the rupture force for a single pendular liquid bridge was measured for a sphere-plane configuration. Fig. 5.3 presents the tensile strength behavior between a glass plate and a sphere, measured experimentally and compared to the corresponding theoretical solution as a function of the separation between particles D . For all force curves presented herein, the last point plotted represents the maximum separation achieved before rupture occurred.

The theoretical curves shown in Fig. 5.3 were plotted following the analysis presented by Pitois *et al.* which calculates the adhesive force for a constant liquid bridge volume with

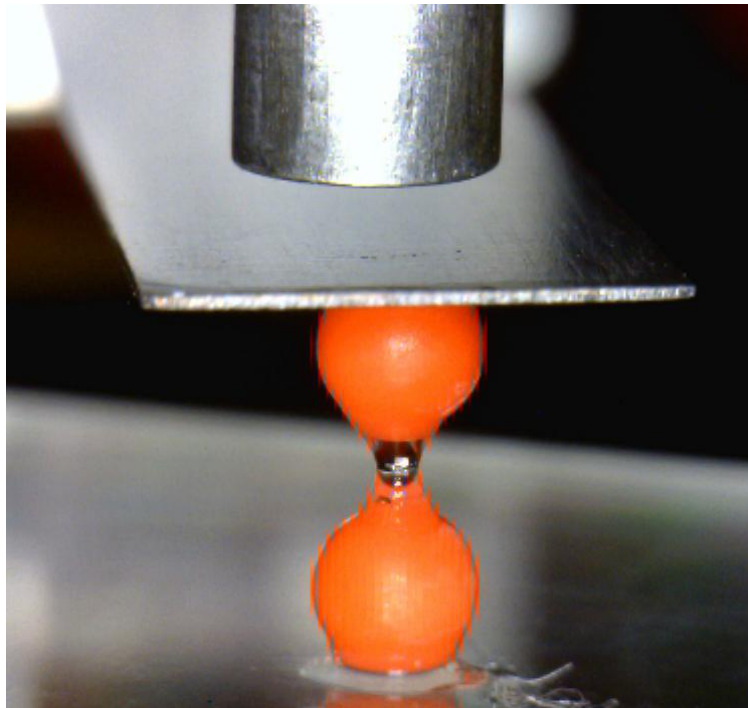


Figure 5.2: Image of a pendular liquid bridge between two spheres. The top sphere is attached to the cantilever and the bottom sphere is held static. Straining of the liquid bridge is a result of the upwards movement of the top sphere at constant speed

pinned contact points (refer to Equations 5.2 and 5.4 [121]). The fluid properties of EG were used in the theoretical calculations. The total force data appears to lie on the same curve as the capillary force equation (Fig. 3), which supports that capillary, not viscous, forces dominate in this system. Throughout the range of particle separation the measured data falls within two standard deviations (based on five independent trials) from the theoretical curve. The agreement observed between the measured and theoretical curves lends validity to the experimental setup.

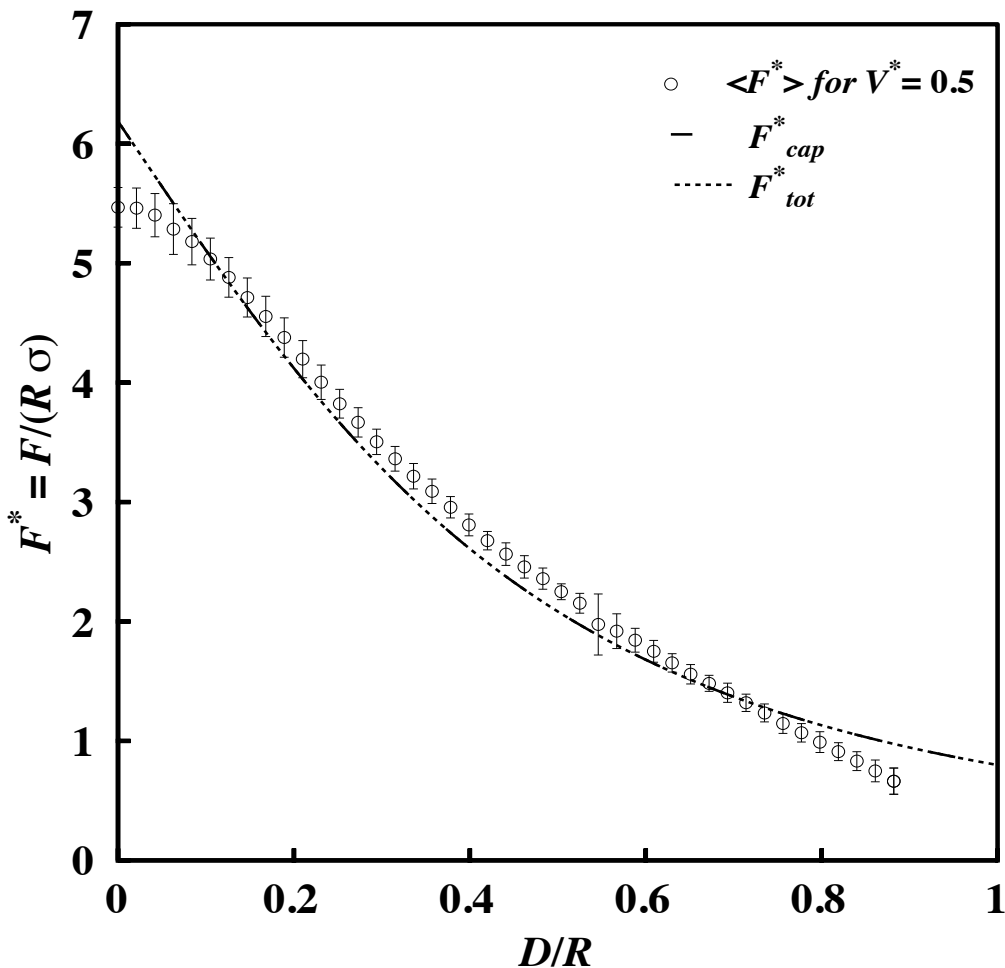


Figure 5.3: Force between an acrylic sphere and glass plane forming a pendar liquid bridge measured experimentally compared with the calculated theoretical values for F^*_{cap} (Eq. 5.2), and F^*_{tot} (Eq. 5.5) as described by Pitois *et al.* The fluid used is Ethylene glycol.

In addition to this, for the widely studied plate and sphere system the rupture distance obtained experimentally follows the relation predicted by Lian *et al.* [74], Eq. 2.19. The selection of EG as the fluid has the advantage of displaying contact angles close to zero, therefore assuming $\theta = 0$ for all systems the above expression reduces to:

$$\tilde{D}_{rupt} \approx V^{*1/3}, \quad (5.8)$$

indicating a direct correlation between the liquid bridge volume and the dimensionless rupture distance. Eq. 5.8 underestimates the rupture distance observed in Fig. 5.3 by 11%.

5.3.1 Liquid bridges between two particles

Calculated modified Bo number indicates that only for dimensionless volumes above one (1) will gravity effects be expected to affect the draining mechanism. According to the V^*Bo calculated, presented in Table 5.2, for liquid volumes where $0.5 \geq V^* \geq 0.75$ are in the transitional regime, where there is a significant decrease in the rupture distance and change in the force by half the bridge weight. For volumes where $V^* \geq 0.75$ that fall inside the gravity controlled regime, rupture by a draining mechanism. The expected rupture distances are also presented, calculated with Eq. 5.8 or 5.7 according to the expected gravitational regime.

Table 5.2: Modified Bond number and expected rupture distance calculations for liquid volumes dispensed

Target V^*	V^*Bo	$V^{*1/3}$	D_{rup}^* (gravitational mapping)
0.25	0.057	0.63	0.63
0.50	0.11	0.79	0.75
0.75	0.17	0.90	0.83
1.0	0.23	1.0	0.89
2.0	0.45	1.3	0.98

According to the modified rupture distance approximation proposed by Adams *et al.* the gravitational effects reduce the rupture distance as much as 20% for the larger liquid volumes dispensed.

In order to observe the sensitivity of the measurements the results for three characteristic runs are plotted for each (liquid volume) condition. The two-particle bridge rupture results presented in Fig. 5.4 are further supported by other indicators reported in literature. Most notably, the maximum force is about half of the sphere-plane rupture force [106], for the same liquid volume.

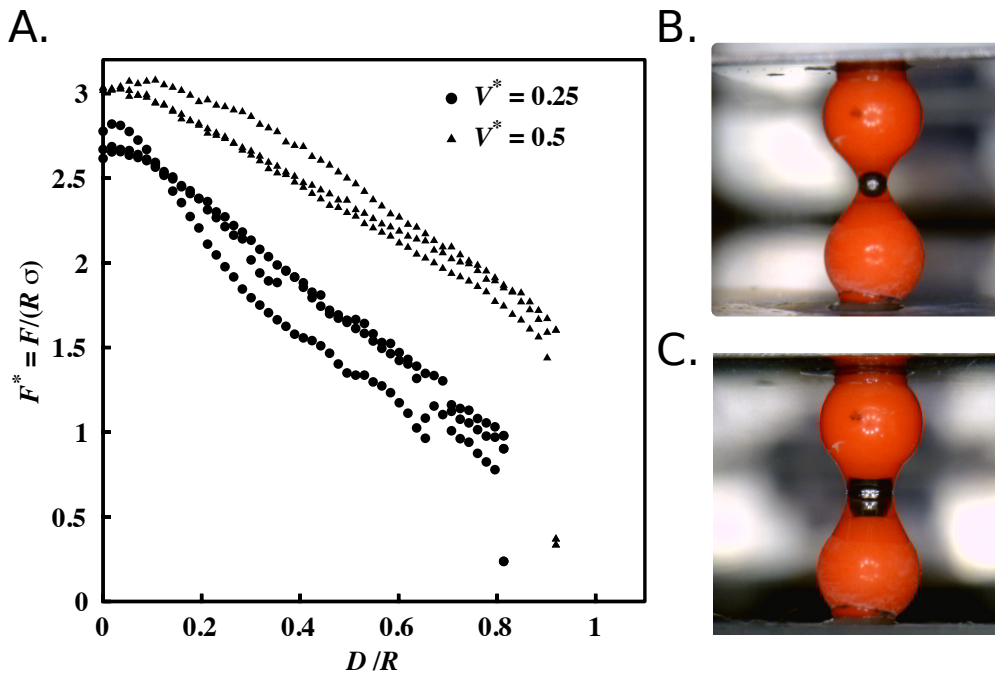


Figure 5.4: A) Experimentally measured capillary force versus separation curves for an axially strained pendular liquid bridge formed between two identical acrylic spheres ($R = 1mm$). Three runs for each corresponding liquid volume ($V^* = 0.25$, $V^* = 0.50$) of ethylene-glycol are presented. B) Picture liquid bridge of volume $V^* = 0.25$. C) Picture liquid bridge of volume $V^* = 0.50$.

The measured tensile force of the liquid bridge is in accordance with theoretical values presented by Willett *et al.* [117] where the maximum capillary force is considered insensitive to the liquid volume for pendular bridges, without gravity effects. In addition to this, Willett *et al.* reported rupture distances being overestimated by Eq. 2.19, and suggested an alternate best-fit solution of the form:

$$D_{rupt}^* = \left(1 + \frac{\phi}{2}\right) \left(V^{*1/3} + \frac{V^{*2/3}}{10}\right) \quad (5.9)$$

Results presented in Fig. 5.4 also support this observation, as the expected rupture distances are underestimated by Eq. 5.8 and 5.7, whereas the modified expression presented by Willett *et al.* describes accurately the results presented for two particles.

5.3.2 Three particle system and capillary liquid bridges

When testing a three-particle set-up two different configurations were tried: one simulating a high solid fraction, where particles are closer together, compared to a low solid fraction, in order to observe the difference in rupture behavior. A setup with a center-to-center distance between the two bottom spheres of $d^* = d/R = 2.5$ was chosen, as the high solid fraction condition, to test a triple contact starting point. The initial condition for the force measurement is when the drop is in contact with all three spheres. The results for three different *effective* liquid volumes are presented in Fig. 5.5.

Contrary to the experimental results presented in Murase *et al.* [114] the observed trend for the force of a single liquid bridge in contact with three spheres (Fig.5.5) does not result in the same maximum capillary force as it does for two spheres (Fig. 5.4). In fact, the maximum measured force is higher when the liquid bridge is stretched over three particles, where we obtain a value comparable with the maximum force for a liquid bridge between a sphere and a plane. This can be explained by the fact that the liquid volume distributes among the two bottom spheres creating a meniscus with a shape closer to that formed between a sphere and a plane.

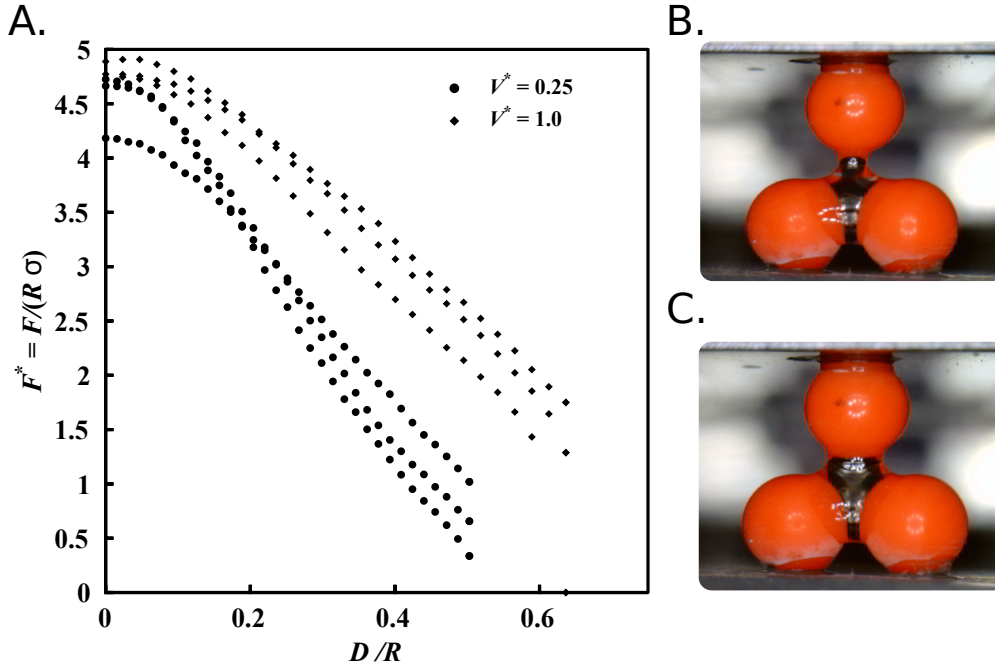


Figure 5.5: A) Measured liquid bridge force for a single axially strained bridge in contact with three identical acrylic spheres. Three runs are plotted for each of the liquid volumes used ($V^* = 0.25$, $V^* = 1.0$). The center-to-center distance for the bottom spheres is $d^* = 2.5$. B) Picture liquid bridge $V^* = 0.25$. C) Picture liquid bridge $V^* = 1.0$.

The rupture distance, on the other hand, is reduced by about 20% for the gravity-free volume of $V^* = 0.25$, and is roughly half the expected length for the capillary saturation volume of $V^* = 1.0$, indicating that rupture distance approximations are only applicable for pendular liquid bridges.

We should note that, for capillary saturation volumes, imprecise draining mechanisms were observed for some of the runs. During these runs the liquid meniscus shifts forming a two-particle bridge between the cantilever sphere and only one of the static beads. In the most frequently seen draining mechanism, a single bridge forms as it does between two spheres, yet the neck of the meniscus forms closer to the top sphere allowing the majority of the volume to be balanced between the bottom two (see Fig 5.6).

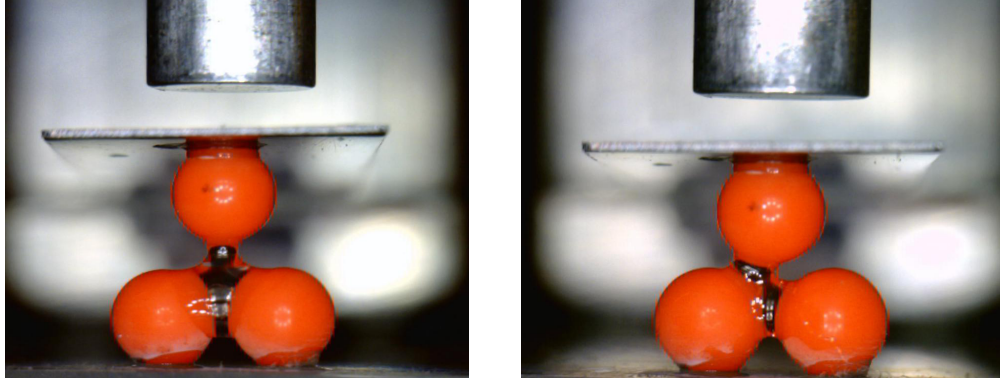


Figure 5.6: Comparison of the two primary draining behavior observed for a single bridge between three identical spheres. Left: Axially strained single bridge where the neck of the meniscus is located closer to the top sphere. Right: Asymmetrical draining and rupture of the meniscus.

The second configuration tested was that mimicking a low solid fraction particle bed, meaning there is a greater gap between adjacent spheres. Again, two drops are dispensed – one above each of the bottom spheres – which now lay at a measured center-to-center distance of $d^* = 3.2$, Fig 5.7.B and 5.7.C. The cantilever is lowered until the top sphere makes contact with the two bottom spheres without allowing the two drops to coalesce. For these cases the liquid volume reported corresponds to the liquid volume *per bridge*, meaning the total liquid volume of the system is twice as much.

The maximum force for two liquid bridges held in a three-particle configuration presents two noteworthy characteristics. First, the maximum force is larger than that of a single liquid bridge held between two spheres. A way to understand this is to think of two springs in parallel. Two identical springs in parallel exert a force that is effectively twice the force of a single bridge, Fig. 5.8A. However, when these springs are inclined at an angle (θ) the force is reduced by a factor of $\sin \theta$, as in Fig. 5.8B.

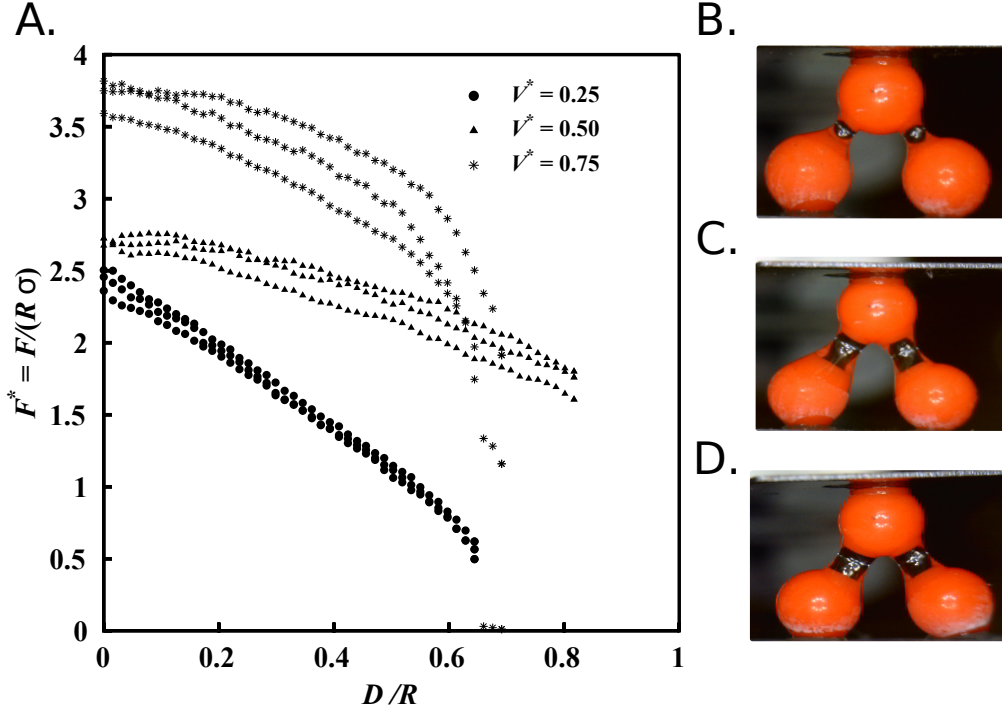


Figure 5.7: A) Measured Capillary force between for two axially strained liquid bridges formed between three identical spheres. Two separate drops are initially placed on top of each of the bottom spheres. Three runs are plotted for each of the liquid volumes used ($V^* = 0.25$, $V^* = 0.50$, and $V^* = 0.75$). The center-to-center separation between the bottom particles is $d^* = 3.2$. B) Picture liquid bridge $V^* = 0.25$. C) Picture liquid bridge $V^* = 0.50$. D) Picture liquid bridge $V^* = 0.75$.

The maximum force for two liquid bridges held in a three-particle configuration presents two noteworthy characteristics. First, the maximum force is larger than that of a single liquid bridge held between two spheres. A way to understand this is to think of two springs in parallel. Two identical springs in parallel exert a force that is effectively twice the force of a single bridge, Fig. 5.8A; however, when these springs are inclined at an angle (θ) the force is reduced by a factor of $\sin \theta$, as in Fig. 5.8B.

For the configuration used in our experimental trials the angle is approximately $\theta = 50^\circ$ which would correctly account for the increase in maximum bridge force observed for $V^* = 0.75$, but overestimated the expected increase in force for the lower volumes. Second, the maximum force increases with increased liquid volume even for liquid volumes corresponding to pendular saturation, and in the transitional gravitational regime.

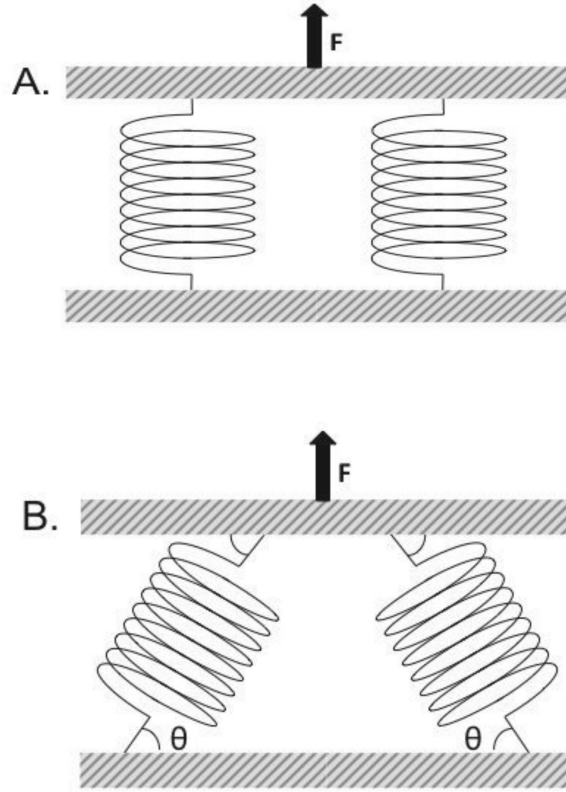


Figure 5.8: Parallel between the combined effect of two springs in parallel and two liquid bridges held between a three particle unit. A) Shows two springs stretched normal to the surface B) Two springs stretched at an angle θ with respect to the surface.

The rupture distance for this case is similar to that of the two-particle configuration, and is approximated to a good degree by Eq. 5.9 for $V^* = 0.25$ and $V^* = 0.5$. For $V^* = 0.75$ the rupture distance is better predicted by the modified rupture proposed by Adams *et al.*, indicating the latent effect of gravitational forces for this volume.

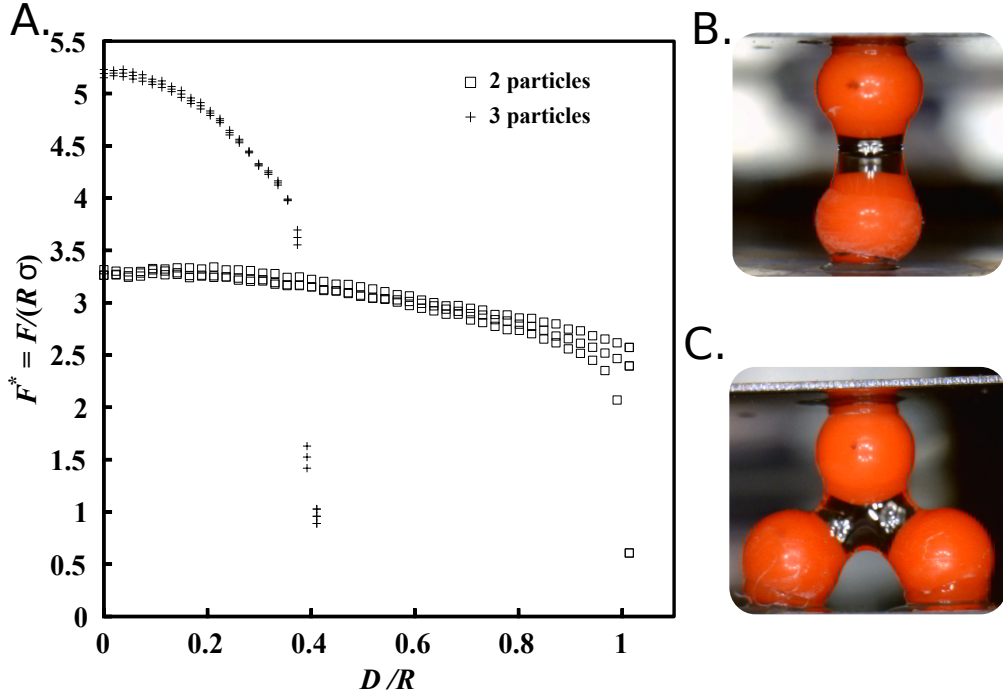


Figure 5.9: A) Rupture force for a dispensed liquid volume $V^* = 2.0$ in a 2 sphere and 3 sphere setup. The three-particle configuration here corresponds to the low solid fraction with $d^* = 3.2$. Three runs are plotted for the two and three particle configuration. B) Picture of liquid bridge ($V^* = 2.0$) held between two particles. C) Picture of liquid bridge ($V^* = 2.0$) held between three particles.

Finally in Figure 5.9 we compare the rupture force for a dispensed volume of $V^* = 2.0$ distributed among two or three particles. Interestingly, for these large liquid volumes we still don't perceive a significant reduction of the maximum capillary force due to gravitational effects. They do, however, exhibit a reduction in the rupture distance that is more significant for the three-particle system than it is for the two-particle configuration. In addition to this, the maximum force is comparable between the close-packed three-particle and the plate-sphere configuration. This can be explained by observing the meniscus shape for both systems, where a single drop in contact with three spheres creates a meniscus geometry that more closely resembles that formed between a sphere and plate.

From a qualitative standpoint, our results are also in agreement with Urso *et al.* [66] in that a pendular configuration will allow for a larger rupture distance than the corresponding capillary configuration, while the latter has a larger maximum binding force.

5.4 SUMMARY AND CONCLUSIONS

In the present study, we measured the quasi-static rupture force of pendular and capillary liquid bridges by using a micro-mechanical force microscope comprised of a Brookfield TA and a fiber optic sensor. The maximum tensile energy of capillary liquid bridges varies with drop volume, contact angle and bridging/draining mechanism. The effect of gravitational forces are conjectured to start influencing the rupture mechanism for $V^* \geq 0.5$.

Capillary liquid bridges are capable of forming strong binding networks given a close packed granular system. The observed trends in F^* also suggest that closely packed granular systems could display a higher cohesion effect than what would be expected based on two-particle system theory. While this effect needs to be studied further it is our hypothesis that this is the result of the meniscus geometry. For closely packed granules, the base spheres could approximate the effect of a bottom flat surface resulting in a net increase in the maximum force.

To completely understand the capillary rupture it would be necessary to test a greater number of initial conditions and describe each one of the observed draining mechanisms, for both close and loosely packed granular materials.

6.0 OUTLOOK AND CONCLUSIONS

The industrial importance of granular material processing is undeniable. Mixtures comprised of macroscopic solids are part of the manufacture of common household items, foods and pharmaceuticals. However ubiquitous these materials are to every day life there are still more questions than answers when it comes to describing the bulk behavior of granular matter. Historically, the design of manufacturing units to process solids has been a trial and error effort. Heuristics and in-situ observations remain a primary source of knowledge when defining geometrical configurations and operational parameters for such units. This has resulted in less than efficient technologies that increase the cost of production. This chapter summarizes the main contributions for each of the studies presented and outlines some potential future work in each area.

The implementation of PD has been successful at reproducing the observed behaviors of free flowing particle, and for cohesive systems when incorporating corresponding equations from theory of capillarity and lubrication. Computational simulations are a useful tool to predict the conditions necessary to control the particle distribution of a process, given all properties of the system are known.

Simple single-particle simulations, implemented for both dynamic and passive separation methods, have been shown to be a useful tool in predicting successful separation conditions. It is worth noting that the presence of a larger number of particles does have a significant influence on the overall flow behavior, and could - in cases where the solid fraction is high - produce a completely different outcome than that observed for low solid fraction. The geometrical configuration of the system will determine an optimal solid fraction.

6.1 THE GALTON BOARD

In Ch. 3 we suggest a passive granular separation method, analogous to sieving in that the separation is the effect of the impeded motion for “larger” particles by an array of obstacles. Unlike sieving however, this method does not yield accumulation of material or clogging resulting in a much more environmentally friendly solution. The Galton board presented here is a quasi two-dimensional system comprised of a flat surface covered in an array of evenly distributed pegs. As a mixture traverses the board collisions with the pegs induce a kinetic differential between the different species involved yielding separation.

In this work we provide preliminary experimental evidence of the separation of a mixture having 1:1 ratio of small to large particles. We compared this with computational results, finding good agreement within the two. Having experimentally tested the possibility of separation using a Galton board the implementation of particle dynamics simulations can provide a shortcut to an optimal design by easily changing the value of operational parameters and studying the outcome effect. The separation between pegs was identified as the key parameter of the system, while elastic properties, and particle size are the characteristic properties for the mixture. The effective separation of a size disperse mixture under purely gravity driven flow and that requires no input energy is a novel contribution and should serve as a starting point in the development of static granular separation units.

Results presented in Ch. 3 relate to a binary size disperse mixture; however a granular mixture having different elastic properties could potentially be separated in the same manner. Computational simulations could be used to easily define a mixture where differences in elastic properties between the species would yield a different terminal velocity. Further optimization to this separation method can evaluate the possibility of designing a continuous operation unit that not only separates the mixture into its constituents spatially within the board but collects them independently.

6.2 THE GRANULAR CHROMATOGRAPH

The study presented in Ch. 4 implements the particle dynamics algorithm coupled with equations of capillarity and lubrication theory to demonstrate the feasible separation of a density disperse mixture. The system is analogous to gas chromatography where an the gas mixture interacts with the walls of the column, coated with an adsorbent. These interactions cause the components of the mixture to elute at a different time, effectively separating the mixture into its constituents. In the case of the granular chromatograph presented, the walls of the column are coated with a fluid and the interactions of the granular species with the walls results in the formation of liquid bridges that restrain motion and induce a kinetic differential. This results in different residence times for different species effectively separating the components of the mixture. This is the first time that a device that combines the effect of vibrational forces and liquid bridge formation to separate a granular mixture.

Studies focused on the segregation effect induced by vibrational forces had focused primarily on the dry case. In this work we not only show it is possible to achieve separation in a wet vibrated column, we present the advantages of including a fluid in conditions were dry vibration would also result in separation. Namely, the presence of a fluid reduces the column length necessary to separate two species. Additionally, the formation purified cluster formation can facilitate the extraction of pure species.

6.3 PENDULAR AND FUNICULAR LIQUID BRIDGES

In Ch. 5 we present the experimental measurement of the rupture of liquid bridges in different saturation levels, for two and three particle configuration. This is the first time that the static rupture of a liquid bridge in the funicular regime is reported, and the first time the effect of distance between spheres (in a three particle configuration) is assessed.

The work performed in order to measure the rupture forces of pendular liquid bridges, presented in this chapter begins to elucidate the effect of adhesive forces resulting from capillary interactions outside of the pendular regime. It is evident from the measurements

presently reported that the effective cohesive liquid force is a complex function of fluid volume, solid fraction and the energetic state of the system under consideration (i.e. dynamic or static). Systems in the same kinetic state, containing identical liquid volumes can build and drain liquid binding networks differently depending on the solid fraction of the granular composite. This makes the characterization of solid-liquid systems particularly challenging due to the lack of understanding of the building/draining mechanisms themselves.

The experimental portion of the work presented numerous challenges. The process by which a droplet is dispensed is crucial, as the location of the drop on the sphere can have an effect in the contact angle, which will in turn affect the force measurement and the rupture distance. The same is true of the volume of liquid dispensed. In this work it was necessary to use image analysis to calculate the effective volume being captured in a liquid bridge, as some of the dispensed liquid was lost to the spreading of the fluid over the bottom bead(s).

Complete characterization of the funicular regime requires measurement of liquid bridge forces for different liquid volumes corresponding to 13-25% moisture content, and for different three particle configurations.

6.4 OUTLOOK

Understanding the underlying driving force for separation can lead to efficient units for the processing of granular materials. This work presents the complete design process of separation methods by first simulating conditions computationally. The model further proved being robust enough to be able to capture the effect of a fluid in the system with enough sensibility to predict operational conditions. Monomodal, size and density disperse mixtures were successfully separated into the constitutive pure species, demonstrating the applicability of energy-efficient, rate-based separation methods to a variety of mixtures.

Further work should be done in order to transform the prototypal units described into effective industrial separation units after the rate-based separation methods presented herein. One of the major implications in achieving this lays in determining the best way to implement continuous operations.

APPENDIX A

TESTING THE ROBUSTNESS OF PD CODE - COEFFICIENT OF RESTITUTION CALCULATION

The coefficient of restitution (refer to Eq. 2.10) is an important metric for characterization of granular materials. For collision-driven flow (inside a fluidized bed, for example) the coefficient of restitution plays a determinant role in the output configuration of the mixture. In the process of simulating granular systems two main approaches are possible. The ‘hard body’ scheme assumes instantaneous collisions defined by a constant normal COR, a tangential COR and a frictional dissipation component. The second approach - termed the soft body method incorporates all mechanical properties associated with the granular material and a force balance determines the dissipated energy following every collisional event [47, 48]. This work implements the soft body methodology.

A single particle study on the energy dissipated upon collision with a flat surface was performed. The objective of this exercise is twofold; (1) assess the robustness of the PD algorithm with respect to impact velocity for different materials, and (2) extract representative values for the COR at various velocities to be used in predictive models such as the probability model described in 3.

In order to obtain the COR associated with each material a single particle is placed one particle diameter away from a flat surface and assigned a downward velocity. This process is repeated ten times for each velocity, for dimensionless velocities (v^*) in the range (0, 10). Velocities are made dimensionless following:

$$v^* = v \frac{t}{l}, \tag{A.1a}$$

$$t = \sqrt{\frac{l}{g}}, \tag{A.1b}$$

where l is the characteristic length, taken here to be particle diameter, and \vec{g} is the gravitational acceleration.

The normal velocity after impact is collected and the COR is calculated according to Eq. 2.10. The results are presented in Fig. A1, where the trend reflects the value for the coefficient of restitution decreases with increased impact velocity, an observation that is in agreement with reports in literature [126, 48]. In particular, the asymptotic value around 0.6 is in good agreement with experimental values reported for dry collisions of stainless steel [127]. The “soft” material is a fictitious material characterized by its elastic properties, where deformation is elastic and there is viscous dissipation of energy upon collisions.

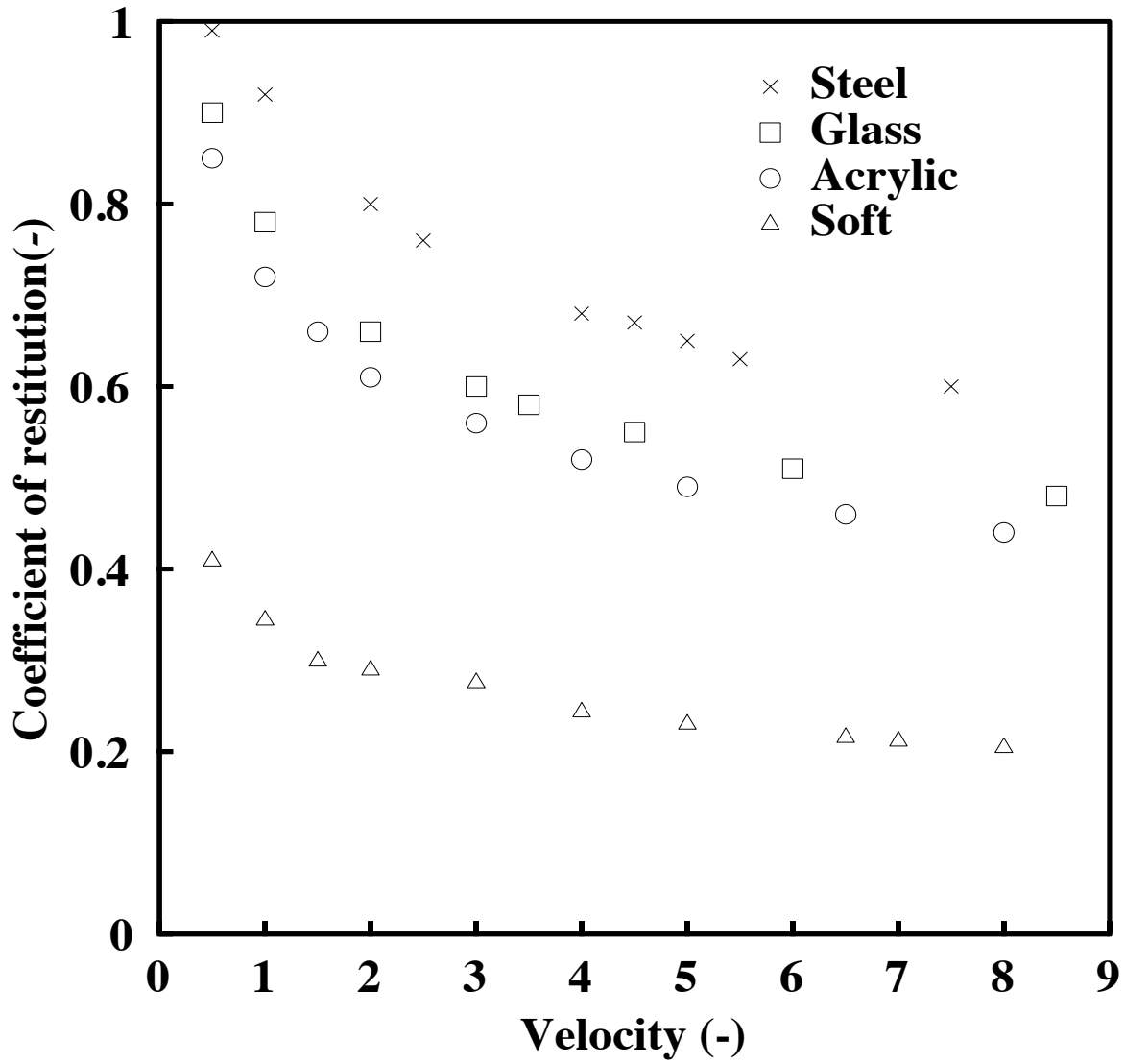


Figure A1: Coefficient of restitution values obtained implementing PD simulation, as a function of impact velocity. The velocity is made dimensionless with $d_{ref}/\sqrt{\frac{d_{ref}}{g}}$, where $d_{ref} = 9\text{mm}$.

APPENDIX B

PROBABILITY BASED TERMINAL VELOCITY CODE TO PREDICT SEPARATION IN A GALTON BOARD SYSTEM

The algorithm presented here corresponds to the probability model implemented to predict particle separation, presented in Ch. 3. The objective of this simple model is to calculate the expected terminal velocity of a particle traversing a galton board.

This input parameters for the model are the particle diameter (d_p), material coefficient of restitution (denoted in the code as e) the spacing between pegs, and the length of the board ($\max L$). This code was used to produce trend lines presented in 3.12.

```

#!/usr/bin/python

import numpy as np
import sys

maxL = int(sys.argv[1])
dp = float(sys.argv[2])

dp = float(dp/1000.0);
e = 0.25;
t = 0.0;
n = 0.0;
theta = 15.015.0*np.pi / 180. ; # inclination of the GB
peg_d = 3.18/1000.0; #meters
g = 9.816;
lp = 19.0/1000.0; #meters
h = lp*np.sin(np.pi/3) ;
a = g*np.sin(theta); #acceleration for a ball sliding down an incline
l_star = lp - peg_d;

for i in range(maxL):
r = np.random.rand()
x = r*l_star;
n += 1.0;
if (x+(dp/2.0)) <= l_star or (x -(dp/2)) >= 0.0:
deltaX = n*h+dxo;
deltat = np.sqrt(2*deltaX/a);
t += deltat;
v = e*a*deltat;

```

```
t += v/a;
dxo = 0.5*v*v/a;
n = 0.0;

deltaX = n*h + dxo;
t += np.sqrt(2*deltaX/a);
vf = float(maxL)*h/t;
print vf;
```

BIBLIOGRAPHY

- [1] Isabel Figueroa. *Exploring analogies between granular materials and fluids*. PhD thesis, University of Pittsburgh, 2013.
- [2] Tathagata Bhattacharya. *Controlling mixing and segregation in time periodic granular flows*. PhD thesis, University of Pittsburgh, 2011.
- [3] Stefanie Strauch and Stephan Herminghaus. Wet granular matter: a truly complex fluid. *Soft Matter*, 8(32):8271, 2012.
- [4] F. Bertrand, L. a. Leclaire, and G. Levecque. DEM-based models for the mixing of granular materials. *Chemical Engineering Science*, 60:2517–2531, 2005.
- [5] James B. Knight, H. M. Jaeger, and Sidney R. Nagel. Vibration-induced size separation in granular media: The convection connection. *Physical Review Letters*, 70(24):3728–3731, 1993.
- [6] Namiko Mitarai and Franco Nori. Wet Granular Materials. *Advances in Physics*, 55(March 2015):1–45, 2006.
- [7] Hm Jaeger, Sr Nagel, and Rp Behringer. Granular solids, liquids, and gases. *Reviews of Modern Physics*, 68(4):1259–1273, 1996.
- [8] J.C. Williams. The segregation of particulate materials. A review. *Powder Technology*, 15:245–251, 1976.
- [9] J.a. Drahun and J. Bridgwater. The mechanisms of free surface segregation. *Powder Technology*, 36(1983):39–53, 1983.
- [10] M. Alonso, M. Satoh, and K. Miyanami. Optimum combination of size ratio, density ratio and concentration to minimize free surface segregation. *Powder Technology*, 68:145–152, 1991.
- [11] J M Ottino and D V Khakhar. MIXing and segregation of granular materials. *Annu. Rev. Fluid Mech.*, 32:55–91, 2000.
- [12] H M Li and J J McCarthy. Controlling cohesive particle mixing and segregation. *Physical Review Letters*, 90:4, 2003.

- [13] J. E. Galvin, S. R. Dahl, and C. M. Hrenya. On the role of non-equipartition in the dynamics of rapidly flowing granular mixtures. *Journal of Fluid Mechanics*, 528:207–232, apr 2005.
- [14] Steven W. Meier, Richard M. Lueptow, and Julio M. Ottino. A dynamical systems approach to mixing and segregation of granular materials in tumblers. *Advances in Physics*, 56(February 2015):757–827, 2007.
- [15] J. Li, a. B. Yu, J. Bridgwater, and S. L. Rough. Spontaneous inter-particle percolation: A kinematic simulation study. *Powder Technology*, 203:397–403, 2010.
- [16] M. J. Woodhouse, a. R. Thornton, C. G. Johnson, B. P. Kokelaar, and J. M. N. T. Gray. Segregation-induced fingering instabilities in granular free-surface flows. *Journal of Fluid Mechanics*, 709:543–580, 2012.
- [17] Karen E Daniels and Matthias Schröter. Focus on granular segregation. *New Journal of Physics*, 15(3):035017, mar 2013.
- [18] J.C. Williams and G. Shields. The segregation of granules in a vibrated bed. *Powder Technology*, 1:134–142, 1967.
- [19] Khan Ahmad and I.J. Smalley. Observation of particle segregation in vibrated granular systems, 1973.
- [20] Troy Shinbrot and Fernando Muzzio. Reverse Buoyancy in Shaken Granular Beds. *Physical Review Letters*, 81:4365–4368, 1998.
- [21] C.H. Tai, S.S. Hsiau, and C.a. Kruelle. Density segregation in a vertically vibrated granular bed. *Powder Technology*, 204(2-3):255–262, dec 2010.
- [22] J. Bridgewater. Fundamental powder mixing mechanisms., 1975.
- [23] Suman K. Hajra and D. V. Khakhar. Radial segregation of ternary granular mixtures in rotating cylinders. *Granular Matter*, 13:475–486, 1997.
- [24] Khakhar D V., McCarthy J J., and J M Ottino. Radial segregation of granular materials in rotating cylinders. *Phys. Fluids*, 9:3600–3614, 1997.
- [25] Suman K. Hajra, Tathagata Bhattacharya, and J. J. McCarthy. Improvement of granular mixing of dissimilar materials in rotating cylinders. *Powder Technology*, 198(2):175–182, 2010.
- [26] Anurag Tripathi and D. V. Khakhar. Density difference-driven segregation in a dense granular flow. *Journal of Fluid Mechanics*, 717:643–669, 2013.
- [27] S. R. Dahl and C. M. Hrenya. Size segregation in rapid, granular flows with continuous size distributions. *Physics of Fluids*, 16(1):1, 2004.

- [28] Isaac Goldhirsch. Introduction to granular temperature. *Powder Technology*, 182(2):130–136, 2008.
- [29] J T Jenkins and S B Savage. A theory for the rapid flow of identical, smooth, nearly elastic, spherical particles. *Journal of Fluid Mechanics*, 130:187–202, 1983.
- [30] Walton O R. and R L Braun. Viscosity, Granular-Temperature, and Stress Calculations for Shearing Assemblies of Inelastic, Frictional Disks. *J. Rheol.*, 30:949–980, 1986.
- [31] Otis R. Walton. Viscosity, granular-temperature, and stress calculations for shearing assemblies of inelastic, frictional disks. *Journal of Rheology*, 30:949, 1986.
- [32] Kerry Johanson, Chris Eckert, Dev Ghose, Millorad Djomlija, and Mario Hubert. Quantitative measurement of particle segregation mechanisms. *Powder Technology*, 159(1):1–12, nov 2005.
- [33] J. M. N. T. Gray and C. Ancey. Multi-component particle-size segregation in shallow granular avalanches. *Journal of Fluid Mechanics*, 678:535–588, 2011.
- [34] J. J. McCarthy. Turning the corner in segregation. *Powder Technology*, 192(2):137–142, 2009.
- [35] Chris H. Rycroft, Ken Kamrin, and Martin Z. Bazant. Assessing continuum postulates in simulations of granular flow. *Journal of the Mechanics and Physics of Solids*, 57(5):828–839, 2009.
- [36] J.M Ottino and D.V Khakhar. Fundamental research in heaping, mixing, and segregation of granular materials: challenges and perspectives. *Powder Technology*, 121(2-3):117–122, 2001.
- [37] Shuiqing Li, Jeffrey S. Marshall, Guanqing Liu, and Qiang Yao. Adhesive particulate flow: The discrete-element method and its application in energy and environmental engineering. *Progress in Energy and Combustion Science*, 37(6):633–668, 2011.
- [38] D V Khakhar, J J McCarthy, J M Ottino, and T Shinbrot. Transverse Flow and Mixing of Granular Materials in a Rotating Cylinder. *Phys. Fluids*, 9(1997):3600–3614, 1997.
- [39] Tathagata Bhattacharya, Suman K. Hajra, and J. J. McCarthy. A design heuristic for optimizing segregation avoidance practices in horizontal drum mixers. *Powder Technology*, 253:107–115, 2014.
- [40] Tathagata Bhattacharya and J. J. McCarthy. Chute flow as a means of segregation characterization. *Powder Technology*, 256:126–139, 2014.
- [41] Isabel Figueroa, Hongming Li, and Joseph McCarthy. Predicting the impact of adhesive forces on particle mixing and segregation. *Powder Technology*, 195(3):203–212, 2009.

- [42] I. Figueroa and J. J. McCarthy. Using janus particles to control mixing and segregation of adhesive particle systems. *Industrial and Engineering Chemistry Research*, 49:5204–5214, 2010.
- [43] O R Walton. Application of molecular dynamics to macroscopic particles. *International Journal of Engineering Science*, 22(8-10):1097–1107, 1984.
- [44] Hertz H. Ueber die Berührungsfester Elastischer Körper. *J. reine ange. Math.*, 92:1–15, 1881.
- [45] O R Walton and R L Braun. Stress calculations for assemblies of inelastic spheres in uniform shear. *Acta Mechanica*, 63(1-4):73–86, 1986.
- [46] P. Gondret, M. Lance, and L. Petit. Bouncing motion of spherical particles in fluids. *Physics of Fluids*, 14(2):643, 2002.
- [47] C. Bizon, M. Shattuck, J. Swift, W. McCormick, and Harry Swinney. Patterns in 3D Vertically Oscillated Granular Layers: Simulation and Experiment. *Physical Review Letters*, 80(1):57–60, 1998.
- [48] C. Mangwandi, Y.S. Cheong, M.J. Adams, M.J. Hounslow, and a.D. Salman. The coefficient of restitution of different representative types of granules. *Chemical Engineering Science*, 62(1-2):437–450, jan 2007.
- [49] Anthony D. Rosato, Denis L. Blackmore, Ninghua Zhang, and Yidan Lan. A perspective on vibration-induced size segregation of granular materials. *Chemical Engineering Science*, 57(2):265–275, 2002.
- [50] Y Taguchi, Y Taguchi Powder, and Journal De Physique. Powder turbulence: direct onset of turbulent flow. *Journal de Physique II*, 2(12):2103–2114, 1992.
- [51] Yidan Lan and Anthony D. Rosato. Convection related phenomena in granular dynamics simulations of vibrated beds. *Physics of Fluids*, 9(12):3615, 1997.
- [52] a. Kudrolli. Size separation in vibrated granular matter. *Reports on Progress in Physics*, 209(67):40, 2004.
- [53] Xiaodong Shi, Guoqing Miao, and Hua Zhang. Horizontal segregation in a vertically vibrated binary granular system. *Physical Review E - Statistical, Nonlinear, and Soft Matter Physics*, 80:1–4, 2009.
- [54] Anchal Jain, Matthew J. Metzger, and Benjamin J. Glasser. Effect of particle size distribution on segregation in vibrated systems. *Powder Technology*, 237:543–553, 2013.
- [55] Katherine Strandburg, Friedrich Prinz, and Robert H Swendsen. Why the Brazil Nuts are on top: Size segregation of particulate Matter by shaking. *Phy. Rev. Lett.*, 58(10):1038–1040, 1987.

- [56] Francis J Alexander and Joel L Lebowitz. Driven diffusive systems with a moving obstacle : a variation on the Brazil nuts problem. *J. Phys. A: Math. Gen.*, 23:375–381, 1990.
- [57] Y Nahmad-Molinari, G Canul-Chay, and J C Ruiz-Suárez. Inertia in the Brazil nut problem. *Physical review. E, Statistical, nonlinear, and soft matter physics*, 68(4 Pt 1):041301, 2003.
- [58] Y. S. Wong, C. H. Gan, C. H. Wang, X. Fan, D. J. Parker, a. Ingram, and J. P. K. Seville. Instabilities in vertically vibrated granular beds at the single particle scale. *Physics of Fluids*, 18(4):043302, 2006.
- [59] James B. Knight, Christopher G. Fandrich, Chun Ning Lau, Heinrich M. Jaeger, and Sidney R. Nagel. Density relaxation in a vibrated granular material. *Physical Review E*, 51(5):3957–3963, 1995.
- [60] S.S. Hsiau, M.H. Wu, and C.H. Chen. Arching phenomena in a vibrated granular bed. *Powder Technology*, 99(February):185–193, 1998.
- [61] S.C. Yang. Segregation of cohesive powders in a vibrated granular bed. *Chemical Engineering Science*, 61(18):6180–6188, sep 2006.
- [62] Kaiwei Hu, Zi-Ang Xie, Ping Wu, Jing Sun, Li Li, Chao Jia, Shiping Zhang, Chuanping Liu, and Li Wang. Convecting particle diffusion in a binary particle system under vertical vibration. *Soft Matter*, 10:4348–4359, 2014.
- [63] Guy Barnocky and Rh Robert H Davis. Elastohydrodynamic collision and rebound of spheres: experimental verification. *Physics of Fluids*, 31(1988):1324–1329, 1988.
- [64] Scott Bair and Peter Kottke. Pressure-Viscosity Relationships for Elastohydrodynamics. *Tribology Transactions*, 46(3):289–295, jan 2003.
- [65] M. E Urso, C. J Lawrence, and M.J. Adams. Pendular, Funicular, and Capillary Bridges: Results for Two Dimensions. *Journal of colloid and interface science*, 220(1):42–56, dec 1999.
- [66] MED Urso, CJ Lawrence, and MJ Adams. A two-dimensional study of the rupture of funicular liquid bridges. *Chemical engineering science*, i:677–692, 2002.
- [67] C. M. Donahue, C. M. Hrenya, R. H. Davis, K. J. Nakagawa, a. P. Zelinskaya, and G. G. Joseph. Stokes’ cradle: normal three-body collisions between wetted particles. *Journal of Fluid Mechanics*, 650:479, mar 2010.
- [68] CL Flemmer. On the regime boundaries of moisture in granular materials. *Powder Technol.*, 66:191–194, 1991.

- [69] B.J. Ennis, J Li, G.I Tardos, and R. Pfeffer. The influence of viscosity on the strength of an axially strained pendular liquid bridge. *Chemical Engineering Science*, 45(10):3071–2088, 1990.
- [70] S.J.R. Simons, J P K Seville, and M.J. Adams. An Analysis of the rupture energy of pendular liquid bridges. *Chemical Engineering Science*, 49(14):2331–2339, 1994.
- [71] M J Adams and V Perchard. The cohesive forces between particles with interstitial liquid. In *Institute of Chemical Engineering Symposium*, volume 91, pages 147–160, 1985.
- [72] A.J. Goldman, R.G. Cox, and H. Brenner. Slow viscous motion of a sphere parallel to a plane wall - II Couette flow. *Chemical Engineering Science*, 22(4):653–660, 1967.
- [73] J Crassous, E Charlaix, H Gayvallet, and JL Loubet. Experimental study of a nanometric liquid bridge with a surface force apparatus. *Langmuir*, 9(2):1995–1998, 1993.
- [74] Gouping Lian, Colin Thornton, and Michael J. Adams. A Theoretical Study of the Liquid Bridge Forces between Two Rigid Spherical Bodies. *Journal of Colloid and Interface Science*, 161:138–147, 1993.
- [75] SJR Simons, JPK Seville, and M.J. Adams. An analysis of the rupture energy of pendular liquid bridges. *Chemical Engineering Science*, 49(14):2331–2339, 1994.
- [76] Boris Y Rubinstein and Leonid G Fel. Theory of axisymmetric pendular rings. *Journal of colloid and interface science*, 417:37–50, mar 2014.
- [77] Mikami T., Kamiya H., and M Horio. Numerical simulation of cohesive powder behavior in a fluidized bed. *Chem. Eng. Sci.*, 53(10):1927–1940, 1998.
- [78] Sumedh R. Risbud and German Drazer. Trajectory and distribution of suspended non-Brownian particles moving past a fixed spherical or cylindrical obstacle. *Journal of Fluid Mechanics*, 714:213–237, 2013.
- [79] Cp Dettmann. Diffusion in the Lorentz gas. *Commun. Theor. Phys*, 62:521–540, 2014.
- [80] Kenichi Arai, Takahisa Harayama, Satoshi Sunada, and Peter Davis. Randomness in a Galton board from the viewpoint of predictability: Sensitivity and statistical bias of output states. *Physical Review E - Statistical, Nonlinear, and Soft Matter Physics*, 86:2–4, 2012.
- [81] M. Nuñez, a. López Villa, C. a. Vargas, and a. Medina. Stochastic Trajectories of Beads in the Galton-Board. *Applied Mechanics and Materials*, 110-116:299–309, 2011.
- [82] J G Benito, a M Vidales, and I Ippolito. Segregation in a Galton Board. *Journal of Physics: Conference Series*, 166:012003, 2009.

- [83] V. V. Kozlov and M. Yu. Mitrofanova. Galton Board. *Regular and chaotic dynamics*, 8(4):431–439, 2005.
- [84] L Bruno, a Calvo, and I Ippolito. Dispersive flow of disks through a two-dimensional Galton board. *The European physical journal. E, Soft matter*, 11(2):131–40, jun 2003.
- [85] I Ippolito, L Samson, S Bourles, J P Hulin, S Bourlès, and JP. Diffusion of a single particle in a 3D random packing of spheres. *The European Physical*, 236:227–236, 2000.
- [86] Arthur Lue and Howard Brenner. Phase flow and statistical structure of Galton-board systems. *Phys. Rev. E*, 47(5):3128–3144, 1993.
- [87] Deniz Ertas. Lateral Separation of Macromolecules and Polyelectrolytes in Microlithographic Arrays. *Phy. Rev. Lett.*, 80(7):4, 1997.
- [88] a van Oudenaarden and S G Boxer. Brownian ratchets: molecular separations in lipid bilayers supported on patterned arrays. *Science (New York, N.Y.)*, 285(5430):1046–1048, 1999.
- [89] C. Keller, Florian Marquardt, and C. Bruder. Separation quality of a geometric ratchet. *Physical Review E - Statistical, Nonlinear, and Soft Matter Physics*, 65(4):1–15, 2002.
- [90] J Machta and I Oppenheim. Mode-Coupling Theory of Hydrodynamics and Steady-State Systems. *Physica A-Statistical Mechanics And Its Applications*, 112:361–392, 1982.
- [91] Vincent Dumas, De Voluceau, and Le Chesnay Cedex. A multiclass network with non-linear, non-convex, non-monotonic stability conditions. *Queueing Systems*, 25:1–43, 1997.
- [92] N. Chernov and D. Dolgopyat. Diffusive Motion and Recurrence on an Idealized Galton Board. *Physical Review Letters*, 99(3):030601, jul 2007.
- [93] Andrew M. Scott and John Bridgwater. Interparticle Percolation: A Fundamental Solids Mixing Mechanism. *Industrial and Engineering Chemistry Fundamentals*, 14(1):22–27, 1975.
- [94] N. Roussel, Thi Lien Huong Nguyen, and P. Coussot. General probabilistic approach to the filtration process. *Physical Review Letters*, 98(11):1–4, 2007.
- [95] J. J. McCarthy and J. M. Ottino. Particle dynamics simulation: A hybrid technique applied to granular mixing. *Powder Technology*, 97:91–99, 1998.
- [96] Luciana Bruno, Irene Ippolito, and Adriana Calvo. Granular mixing in a Galton board. *Granular Matter*, 3(1-2):83–86, 2001.
- [97] F. J. Jr Massey. The Kolmogorov-Smirnov test of goodness of fit. *Journal of the American Statistical Association*, 46:68–78, 1951.

- [98] R Wilcox. KolmogorovSmirnov Test. *Encyclopedia of Biostatistics*, pages 83–90, 1998.
- [99] Rumpf H. *Particle Technology*. Chapman and Hall Publishers, New York, 1975.
- [100] Hitoshi Gotoh and Tetsuo Sakai. Numerical Simulation of Sheetflow as Granular Material. *Journal of Waterway, Port, Coastal, and Ocean Engineering*, 123(December):329–336, 1997.
- [101] F Chevoir, F Gaulard, and N Roussel. Flow and jamming of granular mixtures through obstacles. *Europhysics Letters (EPL)*, 79:14001, 2007.
- [102] Kerry Johanson, Chris Eckert, Dev Ghose, Millorad Djomlija, and Mario Hubert. Quantitative measurement of particle segregation mechanisms. *Powder Technology*, 159(1):1–12, nov 2005.
- [103] Dimitrios Geromichalos, Mika M Kohonen, Frieder Mugele, and Stephan Herminghaus. Mixing and condensation in a wet granular medium. *Physical review letters*, 90(April):168702, 2003.
- [104] Shu-san Hsiau and Shie-chen Yang. Numerical simulation of self-diffusion and mixing in a vibrated granular bed with the cohesive effect of liquid bridges. *Chem. Eng. Sci.*, 58:339–351, 2003.
- [105] Hongming Li and J. McCarthy. Phase diagrams for cohesive particle mixing and segregation. *Physical Review E*, 71(April 2004):1–8, 2005.
- [106] Hans-Jürgen Butt and Michael Kappl. Normal capillary forces. *Advances in colloid and interface science*, 146(1-2):48–60, feb 2009.
- [107] P C T de Boer and M P de Boer. Rupture work of pendular bridges. *Langmuir : the ACS journal of surfaces and colloids*, 24(1):160–9, jan 2008.
- [108] Patrice Pierrat and Hugo S Caram. Tensile strength of wet granular materials. *Powder Technology*, 91:83–93, 1997.
- [109] C.L. Feng and a.D. Yu. Effect of liquid addition on the packing of mono-sized coarse spheres. *Powder Technology*, 99(1):22–28, sep 1998.
- [110] Yakov I Rabinovich, Madhavan S Esayanur, and Brij M Moudgil. Capillary forces between two spheres with a fixed volume liquid bridge: theory and experiment. *Langmuir : the ACS journal of surfaces and colloids*, 21(24):10992–7, nov 2005.
- [111] Kazuyuki Hotta, Kazuo Takeda, and Koichi Inoya. The Capillary Binding Force of a Liquid Bridge Capillary. *Powder Technology*, 10:231–242, 1974.
- [112] D MegiasAlguacil and LJ Gauckler. Capillary forces between two solid spheres linked by a concave liquid bridge: regions of existence and forces mapping. *AIChE journal*, 55(5), 2009.

- [113] David Megias-Alguacil and Ludwig J. Gauckler. Analysis of the capillary forces between two small solid spheres binded by a convex liquid bridge. *Powder Technology*, 198(2):211–218, mar 2010.
- [114] Kazuo Murase, Tsuyoshi Mochida, and Hiroyuki Sugama. Experimental and numerical studies on liquid bridge formed among three spheres. *Granular Matter*, 6(2-3):111–119, oct 2004.
- [115] WC Clark, JM Haynes, and G Mason. Liquid bridges between a sphere and a plane. *Chemical Engineering Science*, 23(Table 1):810–812, 1968.
- [116] H Schubert. CAPILLARY FORCES - MODELING AND APPLICATION IN PARTICULATE TECHNOLOGY. *Powder Technology*, 37:105–116, 1984.
- [117] Christopher D Willett, Michael J Adams, Simon A Johnson, and Jonathan P K Seville. Capillary Bridges between Two Spherical Bodies. *Langmuir*, 16(24):9396–9405, 2000.
- [118] J.-P. Gras, J.-Y. Delenne, and M. S. El Youssoufi. Study of capillary interaction between two grains: a new experimental device with suction control. *Granular Matter*, 15(1):49–56, dec 2012.
- [119] F. M. Orr, L. E. Scriven, and a. P. Rivas. Pendular rings between solids: meniscus properties and capillary force. *Journal of Fluid Mechanics*, 67(04):723, mar 1975.
- [120] O Pitois, P Moucheront, and X Chateau. Liquid Bridge between Two Moving Spheres: An Experimental Study of Viscosity Effects. *Journal of colloid and interface science*, 231(1):26–31, nov 2000.
- [121] O Pitois, P Moucheront, and X Chateau. Rupture energy of a pendular liquid bridge. *PHYSICAL JOURNAL B*, 86:79–86, 2001.
- [122] S. Farshid Chini and a. Amirfazli. A method for measuring contact angle of asymmetric and symmetric drops. *Colloids and Surfaces A: Physicochemical and Engineering Aspects*, 388(1-3):29–37, sep 2011.
- [123] Majid Soleimani, Reghan J Hill, and Theo G M van de Ven. Bubbles and drops on curved surfaces. *Langmuir : the ACS journal of surfaces and colloids*, 29(46):14168–77, nov 2013.
- [124] H. B. Eral, D. J. C. M. t Mannelje, and J. M. Oh. Contact angle hysteresis: a review of fundamentals and applications. *Colloid and Polymer Science*, 291(2):247–260, sep 2012.
- [125] Michael J Adams, Simon A Johnson, Jonathan P K Seville, and Christopher D Willett. Mapping the Influence of Gravity on Pendular Liquid Bridges between Rigid Spheres. *Langmuir*, 18(16):6180–6184, 2002.

- [126] R Ramírez, T Pöschel, NV Brilliantov, and Thomas Schwager. Coefficient of restitution of colliding viscoelastic spheres. *Physical review E*, 60(4):24–26, 1999.
- [127] Advait a. Kantak and Robert H. Davis. Collisions of spheres with wet and dry porous layers on a solid wall. *Chemical Engineering Science*, 61:417–427, 2006.